Strange Metal Behavior in Electron Doped Cuprates Superconductor

A thesis
Submitted towards the partial fullfilment of
BS-MS dual degree programme
by

Arindam Ghara

Date: 10th May, 2024

under the guidance of

Dr. Surjeet Singh

Indian Institute of Science Education and Research Pune

from May 2023 to April 2024

Indian Institute of Science Education and Research Pune

Certificate

This is to certify that this dissertation entitled " Strange Metal Behaviour in Electron Doped Cuprates Superconductor " submitted towards the partial fulfillment of the BS-MS degree at the Indian Institute of Science Education and Research Pune, represents original research carried out by Arindam Ghara at the Indian Institute of Science Education and Research Pune, under the supervision of Dr. Surjeet Singh during academic year May 2023 to March 2024.

Dr. Surjeet Singh
Department of Physics
IISER Pune

Date: 10/05/2024

Declaration

I hereby declare that the matter embodied in the report entitled " Strange Metal Behaviour in Electron Doped Curpates Superconductor " are the results of the work carried out by me at the Department of Physics, Indian Institute of Science Education and Research (IISER) Pune, under the supervision of Dr. Surjeet Singh, and the same has not been submitted elsewhere for any other degree. Wherever others contribute, every effort is made to indicate this clearly, with due reference to the literature and acknowledgment of collaborative research and discussions.

Arindam Gahra

Arindam Gahra
(Roll No - 20191074)
BS-MS fifth year
IISER Pune

Date: 10/05/2024

Acknowledgments

I would like to express my deepest gratitude to Dr. Surjeet Singh for his unwavering guidance and support throughout my journey to completing my Master's thesis. His expertise and insightful feedback have been instrumental in shaping my academic and research endeavors, providing a strong foundation for my work in the complex field of highly correlated systems.

I extend my gratitude to Professor Emeritus Srinivasan Ramakrishnan, my thesis advisor, for his invaluable contributions to my research. His expertise and thoughtful discussions have been instrumental in enhancing the caliber of my work.

I am immensely grateful to my lab members, Sagar Bhaiya, Dibyata Di, and Navita Di, for their mentorship and for teaching me essential experimental techniques crucial for navigating the nuances of a condensed matter lab. Special acknowledgment to Luminita Mam, whose advice on lab safety and precautions has not only ensured a secure working environment but also fostered a considerate and supportive lab culture. I deeply appreciate the insightful discussions with Ankit Bhaiya and Sagar Bhaiya, which have broadened my understanding and perspective on our research topics. Dinesh Bhaiya's guidance in familiarizing me with various instrumentations and the operation of the hall setup has been invaluable. I extend my gratitude to Pankaj Bhaiya, Nashra Di, Prabhu Bhaiya, Lalit Bhaiya, Vishak, Dibya, and Rupesh for making the lab a lively and entertaining place. A huge shoutout to all my lab mates for turning every day into a feast! Your endless parade of snacks and sweets has been the sprinkle of joy on my research doughnut. Thanks for making the lab a tastier place to be!

My acknowledgment extends to Nilesh Sir, Sudhir Sir, Anil Sir, and Karthikeyan for their indispensable technical support, without which navigating the challenges of lab work would have been considerably more difficult.

I am grateful to Vikram Bhaiya for his indispensable assistance with the low-temperature resistivity measurements of my samples. His guidance was crucial in conducting low-temperature measurements accurately, greatly enhancing the conclusion of my research.

My gratitude extends deeply to Mehul, Raghav, and Vedant, whose friendship and guidance have been constants in every aspect of my life. Their unwavering support and belief in my potential have been foundational to my growth. Furthermore, Samarth, Varun, Shubhankar, Hrishikesh, Sanket, and Rajeet have significantly contributed to enriching my life outside the realm of academics, providing memorable and joyous moments that I cherish. Their roles in my life underscore the importance of camaraderie and shared experiences in shaping one's journey through both challenging and rewarding times. This circle of friends has not only been instrumental in my personal and professional development but has also offered a sense of belonging and encouragement, highlighting the profound impact of friendship on personal growth and well-being. Their collective presence has indeed made my journey more meaningful and enjoyable.

My heartfelt thanks extend to my group friends Deep, Siddhant, Eksha, Vedanth, Rohan, Eishica, and Ojashvi for sharing their notes, which were crucial in allowing me to manage my class attendance effectively. Furthermore, the advice and insights from numerous seniors, specifically Raikhik, have been invaluable to my academic progress and have played a key role in my journey.

In closing, I wish to express my deepest appreciation to my parents for their steadfast guidance and unwavering support, which have served as the foundation of my endeavors. Their sage advice and unconditional backing have been the driving force behind my pursuits. Similarly, my cousins and brothers deserve acknowledgment for their constant companionship and support, bolstering my determination at every stage of my journey.

This thesis would not have been possible without the collective support, encouragement, and guidance from each of these individuals.

Abbreviations

Abbreviations	Explanations
EDC	Electron Doped Cuprates
HDC	Hole Doped Cuprates
SC	Superconductivity
QCP	Quantum Critical Point
FSR	Fermi Surface Reconstructions
FL	Fermi Liquid
XRD	X-Ray Diffraction
SEM	Scanning Electron Microscopy
EDX	Energy Dispersive X-Ray Spectroscopy
TGA	Thermogravimetric Analysis
LFA	Laser Flash Analysis
DSC	Differential Scanning Calorimetry
LCCO	$La_{2-x}Ce_xCuO_4$
NCCO	$Nd_{2-x}Ce_xCuO_4$
PCCO	$Pr_{2-x}Ce_xCuO_4$
NSCCO	$Nd_{1.82-y}Sr_yCe_{0.18}CuO_4$
LSCO	$La_{2-x}Sr_xCuO_4$
Nd-LSCO	$La_{1.6-x}Nd_{0.4}Ce_xCuO_4$
Bi2212	$Bi_2Sr_2CaCu_2O_{8+\delta}$
Bi2201	$Bi_2Sr_2Cu_1O_{6+\delta}$
D_Q	Thermal Diffusivity
D_Q^{-1}	Thermal Resistivity

Contents

List of Figures

List of Tables

Abstract

Unraveling the origin of unconventional superconductivity in cuprates has remained a long-standing enigma in the field of highly correlated systems since the discovery of high-temperature superconductors in 1986. The normal state properties of cuprates, from which superconductivity emerges, exhibit numerous anomalous features that defy conventional condensed matter theory. One such anomaly is the strange metal behavior of cuprates, characterized by a T-linear resistivity trend over all temperature ranges in hole-doped cuprates (HDCs) and a T-linear behavior at low temperatures transitioning to T-quadratic at high temperatures for electron-doped cuprates (EDCs), which lacks a comprehensive theoretical understanding. While the T-linear behavior has been empirically linked to superconductivity, a coherent theory remains elusive. Similarly, the origin of the T^2 behavior observed at high temperatures for EDCs is not well understood. The mechanisms driving the crossover from linear to quadratic temperature dependence in the resistivity of EDCs at elevated temperatures remain unclear. Furthermore, the distinct high-temperature resistivity behaviors of HDC, ($\rho \sim T$) and EDC, ($\rho \sim T^2$), despite their similar low-temperature characteristics ($\rho \sim T$), present a compelling puzzle.

The focus of this thesis is centered specifically on the T^2 behavior. Previous studies on EDCs have reported that this T^2 behavior is not universally observed in all samples, with its observation being limited to some single crystal and some thin film studies. In our work, we have studied polycrystalline NCCO samples over a wide range of doping concentrations. Our detailed resistivity analysis suggests that the T^2 behavior is an inherent feature present in all types of EDC samples; however, its clear observation in experimental data is masked by the grain boundary scattering in the polycrystalline sample. Our resistivity analysis is

supported by Seebeck studies and sample conditioning performed using hot-pressing techniques.

In the second chapter, we propose a simplistic model to understand the strange metal phase, consistent with previous experimental observations. This model highlights the importance of competing contributions leading to unique resistivity trends in different samples and temperature ranges. This model facilitates a qualitative understanding of the transition from linear to quadratic temperature dependence in the resistivity of EDCs at high temperatures.

Finally, we studied the thermal resistivity of our samples within the framework of the Planckian dissipation limit theorem to understand the correlation between thermal and electrical transport properties. Our studies suggest an inherent, yet not straightforward, connection between these two crucial physical parameters at high temperatures. The analysis of thermal resistivity has been carried out in parallel with electrical resistivity to elucidate the connection between electronic and phononic transport.

Chapter 1

INTRODUCTION

The discovery of High-temperature superconductivity in the Ba-doped La_2CuO_4 by Bednorz and Müller [1] in 1986 not only changed the ideas about the limit of superconducting transition temperature at ambient pressure but also revolutionized the key idea about the importance of strong electron correlations in the physical properties of materials. These materials, where the electronic correlations play a dominant role, are therefore rightly dubbed as strongly correlated electron systems, and high-Tc cuprates constitute a prime example of this class of systems. Over the years, we have observed the discovery of many exciting and new strongly correlated superconductors [2][3][4]. However, understanding the microscopic origin of superconductivity in Cuprates has remained a daunting task. We have yet to find a theory of unconventional superconductivity. Moreover, the normal state of Cuprates consists of many exotic phases that have not been fully understood, such as - the interplay between charge ordering and magnetism, Charge Density wave (CDW), Pair Density wave (PDW), Strange Metal behavior, Quantum Criticality, Fermi Surface Reconstruction (FSR), and the Pseudogap phase, etc [5][6][7][8].

The Electron-doped Cuprates (EDC) represent a frontier in unconventional superconductivity and have physical properties that are not compatible with conventional theories. One curious aspect of EDC is its “Strange Metal" [9] state, where resistivity varies with the square of the temperature at high temperatures, divergent from the linear variation seen in conventional metals. This T^2-resistivity suggests a departure from the well-understood electron-phonon interactions and into a regime where electronic correlations take the lead.

The intriguing phenomenon of the strange metal state in Cuprates is also highlighted by its departure from the Mott-Ioffe-Regel limit [10], which is a fundamental guiding principle of our understanding of metallic transport. This defiance raises profound questions about the very nature of quasiparticles and their interactions within the lattice. In the Cuprates' normal state, electrons behave in a manner that suggests they are neither completely free, as in conventional metals, nor localized, as in insulators. These materials push the boundaries of conventional physics. Unlocking the secrets of this behavior is crucial for unraveling the mystery of the superconducting state in Cuprates.

Understanding the normal state of Cuprates is an essential preamble to decoding superconductivity. This state is where the seeds of superconducting behavior are sown and where the interplay of various physical phenomena manifests most vividly. The resistivity trends observed in EDCs hint at the subtleties of electron interaction with the crystal lattice and with each other, an intricate puzzle of thermal and quantum mechanics. This resistivity behavior not only illuminates the peculiarities of the electron-doped materials but also allows for a comparative study with their hole-doped counterparts, potentially unraveling the asymmetry in their behaviors. Understanding the normal state could offer insights into the mechanism of electron pairing, a mechanism that defies the predictions of conventional BCS theory and paves the way for unconventional superconductivity.

The sample-dependent T^2 behavior of EDCs is a focal point of this thesis. Variations across different samples offer a unique window into the role of micro-structural subtleties of samples in dictating electronic properties. The lattice constants, microstructures, and stoichiometry, which vary from sample to sample, modulate the electron's mean free path, their scattering rates, and thus the material's resistivity. By examining how these factors affect the quadratic temperature dependency, we aim to connect together a broader understanding of the normal state of EDC.

1.1 Crystal Structure of High-Tc Cuprates

At the heart of the distinction between hole-doped cuprates (HDC) and electron-doped cuprates (EDC) lies their crystallographic structures, which, while sharing a common tetragonal foundation, diverges in the arrangement of the CuO_2 planes. In this thesis, we will specifically talk about R214 Cuprates, which is given by the chemical formula R_2CuO_4 (Where R is a rare-earth element, such as - La, Nd, Pr, Sm, Eu, Gd). We dope electrons in these systems by doping Cerium (Ce) in place of R, and the hole-doping is done by substitution of R by Strontium (Sr), Barium (Ba), and Calcium (Ca). Both types of Cuprates (HDC and EDC) crystallize in a tetragonal lattice; however, EDCs typically exhibit T' phases [11], and the HDCs have T phase [12]. The key difference is the absence of the apical oxygen above the CuO_2 plane in the EDC, as presented in the figure 1.1a.

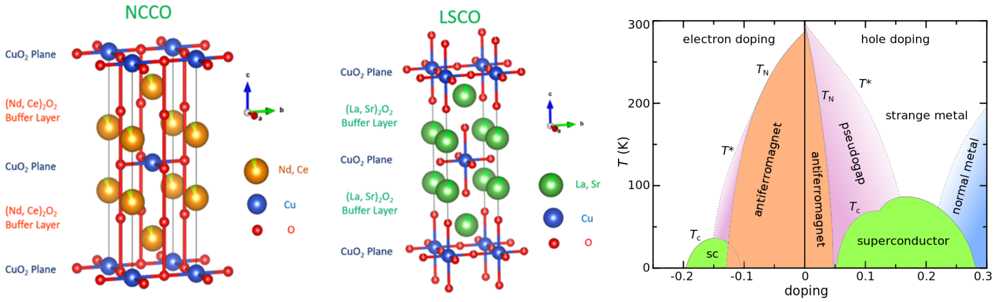

(a) (b)

Figure 1.1: (a) The crystal structure of HDC (LSCO, Sr-doped La_2CuO_4) and EDC (NCCO, Ce-doped Nd_2CuO_4) presenting the absence of apical oxygen in the EDC, NCCO. (b) The phase diagram of HDC and EDC showing different competing phases (Source - [13]).

In both these systems, the CuO_2 planes are shifted by (a/2, a/2) relative to adjacent planes, which influences the antiferromagnetic interactions that are crucial for their high-temperature superconductivity. This distinct lattice structure in EDCs, particularly the T' phase without the apical oxygen, creates an environment where the doped electrons can induce superconductivity through mechanisms that might be different from that in HDCs. The pivotal role of the lattice in determining the physical properties of these materials corresponds to the different phase diagrams of EDC and HDC, as shown in figure 1.1b, having many interesting anomalous normal state properties.

1.2 Unconventional Superconductivity

Unconventional superconductivity in cuprates is a phenomenon that challenges the standard BCS theory of superconductivity. In these materials, superconductivity does not arise from the traditional electron-phonon interaction but potentially from the exchange of magnetic spin fluctuations or other exotic mechanisms. Cuprates have a layered perovskite structure, and their superconducting properties emerge from the complex interplay within the CuO_2 planes. The critical temperatures for superconductivity in these materials are much higher than in conventional superconductors, with some Cuprates exhibiting critical temperatures as high as 165 K.

The exact mechanism behind this unconventional superconductivity is still a subject of intense research. Cuprates display a variety of strange behaviors, such as a pseudogap phase and strange metal behavior that are not coherent with the traditional Bardeen-Cooper-Schrieffer (BCS) theory. Research suggests that the cuprates' superconductivity could be related to their unique electronic structure, which features a mix of localized and itinerant electron characteristics. Recently, the charge-transfer superexchange interactions between electrons on adjacent Cu sites have been argued as the electron-pairing mechanism in HDC superconductors by the group of J. C. Séamus Davis [14].

For a more detailed understanding of unconventional superconductivity in cuprates, including potential mechanisms and their implications, a complete understanding of the normal state is very crucial.

1.3 Anomalous Normal State

The normal state of cuprates, a precursor to their high-temperature superconductivity, exhibits a complex phase diagram characterized by several anomalous phases. These include the pseudogap phase, non-Fermi liquid behavior, charge density waves (CDW), antiferromagnetic fluctuations, quantum critical points (QCP), and Fermi surface reconstruction (FSR), among others (figure 1.1b).

The pseudogap phase is marked by a partial gap in the electronic density of states, observed below a characteristic temperature T^* but above the superconducting transition temperature T_c. This phase signifies a depletion of electronic states, suggesting a precursor to the formation of Cooper pairs or competing orders [7].

Non-Fermi liquid behavior is evident in the linear temperature dependence of resistivity, deviating from the quadratic temperature dependence expected from the Fermi liquid theory at very low temperatures. This suggests that the electrons do not behave as independent quasiparticles, indicative of strong correlations [8].

Charge density waves (CDW) and antiferromagnetic fluctuations reflect underlying order in the charge and spin configurations, respectively. CDWs manifest as periodic modulations in the charge density, while antiferromagnetic fluctuations are tied to the magnetic ordering of the Cu spins in the CuO_2 planes, highlighting the complex interplay between charge, spin, and lattice degrees of freedom [8].

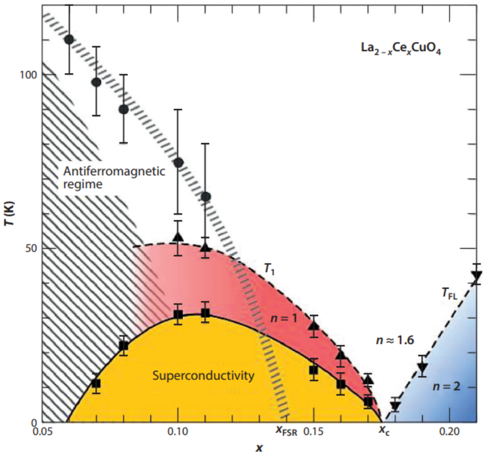

Figure 1.2: The temperature-doping (T-x) phase diagram of $La_{2-x}Ce_xCuO_4$ (Example of EDC) illustrates various phases, including the superconducting dome (yellow) and the long-range antiferromagnetic (AF) phase (hatched), with AF fluctuations indicated by circles. Colored regions denote the temperature dependence of resistivity, where $\rho \sim T^n$, with n = 1 (red) and n = 2 (blue). Between these regions lies the strange metallic phase, characterized by a different power law extending to high temperatures (Source - [9]).

The idea of a quantum critical point (QCP) plays a key role in comprehending the phase diagram of cuprates, indicating a phase transition at zero temperature influenced by quantum fluctuations. The strange metal behavior observed in cuprates is thought to be linked to their proximity to a QCP [15].

Fermi surface reconstruction (FSR) involves a change in the topology of the Fermi surface due to various ordering phenomena such as antiferromagnetism, CDW, or superconductivity itself. This reconstruction is a pivotal aspect of the cuprates' phase diagram, altering the electronic structure and, thus, the material's properties [16].

These phases underscore the rich physics of cuprates, where traditional models of superconductivity and metallicity are inadequate. Understanding the interplay between these anomalous phases is crucial for unraveling the mechanism of high-temperature superconductivity in cuprates.

1.4 Strange Metal Behavior

The phenomenon of "Strange Metal" behavior in cuprates, particularly noticeable in the context of resistivity, offers a stark deviation from conventional Fermi-liquid theory. In hole-doped Cuprates (HDC) near optimal doping, resistivity displays a linear temperature dependence (T-linear) across the entire measurable temperature range without any change in slope or discontinuities. This T-linear resistivity, contrasting sharply with the T^2 dependency predicted by Fermi-liquid theory, is not exclusive to cuprates but has also been observed in iron-based and organic superconductors, hinting at a fundamental linkage to unconventional superconductivity. Empirical relationships established in recent studies, such as the 2020 Nature publication [9], highlight a correlation between the slope of this resistivity trend and the superconducting critical temperature, suggesting a deep-seated connection between T-linear behavior and superconductivity mechanisms.

Conversely, electron-doped Cuprates (EDC) exhibit a linear temperature dependency in resistivity only at lower temperatures, with superconductivity suppressed under an external magnetic field. Beyond 50K (roughly), this behavior transitions to a quadratic temperature dependence (T^2), extending to the highest accessible temperatures. Both HDC and EDC's resistivity patterns defy expected conventions and exhibit no signs of saturation, thereby breaching the Mott-Ioffe-Regel (MIR) resistivity limit and earning the classification as "Strange Metals" or "Bad Metals."

Beyond resistivity, Strange Metal behavior in cuprates extends to several other physical

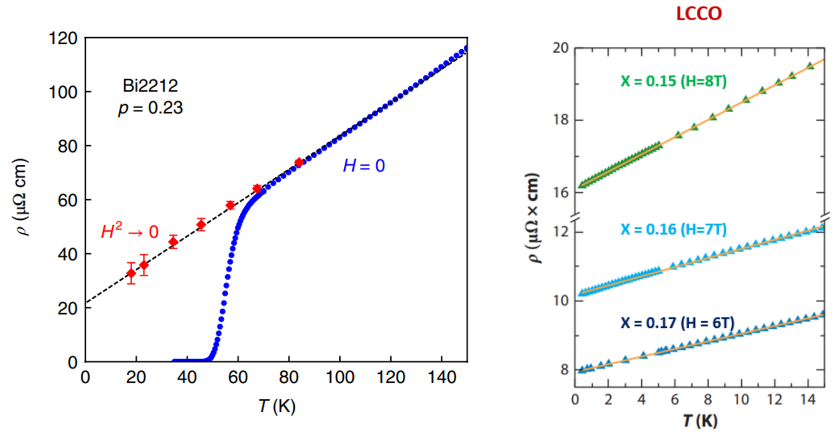

(a)

(b)

Figure 1.3: (a) T-linear resistivity behavior of HDC as seen in $Bi2212$ (Source - [17]). (b) T-linear behavior of EDC at low temperature as seen in $LCCO$ (Source - [18]).

properties, each presenting anomalous features. Thermopower, or Seebeck coefficient, in these materials, often diverges from standard metallic predictions, displaying a logarithmic temperature dependence, which is $S/T \sim -\ln T$ [19]. Magnetoresistance in Strange Metals does not follow the conventional quadratic field dependence but rather exhibits a linear field dependence [20]. Optical conductivity, deviating from the simple Drude model, often shows a frequency dependence indicative of complex charge carrier dynamics [5]. The Hall effect [21], too, manifests peculiar temperature and doping dependencies, reflecting the unconventional nature of the charge carriers in these systems. These characteristics underline the inadequacy of conventional theories to fully capture the physics of Strange Metals, pointing instead towards the influence of strong correlations, quantum criticality, and other non-Fermi liquid behaviors.

However, a distinct anomaly is observed in the high-temperature resistivity behavior of EDCs, which transitions to a T^2 dependence, setting a clear contrast with the T-linear trend of HDCs. This difference is critical for understanding the distinct mechanisms at play in EDCs, which underscores the importance of developing theories that can account for these two divergent behaviors. The quadratic temperature dependence in EDCs above 50K, persisting to the highest measurable temperatures, challenges the universality of T-linear resistivity in defining Strange Metal behavior and emphasizes the complexity of the normal state in cuprate superconductors.

1.5 T^2 temperature dependence of EDC

The quadratic temperature dependence of resistivity (T^2) at high temperatures in EDC stands as a significant anomaly in the study of high-temperature superconductors. This behavior starkly contrasts with the linear temperature dependence observed in Hole Doped Cuprates (HDC) and challenges the conventional theories of electron transport in metals. In conventional Fermi-liquid theory, a T^2 dependence of resistivity is anticipated at low temperatures due to electron-electron scattering, yet the persistence of this trend at high temperatures in EDCs, well beyond the Fermi-liquid regime, presents a conundrum [22].

This quadratic dependence in EDCs is intriguing not only because it diverges from the linear behavior of low temperature but also because it suggests a fundamental difference in the electronic interactions within EDCs as compared to HDCs. The transition from T-linear at lower temperatures to T^2 at higher temperatures within EDCs cannot be adequately explained by existing theoretical frameworks, which typically predict a saturation of resistivity at high temperatures due to phonon scattering limits, adhering to the Mott-Ioffe-Regel limit.

Understanding the T^2 temperature dependence is crucial for several reasons. Firstly, it may shed light on the nature of the interactions and scattering mechanisms at play in the normal state of EDCs, providing insights into the electronic structure and the role of correlations and fluctuations. Secondly, the distinct behavior between EDCs and HDCs raises fundamental questions about the universality and diversity of electronic behaviors in cuprates, challenging the notion of a single model for high-temperature superconductivity. Finally, the recent studies from Greene et al. [22] suggest that the coefficient of quadratic temperature dependency shows a similar trend as the critical temperature as a function of doping.

Investigating this quadratic temperature dependence is, therefore, pivotal for developing a comprehensive understanding of high-temperature superconductivity. It opens avenues for questioning and refining the theoretical models that seek to describe the electronic properties of cuprates. Such investigations could not only demystify the superconducting pairing mechanism in EDCs but also enhance our understanding of the phase diagram of cuprates, including the interplay between superconductivity, magnetism, and other electronic orders.

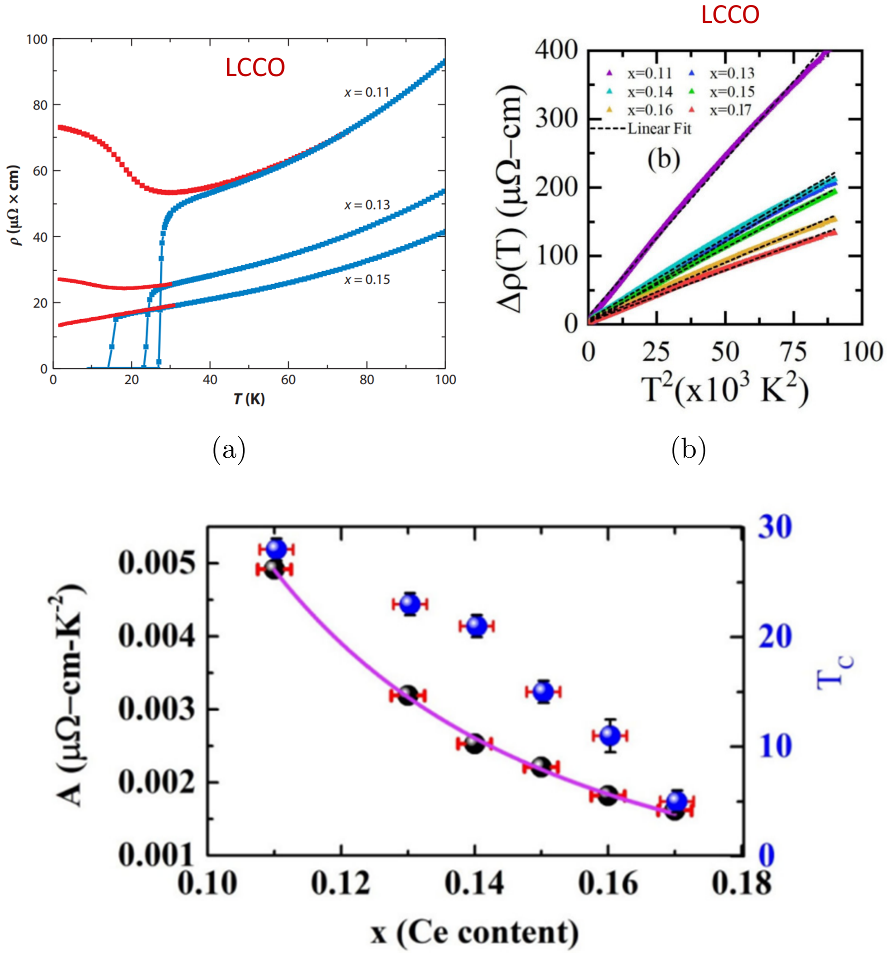

(a) (b)

(c)

Figure 1.4: (a) Crossover from linear temperature dependence at low temperature to Quadratic temperature dependency in EDC, as observed in LCCO (Source - [9]). (b) T^2 temperature dependency of resistivity at high temperature. Here, the resistivity has been plotted as a function of T^2. So, we are observing a linear trend (Source - [22]). (c) The coefficient of Quadratic temperature dependency and T_c show similar doping dependency (Source - [22]).

1.6 Sample dependency of T^2 Behaviour

At elevated temperatures, the resistivity of EDC typically exhibits a quadratic temperature dependence. This phenomenon has predominantly been observed in single crystals and thin films. However, this pattern shifts dramatically when considering the reported studies on polycrystalline samples of EDC. Contrary to expectations, polycrystalline EDC resistivity does not follow a quadratic trend; instead, it decreases with temperature post-superconducting transition. This deviation is particularly puzzling as, in near-optimal doping, both the ab-plane and c-axis resistivity in single crystals increases with temperature, suggesting that the behavior of polycrystalline samples cannot simply be explained as a combination of these directional tendencies.

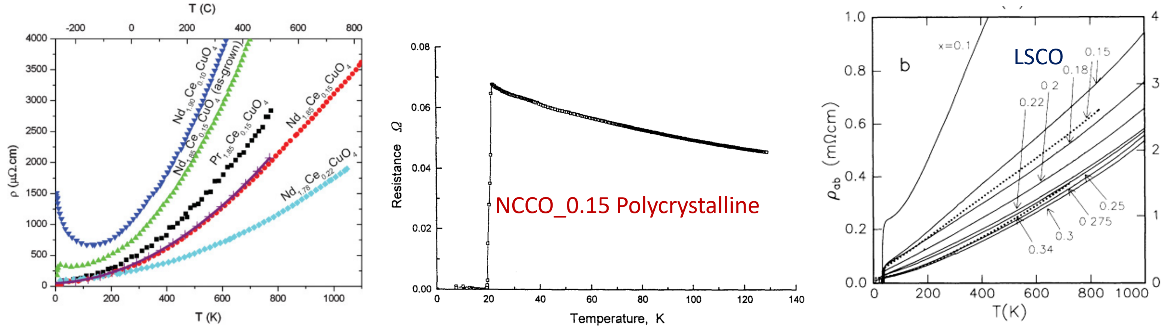

(a) (b) (c)

Figure 1.5: (a) Single Crystal of NCCO and the thin film of PCCO showing quadratic temperature dependency at high temperature (Source - [23]).(b) A polycrystalline sample of NCCO having a decreasing resistivity trend (Source - [24]). (c) Single crystal (dash line) and polycrystalline (solid line) samples of LSCO, which is an HDC, showing the same resistivity trend (Source - [25]).

Moreover, there are instances of single crystal samples that do not adhere to the expected quadratic temperature dependency, alongside thin films that only exhibit the T^2 dependency at higher temperatures following an initial decrease post superconducting transition. This variability hints at a lack of universality in the quadratic temperature dependency among different EDC samples. In contrast, the resistivity behavior of Hole Doped Cuprates (HDC) appears consistent across both single crystal and polycrystalline forms, showcasing similar temperature dependencies. This discrepancy in EDC is very puzzling. Even though this question has been raised many times [26] [27], we don't have an answer to this anomaly.

These observations raise critical questions regarding the sample-dependent nature of the T^2 resistivity behavior in EDCs. The anomalies suggest an underlying mechanism that current models do not fully capture. To delve into the roots and implications of this quadratic temperature dependency, a thorough investigation across the cuprate phase diagram, particularly focusing on polycrystalline samples such as Ce-doped Nd_2CuO_4, is essential. Such a study could illuminate the intrinsic properties driving the T^2 dependency in resistivity,

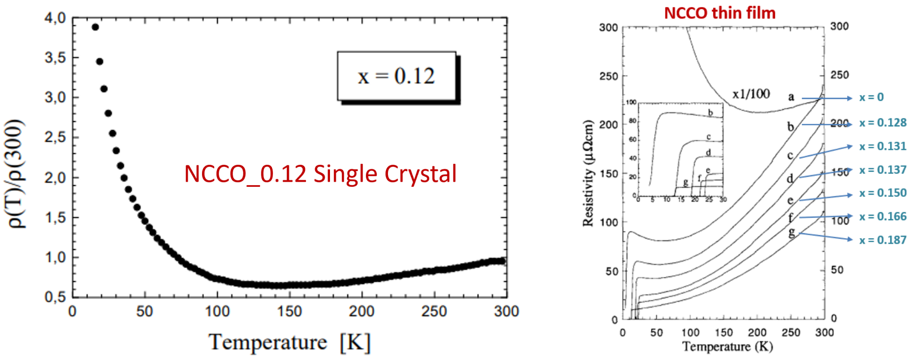

(a) (b)

Figure 1.6: (a) Reported Single crystal study of NCCO having no quadratic temperature dependency (Source - [28]). (b) The thin film of NCCO shows a decreasing trend after the superconducting transition and only has quadratic temperature dependency at a relatively higher temperature (Source - [29]).

offering new insights into the complex behavior of electron-doped superconductors.

1.7 Planckian Conjecture

The Planckian dissipation limit theory, or the Planckian conjecture, posits a fundamental bound on how quickly systems can dissipate energy in a quantum many-body system, described through the Planckian relaxation time, $\tau_{PL} \approx \frac{\hbar}{k_B T}$, where $\hbar$ is the reduced Planck constant, k_B is the Boltzmann constant, and T is the temperature. This conjecture has been instrumental in explaining the linear temperature dependence of resistivity observed in various systems, including cuprates, suggesting a universal mechanism for electron scattering and energy dissipation in strongly correlated materials beyond conventional Fermi-liquid theory [17].

In the context of resistivity, the Planckian dissipation limit provides a framework for understanding why the resistivity of HDC exhibits a T-linear behavior, extending beyond the Mott-Ioffe-Regel (MIR) limit where the conventional quasiparticle picture fails. This behavior reflects the fundamental energy dissipation rate of the system and is indicative of the existence of a state where electron scattering and interactions cannot be described within the conventional theoretical framework, challenging the existence of well-defined quasiparticles.

Furthermore, the Planckian conjecture extends its relevance to thermal transport properties, where thermal diffusivity measurements in cuprates and other strongly correlated systems have revealed that the inverse of thermal diffusivity (a measure of thermal resistivity) also follows a linear temperature dependence. These observations suggest that both electronic and phononic contributions to thermal transport reach the Planckian dissipation limit, highlighting the universal nature of this bound across different physical properties and domains.

The contrast in the high-temperature resistivity behavior between electron-doped cuprates (EDC), which exhibit a quadratic temperature dependence, and hole-doped cuprates (HDC), which maintain a linear temperature dependence, emphasizes the unique and complex nature of the electronic interactions in these materials. The transition from a T-linear to T^2 resistivity in EDCs raises significant questions about the underlying physics driving this behavior and the role of the Planckian dissipation limit. However, interestingly, even though the resistivity of EDC shows a T^2 behavior at high temperatures, thermal resistivity presents a T-linear trend. Comparing these two properties in parallel with the help of the Planckian dissipation limit framework will be fundamental to understanding the normal properties of Cuprates.

1.8 Thermal Resistivity

In the framework of Planckian dissipation, thermal diffusivity measurements on Cuprate superconductors have provided significant insights into the incoherent transport mechanisms that defy the traditional Fermi-liquid model. The Planckian relaxation time, $\tau_{PL} \approx \frac{\hbar}{k_B T}$, represents the shortest possible timescale for electron scattering processes in a quantum many-body system. This approach posits a universal bound on energy dissipation rates, implicating that the diffusion of both electrons and phonons can reach this fundamental limit, leading to a linear temperature dependence in the inverse thermal diffusivity, $D_Q^{-1} = aT + b$, where a and b are constants. This relationship, interpreted through the Planckian dissipation limit, suggests a universal behavior in the thermal transport of strongly correlated materials, pointing to a fundamental constraint on thermal relaxation processes. Here, the slope a reflects the Planckian relaxation bound, translating into a thermal diffusion velocity v_B, closely aligned with, yet slightly exceeding, sound velocity in the material. The intercept b, or D_0^{-1}, defines a boundary between coherent and incoherent quasiparticle regimes, highlighting the transition to a regime where traditional quasiparticle-based transport descriptions falter.

For Coherent transport in Insulators:

$$D_Q = \frac{1}{d} V_{ph}^2 \tau = s V_p^2 h \frac{\hbar}{k_B T} \quad \implies \quad D_Q^{-1} = aT \tag{1.1}$$

For incoherent transport in Cuprates:

$$D_Q^{-1} = aT + b = \left(\frac{\hbar}{k_B T} + D_0^{-1} \right) = \left(\frac{\hbar}{k_B T} \right) + \left(\frac{\hbar}{3 m_D} \right)^{-1}$$

The analysis within the Planckian dissipation limit theorem for cuprates suggests that both the electrons and phonons reach the Planckian bound, which is very unusual. As a result, quasi-particle pictures for both the electron and phonon are no longer applicable directly.

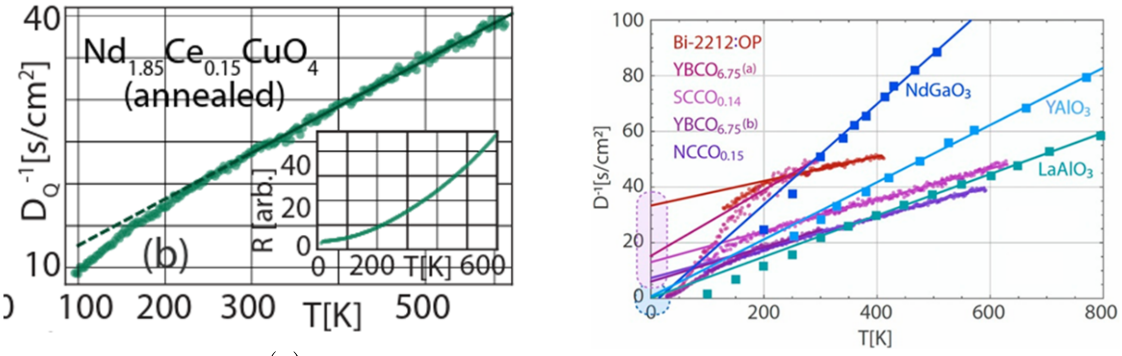

(a)

(b)

Figure 1.7: (a) Experimental data on NCCO single crystal showing T-linear behavior of inverse thermal diffusivity or the thermal resistivity (Source - [30]). (b) Thermal diffusivity study on different families of Cuprates, presenting the signature of incoherent transport, which is defined by the intercept on the linear fitting of Thermal resistivity ([31]).

1.9 Electron Phonon Soup

The introduction of the concept of an overdamped electron-phonon fluid emerges as a pivotal development in addressing the incoherent transport mechanisms in cuprate superconductors, where the quasi-particle picture does not seem to be accurate. Traditional models, grounded in Fermi-liquid theory, fall short in explaining the observed thermal and electrical transport behaviors at high temperatures, particularly the linear temperature dependence of resistivity and its deviation from the Mott-Ioffe-Regel limit. This deviation calls into question the validity of the quasiparticle framework in these regimes, necessitating a novel theoretical approach.

The overdamped electron-phonon fluid model provides a compelling explanation for these phenomena. By considering the interactions between electrons and phonons not as discrete, well-defined quasiparticles but as a collective, incoherent fluid, this model accounts for the linear temperature dependence observed in the inverse thermal diffusivity, as well as the resistivity of cuprate superconductors. This approach aligns with the Planckian dissipation framework, where both electrons and phonons are subject to a universal relaxation time bound, $\tau_{PL} \approx \frac{\hbar}{k_B T}$, indicative of the fastest possible rate of energy dissipation in any system.

The significance of the overdamped electron-phonon fluid model lies in its ability to unify the thermal and electrical transport properties under a common theoretical umbrella, thereby providing a coherent explanation for the Planckian bound's applicability across different physical domains.

While the overdamped electron-phonon fluid framework successfully explains the linear temperature dependence of resistivity and the inverse of thermal diffusivity in cuprate superconductors, it notably does not address the quadratic (T^2) resistivity behavior observed in Electron Doped Cuprates (EDC). This omission highlights a gap in the theory's applicability to all facets of cuprate behavior. Furthermore, there exists a significant void in experimental research covering the entire phase diagram, particularly in terms of thermal diffusivity measurements across different doping levels and temperature ranges. To bridge this gap, our research focuses on conducting a thorough investigation of thermal transport in polycrystalline samples of NCCO, spanning the entirety of the phase diagram.

In this thesis, we explored polycrystalline samples of NCCO across the entire phase diagram of EDC. The comprehensive methodology encompassing sample synthesis, characterization, and the measurement of physical properties is elaborated in the subsequent sections. Our objective was to examine the sample-dependent T^2 resistivity behavior of EDC by carefully controlling the sample synthesis condition. This examination enabled us to confirm the consistent presence of the T^2 behavior across the samples, although the microstructures of the samples significantly influence their observability. Concurrently, we delved into the thermal resistivity of these samples under the Planckian dissipation limit to parallel our investigation with electrical resistivity studies, aiming to elucidate the interplay between electronic and phononic transport. The investigation of thermal resistivity was intended to demonstrate a correlation between the T^2 electrical resistivity behavior and the T-linear thermal resistivity behavior.

Chapter 2

EXPERIMENTAL TECHNIQUES

The samples for our study have been synthesized following the solid-state synthesis protocol. We performed the room temperature powder X-ray diffraction (XRD) and SEM-EDX measurements on our samples and confirmed the purity. We deployed the Thermogravimetric analysis (TGA) scan under the $Ar - H_2$ environment to get the Oxygen Content of our samples. We utilized our in-house high-temperature setup to measure the resistivity of our samples and verified the results by conducting measurements on the commercial Linseis LSR setup. Thermal diffusivity measurements were carried out on the Laser Flash Analysis (LFA) setup, spanning temperatures up to $700K$ with step increments of $25K$. The details of all these processes will be discussed in this section.

2.1 Solid State Sintering

Solid-state synthesis is a widely adopted technique for preparing transition metal oxides (TMOs), particularly those with complex crystal structures and high melting points. This method involves carefully mixing solid precursors, such as oxides, carbonates, or nitrates, in the desired stoichiometric ratios, followed by a series of heat treatment steps.

The synthesis process typically starts with weighing and thoroughly mixing the precursor materials to ensure homogeneity. The mixed powder is then subjected to a calcination step, where it is heated to a specific temperature to initiate solid-state reactions and promote the formation of intermediate phases.

After calcination, the powder is often palletized by applying pressure to increase its density and improve diffusion kinetics during the subsequent sintering step. The palletized or powder sample is then sintered at high temperatures, typically above 900°C, for an extended period. This high-temperature treatment facilitates solid-state diffusion processes and chemical reactions, leading to the formation of the desired phase with the targeted crystal structure and density.

The sintering temperature and duration are crucial parameters that can be optimized. In some cases, an additional annealing step may be performed after sintering to improve crystallinity and relieve lattice strain.

It is important to note that the specific synthesis parameters, such as precursor ratios, calcination and sintering temperatures, and durations, may vary depending on the targeted Oxide system and the desired properties. Careful optimization and characterization of the synthesized materials are essential to ensure phase purity, crystallinity, and the desired physical properties.

In this work, We synthesized several Ce-doped Nd_2CuO_4 with the chemical formula, $Nd_{2-x}Ce_xCuO_4$ following this procedure for different x values. In this particular sample, we have to perform an Ar-annealing treatment to make the samples superconducting.

2.2 Powder X-ray Diffraction

Powder X-ray diffraction (PXRD) is a powerful and widely employed analytical technique that enables researchers to determine the crystal structure of a crystalline material. It involves exposing a powdered sample to an X-ray beam and measuring the pattern of diffracted X-rays produced by the sample. The diffraction pattern contains valuable information about the atomic arrangement within the crystal structure of the sample in specific atomic planes.

The fundamental principle behind powder X-ray diffraction lies in Bragg's law, which states that the diffraction of X-rays by a crystal lattice occurs when the X-rays interact with the planes of atoms in the lattice in a way that their path difference equals an integer multiple of the wavelength of the X-ray used. This condition can be expressed mathematically as:

$$2d\sin(\theta) = n\lambda \tag{2.1}$$

Where d is the inter-planar spacing (distance between adjacent crystal planes), θ is the angle of incident X-rays with the plane of the sample, n is the order of diffraction, and λ is the wavelength of the X-ray used.

In experimental setups, X-rays are generated from a target (e.g., Cu in our case with a wavelength of 1.5405 Å) through an X-ray tube or X-ray generator. Electrons are accelerated towards the target by a high voltage, and when they collide with the target atoms in the anode, X-rays are emitted. The energy of the X-rays produced is determined by the difference in energy levels between the electronic shells involved in the transition, and the X-ray spectrum has characteristic peaks corresponding to the different transitions in the target atoms. For example, $K\alpha$ and $K\beta$ are the most intense peaks in the characteristic spectrum, corresponding to L and M shells to the innermost shell K, respectively.

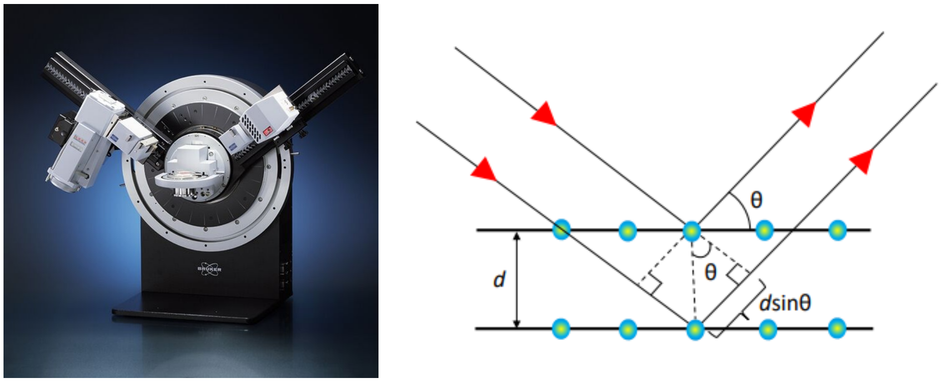

(a) (b)

Figure 2.1: (a) The XRD diffractometer, which has been used to perform PXRD of all of our samples (Source - [32]). (b) This image presents the Schematic diagram of Bragg's condition for X-ray diffraction by crystalline material.

In a typical powder XRD experiment, a powdered sample is placed on a sample holder and then exposed to a beam of X-rays. The X-rays interact with the atoms in the crystal lattice and produce a pattern of diffracted X-rays that are collected by a detector. The pattern of diffracted X-rays is then analyzed using software programs to determine the crystal structure of the sample.

One of the key advantages of PXRD is that it is a non-destructive technique, meaning that the sample is not destroyed during the analysis. This makes it an ideal technique for studying materials that are rare or difficult to synthesize. Additionally, because PXRD is a bulk technique, it can be used to analyze a large number of samples quickly and efficiently.

For this project, room temperature and high-temperature Powder X-Ray Diffraction was conducted using a Bruker D8 Advance Powder X-Ray Diffractometer. To begin, the prepared samples were ground into a fine powder and then mounted onto a glass slide. This prepared sample was then placed into the diffractometer. It is worth noting that the glass slide is amorphous and does not contribute to the diffraction patterns. The obtained diffraction patterns were then compared to the standard patterns recorded in different international crystallographic databases.

The XRD setup typically consists of an X-ray source, a sample holder, and a detector. The schematic representation provided in the image clearly illustrates the essential components of the diffractometer and the geometric arrangement that facilitates the observation of Bragg's law.

2.3 SEM-EDX

Scanning Electron Microscopy (SEM) is a cornerstone technique in material science for investigating surface structures, where it provides a detailed view of sample morphology, grain size, and the grain boundaries within a sample. By using a focused electron beam and capturing the secondary electrons released from the sample's surface, SEM can render intricate images that reveal the granular architecture of materials. These high-resolution images allow for a meticulous examination of grain boundary structures, which are critical in understanding the properties and behavior of materials. These SEM images have been used in this thesis to understand the grain boundary contribution to the physical transport properties.

Energy Dispersive X-ray Spectroscopy (EDX) analysis, often performed in conjunction with SEM, provides the chemical composition of the sample being studied. EDX is pivotal in quantifying the stoichiometry, or elemental ratio, of the components within the material. By bombarding the sample with electrons and measuring the characteristic X-rays emitted, EDX can pinpoint the presence and proportion of elements, thus offering insights into the sample's overall stoichiometric balance. This information is precious when assessing the purity and homogeneity of a material, as well as identifying phases and inclusions within the grain boundaries.

In material analysis, the synergy between SEM and EDX becomes particularly powerful. SEM allows researchers to visualize the morphology and structure of grain boundaries, which are known to affect the mechanical and thermal properties of materials. Meanwhile, EDX contributes a complementary layer of information by revealing the elemental composition at these boundaries, providing clues about the diffusion of elements and the formation of various phases within the crystalline lattice.

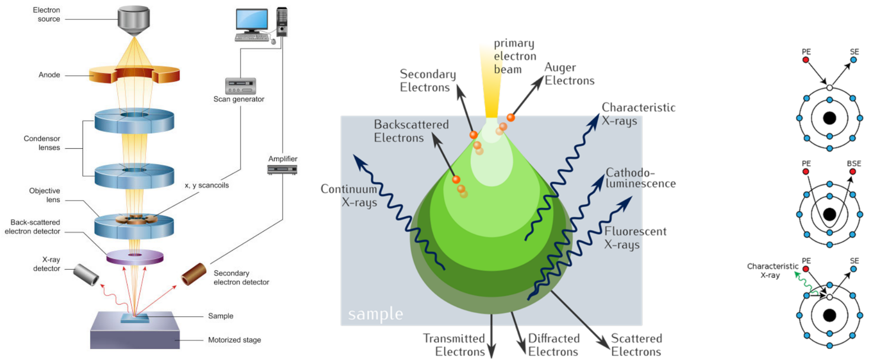

(a) (b)

Figure 2.2: (a) The schematic diagram of Scanning electron microscope. (Source - [33]). (b) This image presents the different electron excitations that occur when primary electrons interact with the sample (Source - [34]).

The technical capabilities of SEM-EDX are designed to cater to the exacting demands of modern material science. With the ability to magnify features up to 50,000 times, SEM can reveal even the subtlest details at the boundary level. Concurrently, EDX offers a precise stoichiometric analysis down to the sub-micron level. Together, these techniques provide a comprehensive understanding of the sample's structural and chemical attributes, forming a complete picture crucial for materials research and engineering applications. The findings derived from SEM images and EDX data are instrumental in validating theoretical models and provide a foundational understanding that guides the development of materials with desired properties and functionalities.

The SEM analysis conducted for this thesis used a field emission secondary electron microscope (FESEM) from Zeiss Ultra Plus, Germany. This FESEM setup equipped an EDS analysis probe with a 20 mm^2 detector from Oxford Inca that offers an energy resolution of 129 eV. Freshly broken, relatively flat sections of the sintered pellets were stuck to a double-sided carbon tape and loaded onto an SEM stub. For each sample, multiple areas were randomly selected to examine their morphology and composition. As the EDS analysis is not sensitive to lighter elements, such as - Hydrogen and oxygen, we only used the relative atomic percentage of the heavier atoms for the quantitative estimation of atomic percentage.

2.4 Thermogravimetric Analysis (TGA)

Thermogravimetric Analysis (TGA) is a widely employed technique to study the thermal behavior of materials by measuring the weight change of a sample as a function of temperature or time. This technique is particularly useful for investigating processes such as decomposition, oxidation, reduction, and dehydration, which involve mass changes.

In the context of our work, TGA was used methodically to determine the oxygen content of the sample by reducing it in an argon-hydrogen environment. This process involves exposing the sample to a controlled atmosphere of $Ar - H_2$ gas mixture while heating it at a specific temperature ramp or isothermal condition. As the sample is heated, the oxygen present in the material is expected to react with the hydrogen gas, forming water vapor, which is subsequently removed from the system. The weight loss observed during this reduction process corresponds to the amount of oxygen initially present in the sample.

The experimental setup, as shown in figure 2.3, consists of a highly precise microbalance suspended within a furnace chamber. The sample with weight ranging from 15-20 mg is placed in a freshly glowed alumina crucible, which is hung from the microbalance arm, allowing continuous monitoring of the sample's weight during the heating and gas flow cycles. The furnace chamber is equipped with gas inlets and outlets, enabling the controlled flow of the desired gas atmosphere. The sample chamber was purged and sealed 6 times before starting the heating cycle to remove oxygen from the sample chamber, as the used W-type carrier is highly prone to oxidation in a trace amount of Oxygen at higher temperatures.

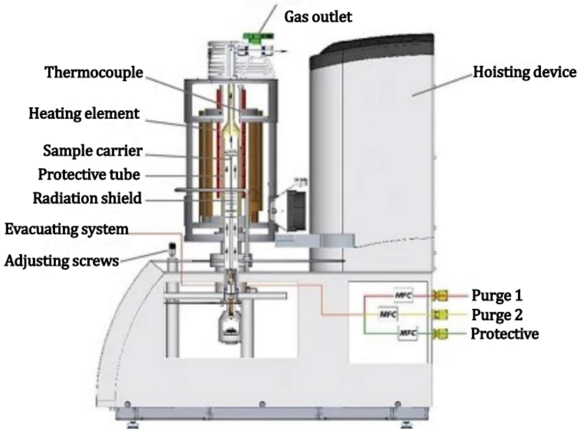

Figure 2.3: Schematic representation of the Netzsch STA 449 F1 TGA setup. (Source - Netzsch website [35])

Then, the samples are decomposed completely using a reducing atmosphere of $Ar-H_2(10\%)$ in an isotherm run at 600 °C. The oxygen content has been estimated by back-calculating the weight loss.

By monitoring the weight loss profile of the sample during the reduction process, the oxygen content can be quantified based on the stoichiometry of the reaction and the known initial weight of the sample. This Oxygen content information is crucial for understanding the physical properties of any oxide.

2.5 High Temperature Hall Setup

The homebuilt high-temperature Hall setup is designed to measure electrical resistivity and Hall effect in samples from room temperature up to 750 K with high precision and temperature stability of ±0.01 K. The key components, which are shown in figure 2.4 include a localized heating sample holder, quartz sample chamber, bipolar electromagnets, and lock-in amplifier-based electronic circuitry

The sample holder is a stainless-steel cuboidal block with a cartridge heater for resistive heating and a Pt100 sensor for temperature sensing/control using a Cryocon temperature controller. The sample is placed on an aluminum nitride (AlN) base, which has high thermal conductivity for efficient heat transfer but low electrical conductivity to isolate the sample.

Ceramic adhesive secures the sample on the AlN base.

Three types of sample contacts are used: pressure contacts (PC) made from bent stainless-steel sheets for point contacts, pressure contacts with silver paint (PCS), and gold wires with silver paint (GW). The sample chamber is a quartz tube attached to an electromagnetic cage, allowing measurements in inert gas or high vacuum (≤2 Pa). The sample holder is aligned parallel to the magnetic field poles inside the chamber.

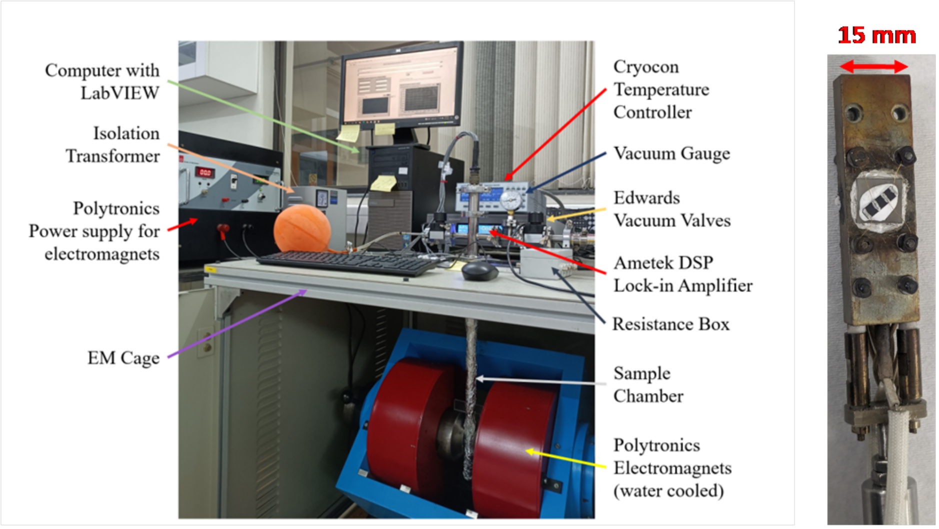

Figure 2.4: Homebuilt high-temperature hall setup and the sample stage with our sample loaded in four probe configuration for resistivity measurement.

Bipolar electromagnets provide magnetic fields up to 1 T, controlled by an NI DAQ card. A lock-in amplifier obtains high-precision Voltage data for resistivity and hall measurement using an alternating current to eliminate offsets/noise. A homebuilt switch system with an Arduino-controlled relay switches between current and voltage probes.

The setup's accuracy is validated by comparing resistivity and Hall data with a commercial Linseis LSR setup and literature values, showing excellent agreement. The high-temperature stability of ±0.01 K enables precise measurements. Overall, this automated setup provides reliable high-temperature electrical transport data using versatile sample contacts on a localized heating sample holder with optimized electronic measurement circuitry.

The setup's accuracy is validated by comparing resistivity and Hall data with a commercial Linseis LSR setup and literature values, showing excellent agreement. The measured data on our samples matches the Linseis LSR data well. The samples are loaded onto an aluminum nitride plate using a ceramic paste, which is attached to the sample holder using silver paint. The GW contacts, made with RS Pro silver paint baked under high-intensity light for an hour, are mainly used for measurement purposes. The very high-temperature stability of ±0.01 K enables precise measurements and acquisition of high-quality data.

2.6 Linseis LSR Setup

The Linseis LSR-3 is a versatile instrument designed to simultaneously measure the resistivity and Seebeck coefficient of materials across a broad temperature range, typically up to 1000°C. The setup is engineered to deliver precise control over the temperature gradient applied to the sample, a feature critical for observing the variable thermoelectric behavior of materials under study. In the resistivity measurement mode, a constant current is passed through the sample while the voltage drop is measured across it. For Seebeck coefficient measurements, a temperature difference is induced across the sample, and the resulting voltage difference is recorded. The meticulous design of the LSR-3 ensures the fidelity of these measurements by minimizing thermal losses and external interference.

At the heart of the system's design is the sample holder, which securely positions the sample between two temperature-controlled plates. This configuration is essential for maintaining a stable and known temperature gradient along the sample. The standard LSR-3 setup utilizes normal pressure contacts to hold the sample in place, facilitating electrical contact without compromising the sample's integrity. This aspect of the design allows for a broad application across various materials, from metals and semiconductors to complex compounds that exhibit a range of electrical and thermal properties.

In the context of our work on electron-doped Cuprates, the LSR-3 required a customized approach. Our electron-doped Cuprates samples presented a challenge, as their unique properties rendered the standard pressure contacts ineffective. To address this, we sputtered our sample bars with platinum, as shown in the figure 4.6a. By integrating this tailored technique into the Linseis LSR-3's robust framework, we were able to precisely measure the resistivity and Seebeck coefficient of the electron-doped Cuprates, providing significant

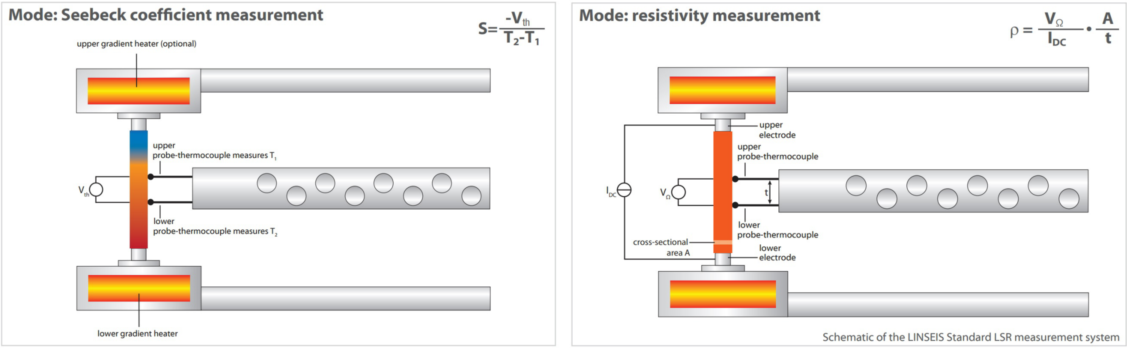

(a) (b)

Figure 2.5: Schematic diagram for measuring Seebeck coefficient(a) and resistivity(c) in Linseis LSR-3 setup (Source - Linseis website [36].

contributions to our understanding of their properties.

2.7 Linseis LFA Setup

The Laser Flash Analysis (LFA) technique is an essential tool for the measurement of thermal diffusivity and specific heat capacity of various materials. It operates on the principle of transient thermophysical analysis: an energy pulse from a laser heats one side of a planar sample, and the resulting temperature rise on the opposite side is recorded over time. The higher the thermal diffusivity, the quicker the temperature on the rear face rises. This time-dependent temperature increase is the core data from which thermal diffusivity, conductivity, and specific heat are calculated.

LFA's precision stems from its controlled experimental setup, where the sample is typically loaded with layers of graphite on each side. During an LFA measurement, a laser pulse is directed at the front face of the sample, and a detector—often an infrared sensor—monitors the temperature rise on the rear face. This setup minimizes heat loss and ensures that the temperature rise is primarily due to the laser pulse.

In Laser Flash Analysis (LFA), the half-rise time, $t_{1/2}$, is pivotal, denoting the time for the sample's rear face to achieve half of the maximum temperature increase post-laser pulsing. This parameter is integral to determining thermal diffusivity through Parker's analysis, which corrects for finite pulse duration and heat loss. Parker's method employs $t_{1/2}$

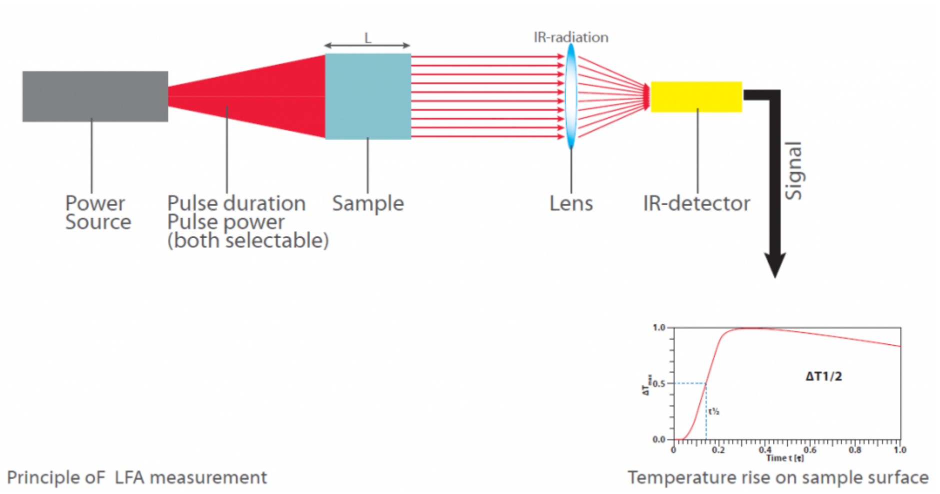

Figure 2.6: Schematic diagram presenting the working principle of LFA (Source - Linseis website [37]).

in a model fitting the temperature-time curve, yielding a precise diffusivity measure even with complex thermal behaviors, ensuring accuracy in materials that exhibit non-standard thermal responses.

The data acquired through LFA can offer significant insights into the materials' intrinsic properties. The thermal diffusivity of our sample has been extensively investigated to understand the Planckian conjecture in thermal diffusivity inverse.

Chapter 3

SYNTHESIS AND CHARACTERIZATIONS

This chapter will discuss the sample synthesis protocols and their detailed characterizations using XRD, SEM-EDX, and TGA in $Ar - H_2$ environment.

3.1 Synthesis

The Poly-crystalline sample of $Nd_{2-x}Ce_xCuO_4$ (NCCO) was synthesized by the conventional solid-state reaction method. We used high-purity preheated Nd_2O_3, CeO_2, and CuO in a stoichiometric ratio and ground them for forty-five minutes before heating. The sample has been synthesized in multiple steps. In 1st sintering, we kept the sample at 950 degC for 24 hours. After that, we ground the powders for 1hr and made pallets of 13mm diameter using 10-ton pressure in our KBr press. Then, the sample has been heated at 1100 degC for 40hr for the 2nd sintering. With these two steps, we can get a pure NCCO phase. The 1st sintering and 2nd sintering conditions have been presented in figure 3.1a and 3.1b.

However, to get superconductivity in these samples, we have to Argon anneal these samples. The exact effect of this Ar-annealing in the sample is twofold. It reduces the oxygen content by 1-2%, and there is migration of oxygen to the apical position of Copper during this annealing process. Their detailed implications for the onset of superconductivity have been discussed in this PRB publication [38]. So, to obtain the superconductivity, we also Ar-annealed our samples at 1050 degC for 48 hr at an Argon flow rate of 1 bubble/s, as mentioned in the figure 3.1c.

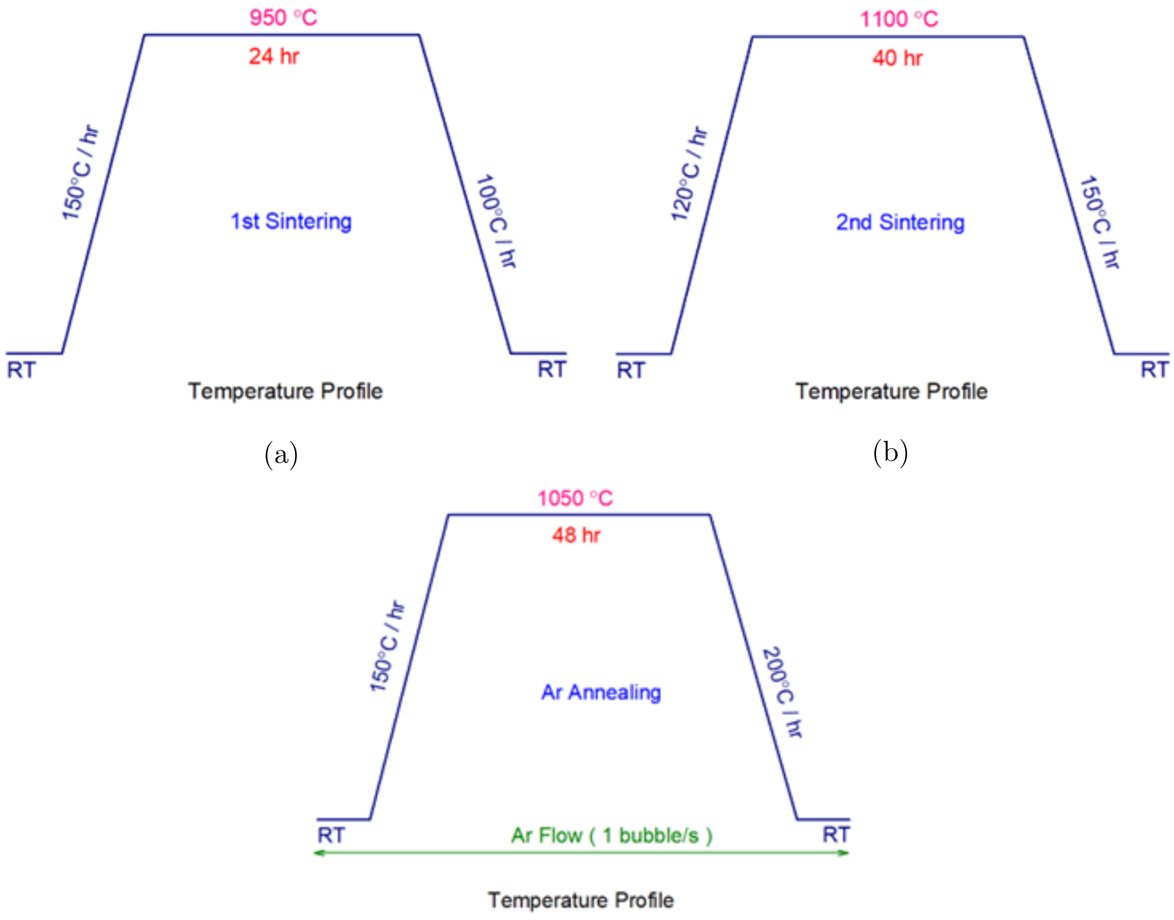

(a) (b)

(c)

Figure 3.1: Heating profile for 1st sintering(a), 2nd sintering(b), and Ar-annealing(c) for the sample synthesis.

3.2 Nomenclature

In this section, We will introduce the naming scheme of our samples. This nomenclature will be followed throughout this whole thesis. This nomenclature is based on the sample synthesis condition. The general name is $NCCO\_x\_M$, where NCCO refers to the sample $Nd_{2-x}Ce_xCuO_4$, x refers to the doping coefficient or the Cerium stoichiometry, and M refers to the sample synthesis condition. Table 1 summarizes all the sample preparation conditions with details and their naming scheme.

Name	Condition	Details
$NCCO\_x\_U$	Unannealed	As grown sample, kept after the 2nd Sintering.
$NCCO\_x\_AA$	Ar-Annealed	Sample obtained by Ar-annealing the unannealed pallets.
$NCCO\_x\_AS$	Ar-Sintered	An unannealed sample is ground as fine powders and cold-pressed to form a pellet, and then the pellet is Ar-annealed.
$NCCO\_x\_VA$	Vacuum Annealed	Unannealed sample is vacuum annealed inside an ampoule.
$NCCO\_x\_HP$	Hot Pressed	Unannealed sample is ground into fine powders followed by hot-pressing.
$NCCO\_x\_HP\_Sint$	Hot Pressed Sintered	Hot Pressed sample is sintered following the 2nd Sintering condition.

Table 3.1: Sample Nomenclature

3.3 Characterizations

3.3.1 X-Ray Diffraction

The powder X-ray diffraction data is taken on the polycrystalline samples of NCCO using our lab-based Bruker D8 Advance Powder X-Ray Diffractometer. Figure 3.2a and figure 3.2b presents the XRD pattern of all the unannealed samples and the Ar-Annealed samples, respectively. The obtained XRD pattern for all the samples is in good agreement with the simulated pattern for NCCO, suggesting the pure phase. It also does not contain any impurity phase.

3.3.2 Lattice Parameters

We calculated the lattice parameter from the XRD peak positions using Unit Cell software. The value and trend of lattice parameters as a function of cerium content(x) also match well with the literature trend [39]. With the introduction of more and more cerium in the lattice, the c-axis reduced significantly due to the lower atomic radius of cerium and the layered nature of these compounds. The change in the a-axis is negligible compared to the change in the c-axis. The Annealing process, which is necessary for the superconducting

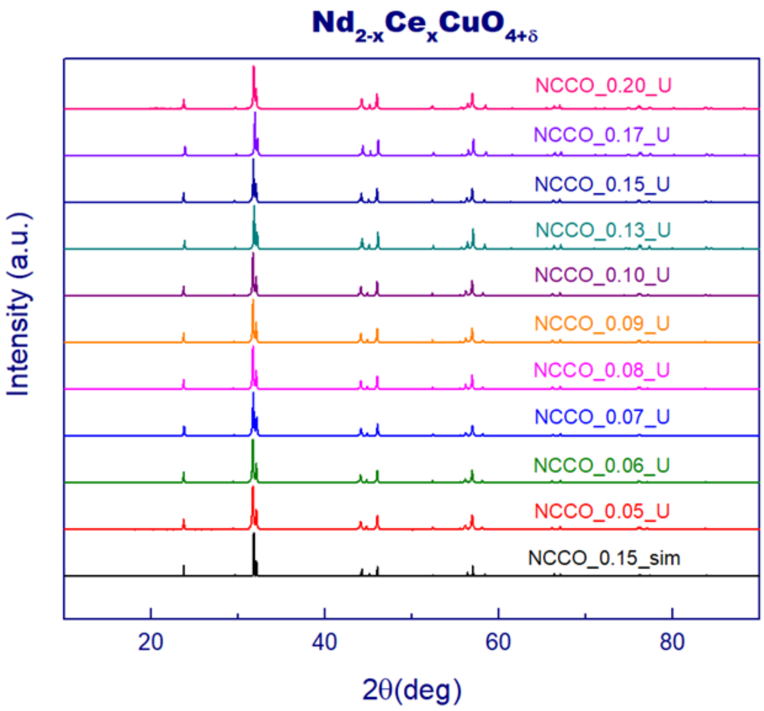

(a)

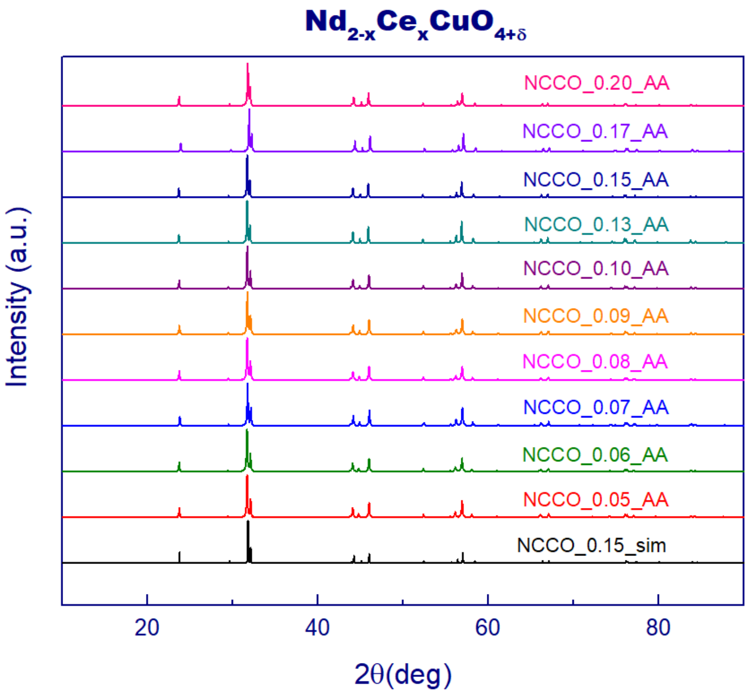

(b)

Figure 3.2: XRD pattern of all the unannealed samples (a) and Ar-Annealed samples (b) presenting pure NCCO phase.

state, does not affect the lattice parameters significantly.

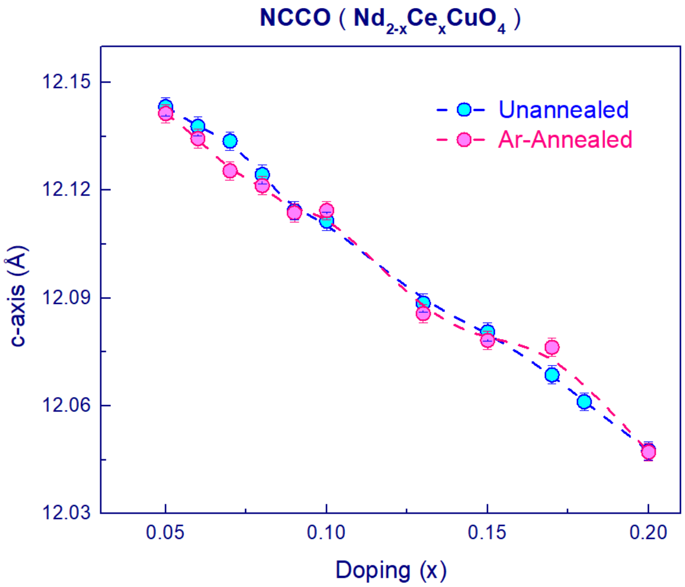

(a)

Figure 3.3: The lattice parameter (c-axis) trend of our samples as a function of Cerium content has been presented in this figure

3.3.3 SEM-EDX

The Scanning Electron Microscopy (SEM) images of the sample and Electron-Dispersive X-ray spectroscopy (EDX) analysis also confirmed the phase purity and the doping percentage. Figure 3.4a, 3.4b presents the SEM images of some of our samples, indicating a uniform distribution without any secondary phase contrast. This suggests that these samples are phase pure. The morphology of the freshly broken pallets can be seen in Fig. 3.4b and Fig. 3.4d. We observe layered morphology in the sample $NCCO\_0.13\_AA$, as depicted in the figure 3.4d. This is in accordance with the layered structure of these samples. Another important thing to notice is that the grain size has changed depending on the sample conditioning. The sample $NCCO\_0.13\_U$ (figure 3.4b) has less grain boundary compared to the Ar-Sintered sample of the same doping, $NCCO\_0.13\_AS$ (figure 3.4c). This observation is crucial to understand the physical properties of these samples. We will explore the effect of these grain boundary distributions in detail in the next chapter.

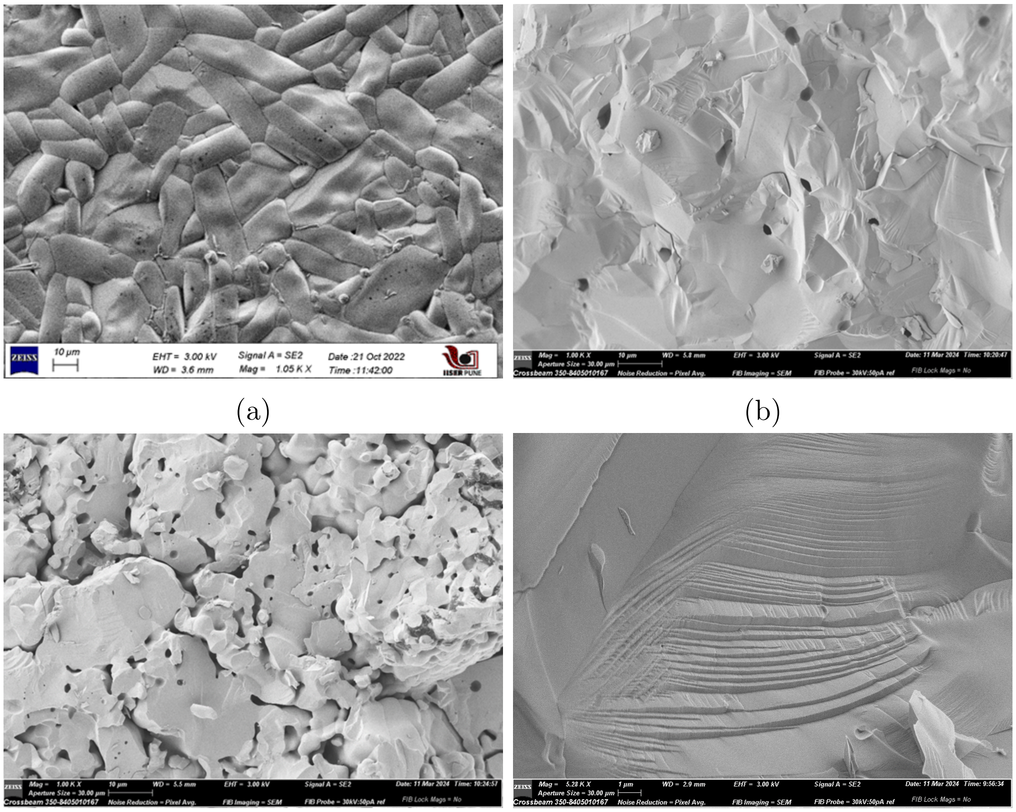

(a) (b) (c) (d)

Figure 3.4: (a) SEM images of the $NCCO\_0.07\_U$ showing the distribution of grains. The morphology of the freshly broken pallet of $NCCO\_0.13\_U$ sample (b) and $NCCO\_0.13\_AS$ sample (c). (d) Stacking of 2D planes in the sample $NCCO\_0.13\_AA$ sample.

Detailed EDX analyses were also conducted on several samples, with EDX scans performed at various positions on each sample. By averaging these scans, we determined the samples' stoichiometry. The stoichiometry obtained from the EDX measurements closely matches the expected stoichiometry of our samples, indicating their high quality.

3.3.4 TGA

We have used TGA methodically to get the oxygen content of our samples. We performed the TGA in an $Ar - H_2(10\%)$ flow following a heating profile (shown in figure 3.5a) up to 600 degC. The objective was to subject the sample to a reduction in an $Ar - H_2$ environment, followed by calculating the oxygen stoichiometry based on the observed weight loss during this process. The TGA end products have been confirmed by performing XRD scans on the reduced powder. The end products are found to be Nd_2O_3, CeO_2, and Cu from the Xrd peak matching as presented in figure 3.5b. By the stoichiometric balanced reaction of the starting compound and the reduced end products, we can back-calculate the Oxygen content in the sample. The stoichiometric reaction can be written as below:

$$Nd_{2-x}Ce_xCuO_{4+\delta}+(1+\delta-\frac{x}{2})H_2 \longrightarrow (1-\frac{x}{2})Nd_2O_3+xCeO_2+Cu+(1+\delta-\frac{x}{2})H_2O\uparrow \quad (3.1)$$

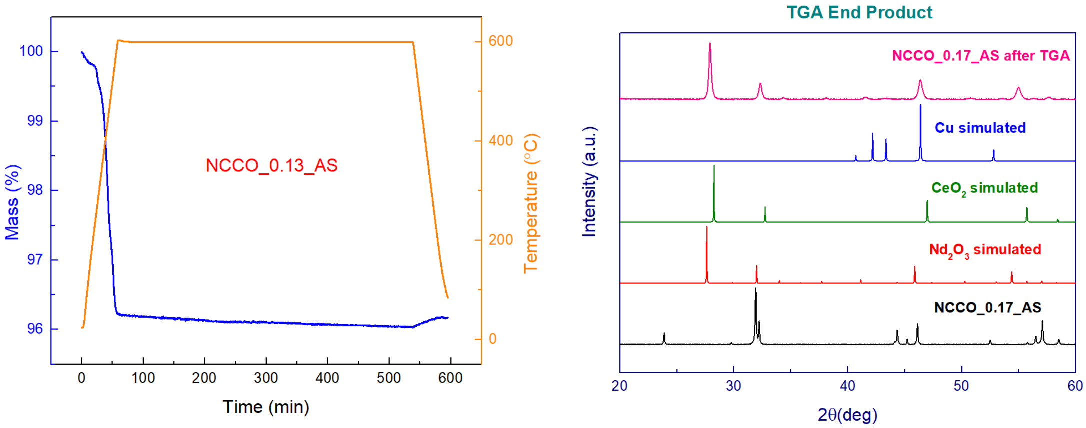

(a)

(b)

Figure 3.5: (a) TGA heating profile (right) and corresponding mass loss curve (left) have been presented for the sample $NCCO\_0.13\_AS$. (b) XRD of the TGA end product suggests the reduced samples to be Nd_2O_3, CeO_2, and Cu.

From the mass loss captured during the TGA experiment, we can estimate the Oxygen content of the sample. If the mass loss is $\Delta m\%$, then the oxygen content is given by the equation 3.2.

$$\delta = \frac{416.03\lambda \; - \; 4.12\lambda x - 16 + 8x}{16 - 16\lambda} \qquad \text{where, } \lambda = \frac{\Delta m}{100} \qquad (3.2)$$

The calculated oxygen content provides a reasonable estimate. However, for a more precise estimation, extending the TGA to higher temperatures might be necessary while paying careful attention to sample preparation. As we are working with polycrystalline samples, they can have pores that might absorb moisture. So, we kept the powder sample in an oven for at least half an hour before loading it in the TGA setup. The TGA curves corresponding to different samples have been presented in the figure below, and the calculated oxygen stoichiometry is presented in Table 2.

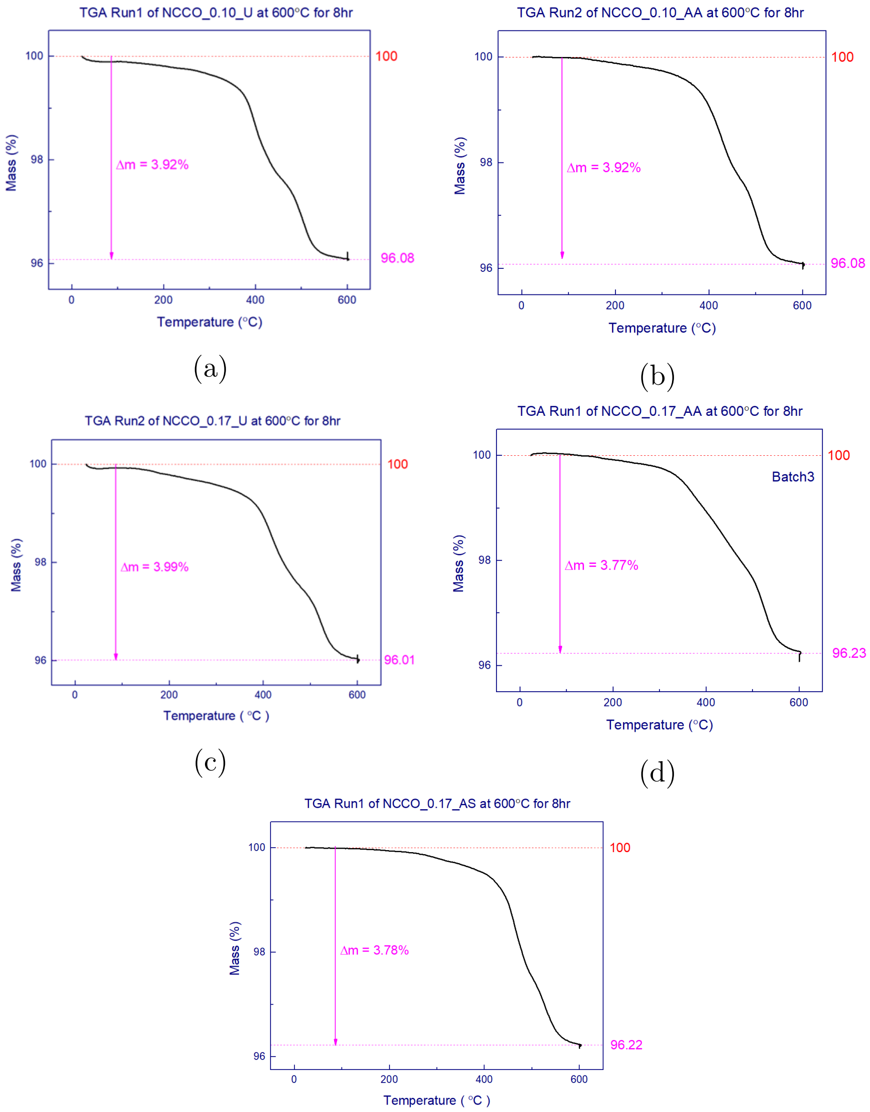

(a) (b) (c) (d) (e)

Figure 3.6: TGA Curves of different samples presenting mass loss during the TGA in $Ar-H_2$ environment. (a) $NCCO\_0.10\_U$, (b) $NCCO\_0.10\_AA$, (c) $NCCO\_0.17\_U$, (d) $NCCO\_0.17\_AA$, (e) $NCCO\_0.17\_AS$

We performed the TGA of the same sample before and after Ar-Annealing. The change in the oxygen content due to Ar-annealing treatment is roughly $1-2\%$, which matches with the literature [38]. Our results support the idea that during the Ar-annealing, the oxygen content does not change that much.

The TGA curves for the unannealed (figure - 3.6a, 3.6c) and Ar-Annealed (figure - 3.6b, 3.6d) sample present a slight difference. The TGA curve is much smoother in the

Sample	Unannealed	Ar-Annealed	Oxygen Loss(%)
$NCCO\_0.07$	4.09	4.06	0.73
$NCCO\_0.10$	4.08	4.05	0.74
$NCCO\_0.13$	4.06	4.05	0.25
$NCCO\_0.15$	4.03	4.00	0.74
$NCCO\_0.17$	4.13	4.07	1.45
$NCCO\_0.20$	4.04	4.03	0.25

Table 3.2: Calculated Oxygen Content of all the samples.

Ar-Annealed samples compared to the step-like characteristics in the unannealed sample around 500 °C. This might be due to the change in the position of the oxygen in the lattice, as argued by Guarino et al. [38]. Variations in the oxygen position may result in alternate reduction pathways, potentially resulting in subtle differences in the TGA curve.

Figure 3.6e presents the TGA curve for the Ar-Sintered sample, $NCCO\_0.17\_AS$. The mass loss in the Ar-Annealed sample (3.6d) and Ar-Sintered sample (3.6e) is roughly the same. That implies both of these samples have the same oxygen content. This outcome is anticipated, given that they were annealed in Argon for identical durations at the same flow rate. So, the key difference between the Ar-Annealed sample and the Ar-Sintered sample is their microstructure. In the next chapter, we will see how these different microstructures affect the physical properties of the sample, and we will also use their SEM images (Shown in figure 3.4b and 3.4c) to understand their grain boundary structures.

To summarise, we have synthesized NCCO samples with varying cerium content and performed Ar annealing to get superconductivity. The XRD, SEM-EDX analysis suggests that we have pure samples without any impurity phase. The calculated lattice parameters also match the literature values. The Thermogravimetric analysis of our samples in $Ar - H_2$ environment suggests that we have oxygen content close to 4, and the Ar annealing reduces the oxygen content by $1 - 2\%$. We have good-quality polycrystalline samples of NCCO to study their physical properties in detail.

Chapter 4

QUADRATIC TEMPERATURE DEPENDENCE OF RESISTIVITY

In this chapter, we will discuss the electrical transport properties (Resistivity, Seebeck Coefficient) of our samples. In our electrical resistivity data, we have observed interesting features. The detailed analysis of our experimental data provided insight into the sample dependence property of the high-temperature resistivity characteristics of EDC. The analysis of the Seebeck coefficient and the conditioning of the sample using Hot Press supports our resistivity analysis and physical understanding.

4.1 Low Temperature Resistivity Behaviour

This section will discuss the low-temperature resistivity behavior of our samples. The low-temperature resistivity behavior will confirm the superconducting nature of our samples and how it is related to the Ar-annealing process.

Figure 4.1a presents the resistivity of our optimally doped Ar-Annealed sample, which is $NCCO\_0.15\_AA$. The resistivity data has a clear signature of the superconducting transition, with the onset temperature being 17.8 K. This critical temperature is lower than the reported T_c in a single crystal [40], which is due to the grain boundaries and disorder in the polycrystalline samples. Figure 4.1c presents the reported resistivity data on the polycrystalline sample of the same compound, and our data is consistent with their results.

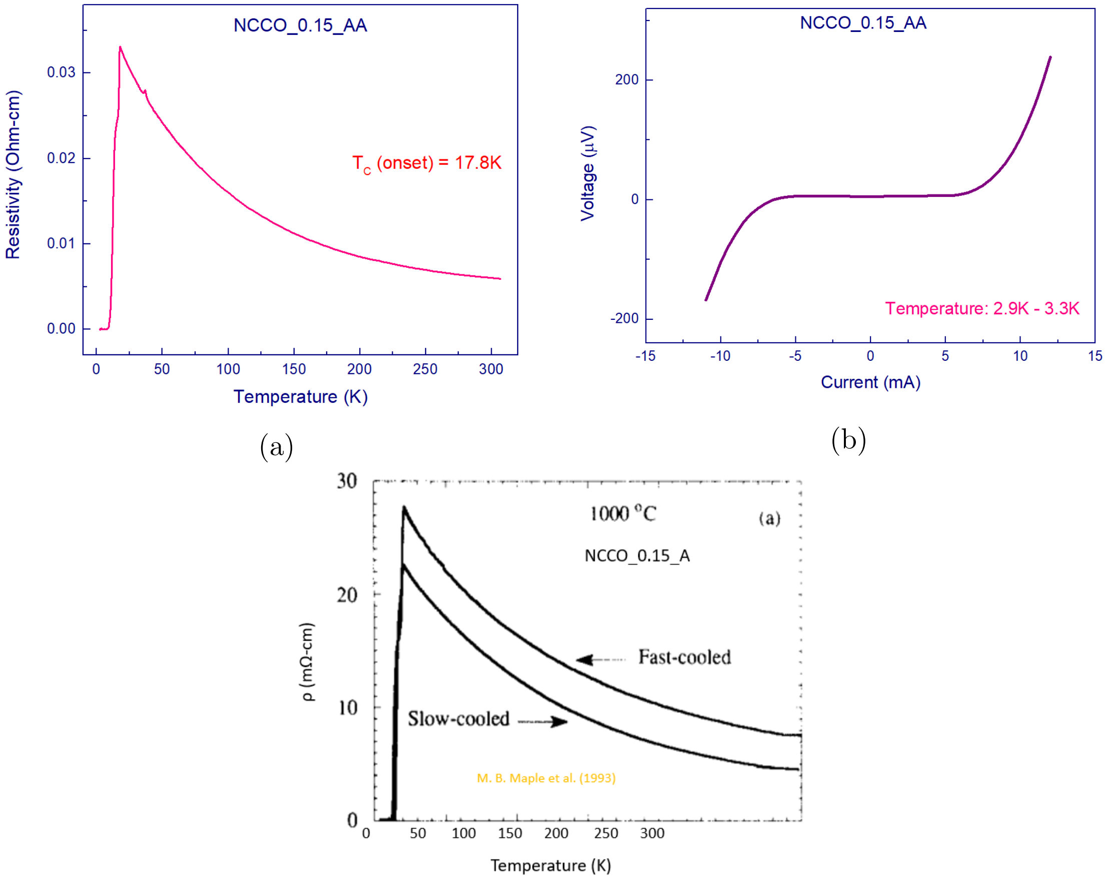

(a)

(b)

(c)

Figure 4.1: (a) The low-temperature resistivity of the optimally doped Ar-Annealed sample showing clear superconducting transition onset at 17.8K. (b) The I-V characteristics of the sample at 3K present a signature of a superconducting state. (c) Reported low-temperature data on the optimally doped polycrystalline sample (Source - [27]).

The I-V characteristics of this sample at 3K have been presented in figure 4.1b. This I-V characteristic shows a clear signature of a superconducting state. For the resistivity measurements, we used 1 mA current to make sure that the sample was in the superconducting state. One thing to be noticed here is that in our polycrystalline samples, the critical currents are not as high as reported for the single crystals [41]. This might be related to the presence of a large number of grain boundaries in the polycrystalline samples. We will discuss the importance of this observation in the later sections.

To present the importance of Ar-annealing to achieve the superconducting state, which has been discussed extensively in literature [38], we measured the low-temperature resistivity of the unannealed sample. This sample shows a superconducting drop below $T_c(\text{onset}) = 6$ K as opposed to 17.8 K for the Ar-Annealed sample.

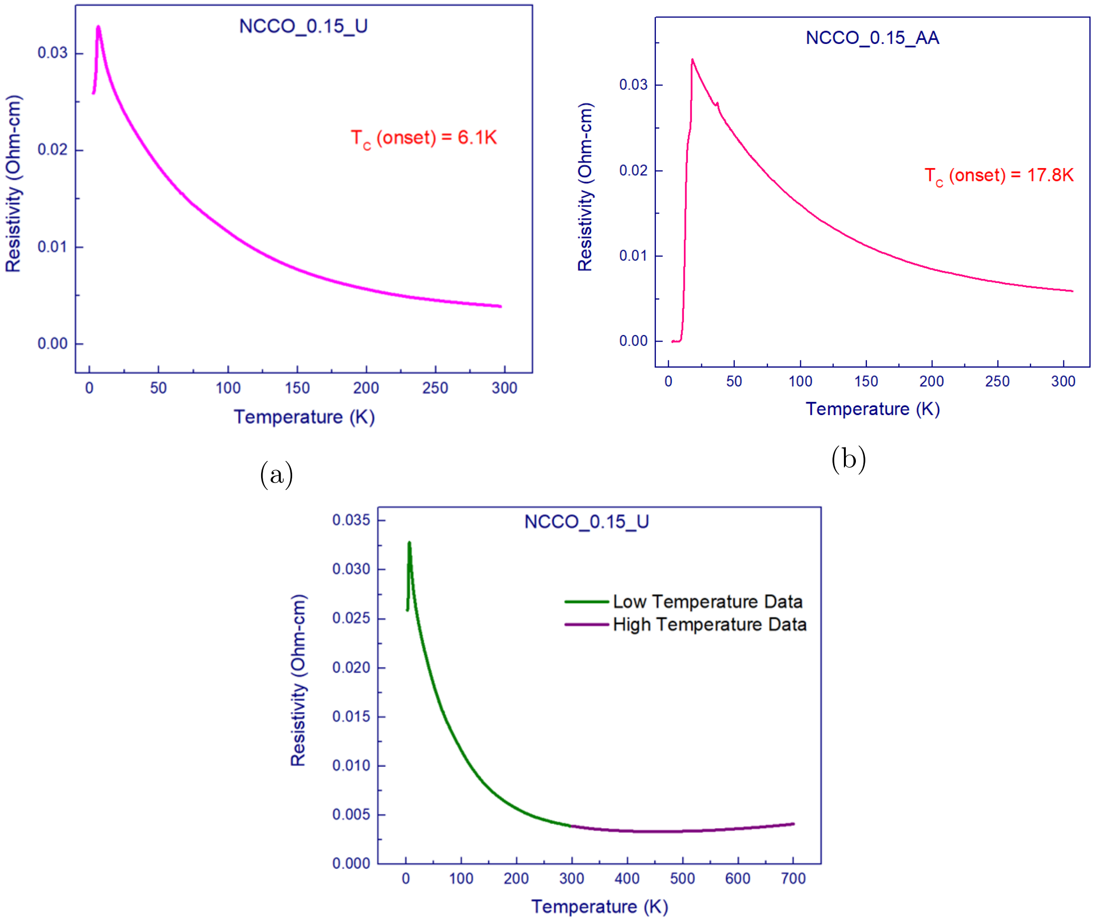

(a)

(b)

(c)

Figure 4.2: (a) The low-temperature resistivity of the optimally doped Unannealed sample. (b) The low-temperature resistivity data of the Ar-Annealed version of the same sample is presented for comparison. (c) The resistivity of the $NCCO\_0.15\_U$ in the temperature range 2K to 700K.

In the unannealed sample, the superconducting transition also remains incomplete down to 3 K (i.e., the resistance remains non-zero down to our lowest measurement temperature). We got a complete superconducting transition in the Ar-Annealed samples. The low-temperature resistivity of these two samples has been presented in the figures 4.2a and 4.2b side by side for comparison. This comparison clearly presents the importance of Ar-annealing in obtaining the superconducting state, which is consistent with the literature. Figure 4.2c presents the resistivity of the $NCCO\_0.15\_U$ sample in the temperature range of 2K to 700K. The high-temperature and low-temperature data nicely match each other. The high-temperature data will be analyzed in depth in the next section.

The critical temperature of the single crystal NCCO has an explicit doping-dependent behavior, which has been discussed in detail in ref. [40]. Even though we are working with polycrystalline samples, we can use that empirical formula (eq. 4.1) given in Ref. [40] to estimate the critical temperature as a function of doping concentration x.

By taking the reported maximum critical temperature $(T_c, max) = 25.\ 1$ K [40], we can back-calculate x for the observed $T_c = 17.8$ K. Using this, we obtained the stoichiometry (x) to be 0.16, which is close to our doping of x = 0.15.

$$\begin{aligned} \frac{T_c}{T_{c,max}} &= 1 - 1320(x - 0.146)^2 \\ x &= 0.146 \pm \sqrt{\frac{1}{1320}\left(1 - \frac{T_c}{T_{c,max}}\right)} \end{aligned} \tag{4.1}$$

The low-temperature resistivity of the $NCCO\_0.17\_AA$ is presented in figure 4.3a. In this sample, the onset of the superconducting transition is at 17.5K. However, the complete transition only occurs upon cooling below 8 K. This kind of behavior can be caused by the inhomogeneous doping of cerium, which is usual in EDC [27]. Even though, in our EDX data, we don't see any inhomogeneous distribution of Cerium, it's quite possible that on a microscopic scale, we have inhomogeneous doping. Figure 4.3b presents the resistivity data measured in different applied magnetic fields. While the resistivity above the superconducting transition has the same behavior for all the samples, the superconducting onset has been suppressed by the applied magnetic field. Analysis of the critical temperature using the empirical relation 4.1 provides that the doping x will be 0.16 if we consider the T_c(onset) and if we consider the transition temperature to be T_c(final) = 8 K, doping will be x = 0.17. These rough estimates are close enough to our intended doping.

Figure 4.4a presents the low-temperature resistivity data of the Ar-Sintered sample with doping x = 0.13. According to the single crystal studies, this sample should have been superconducting. However, in our polycrystalline samples, we did not observe a superconducting transition. Instead, there is a resistivity drop around 10.9 K, followed by an upturn around 5 K. This can be due to the inhomogeneous doping of Cerium, which highly affects

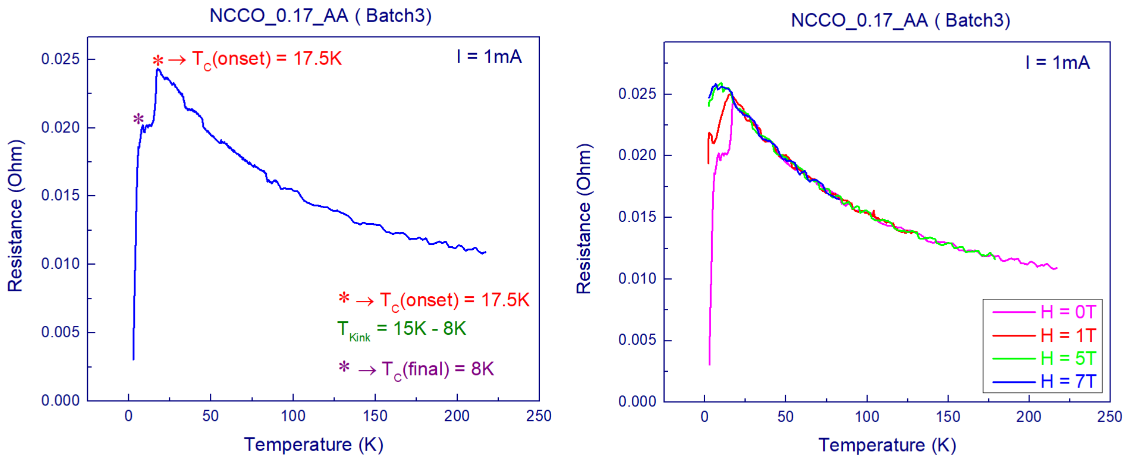

(a) (b)

Figure 4.3: (a) The low temperature resistivity of the x =0.17 doped Ar-Annealed sample. (b) The low-temperature resistivity was measured at different applied magnetic fields.

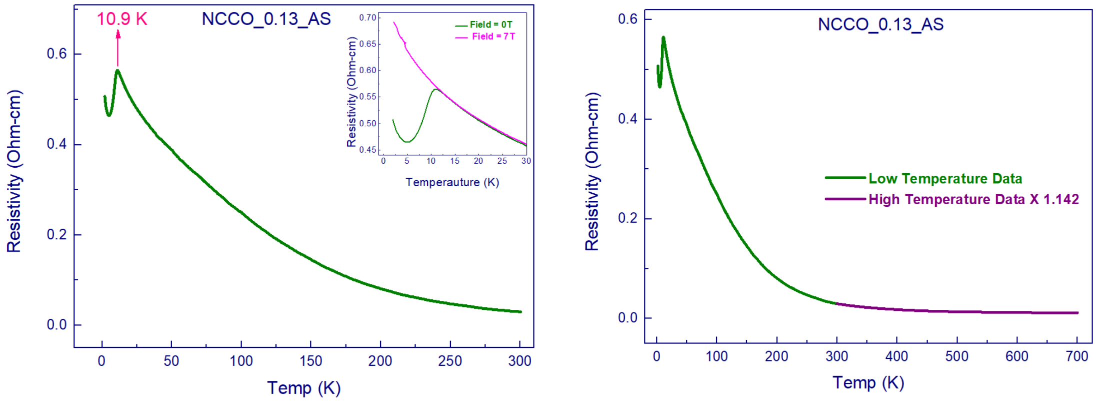

(a) (b)

Figure 4.4: (a) The low temperature resistivity of the x =0.13 doped Ar-Sintered sample. The inset presents the resistivity of the samples at an applied field of 7T. (b) The resistivity of the same sample over the temperature range of 2K - 700K.

the low-temperature behavior of these samples. Resistivity upturn at low temperatures has been reported for the underdoped samples of NCCO due to weak localizations of charge carriers around the Ce ions [42]. In our samples, we might have patches of lower doping leading to this upturn at low temperatures, and the patches with doping close to x = 0.13 or higher exhibit superconducting transitions. This inhomogeneous doping has been a constant challenge in studying the EDC.

In the inset of the figure 4.4a, we present the resistivity of the samples at an applied field of 7T. With the application of a 7 T magnetic field, the transition at 10.9 K is completely suppressed. However, close to the upturn at 5 K, a kink in the resistivity data remains in the applied field of 7 T, which suggests a possible magnetic origin. Figure 4.4b presents the resistivity data of the x = 0.13 sample over the temperature range of 2K to 700K. We had to scale the High-temperature data by a factor of 1.142 to match it to the low-temperature data. This might be due to errors in the geometrical factors. The high-temperature resistivity part will be discussed in detail in the next section.

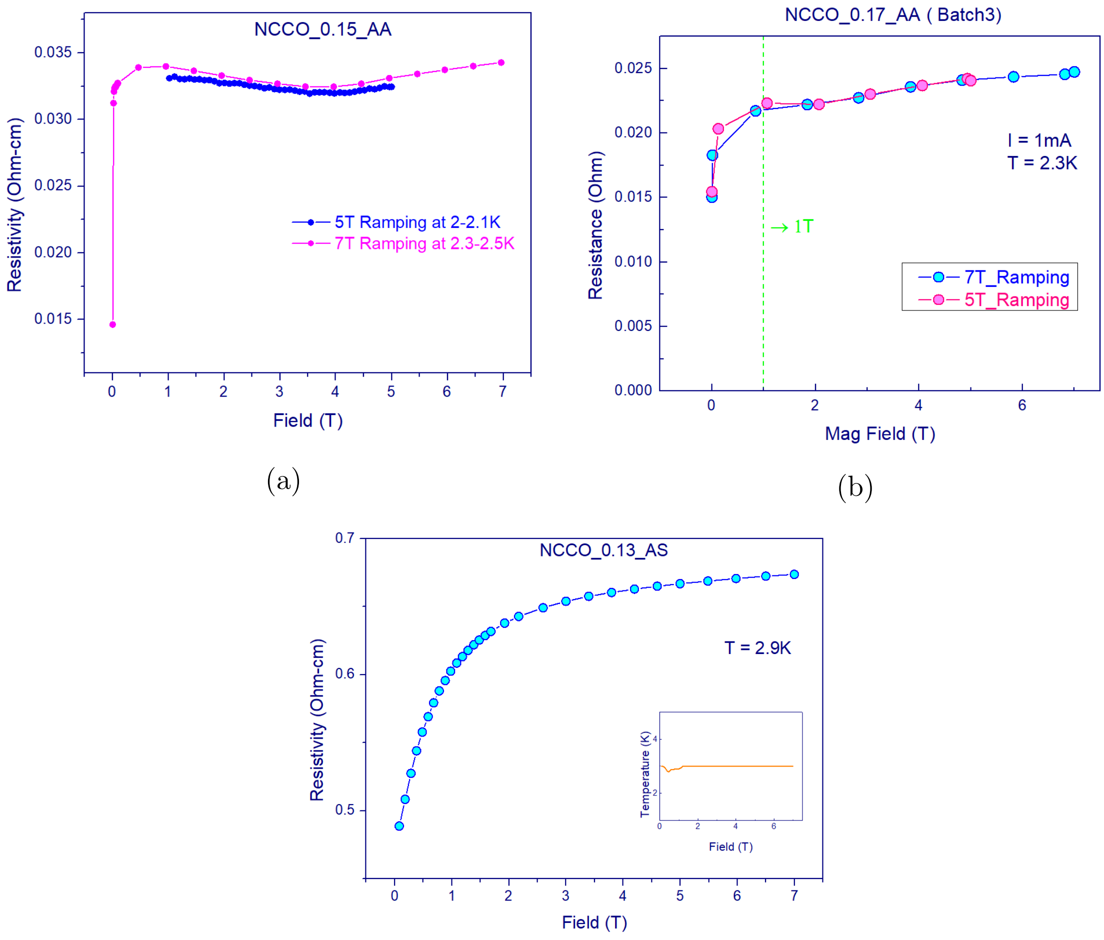

(a)

(b)

(c)

Figure 4.5: Magnetic field dependent resistivity at very low temperature(2-3K) for three different samples, $NCCO\_0.15\_AA$ (a), $NCCO\_0.17\_AA$ (b), $NCCO\_0.13\_AS$ (c).

Figure 4.5a and 4.5b presents the resistivity of $NCCO\_0.15\_AA$ and $NCCO\_0.17\_AA$

sample as a function of the magnetic field at a temperature close to 2.3 K. These measurements are done to assess the normal state of the EDC superconductors inside the superconducting dome. It is interesting to note that, in our polycrystalline samples, the critical magnetic field of around 1 T is much lower than the reported values for the single crystal. We also measured the low-temperature resistivity of the $NCCO\_0.20\_U$ sample, where we don't see any superconducting transitions as this composition does not lie inside the superconducting dome of the Cuprates phase diagram. This result has been presented in figure 4.10 and analyzed in detail in the next section.

To summarise, the low-temperature resistivity of our samples is in good accord with the literature. The Ar-Annealed samples undergo complete superconducting transitions, whereas the transitions remain incomplete for the unannealed samples. Due to possible inhomogeneous doping of cerium and grain boundary contribution in polycrystalline samples, our samples do not show a very sharp transition, which is consistent with the literature. The analysis of the T_c as a function of doping matches our expectations reasonably. The critical current (I_c) and critical magnetic field (H_c) of our polycrystalline samples are lower than those of the single crystals due to the disorders and grain boundaries in the polycrystalline samples. This lower I_c and H_c might help us to study the normal state of the EDC inside the superconducting dome.

4.2 High Temperature Resistivity Behavior

We conducted high-temperature (300 K - 700 K) resistivity measurements on our samples using our home-built high-temperature setup, which allows for the use of various probe contact types. The resistivity obtained in our setup using a gold wire with silver paint contact (GW) or pressure contact with silver paint (PCS) shows a good agreement with the resistivity measured in the commercial Linseis LSR setup. To measure the sample in the LSR setup, we sputter-coated platinum (Pt) pads onto the sample's surface. This was necessary to establish electrical contact between the voltage probes in the LSR set-up and the sample. This step served to validate the quality and reliability of our data. Figure 4.6a displays the sputtered Pt pads on the samples used for measurements in the LSR setup. Figure 4.6b presents the resistivity measured both in the LSR apparatus and in our homebuilt setup, demonstrating a good agreement between the two measurements.

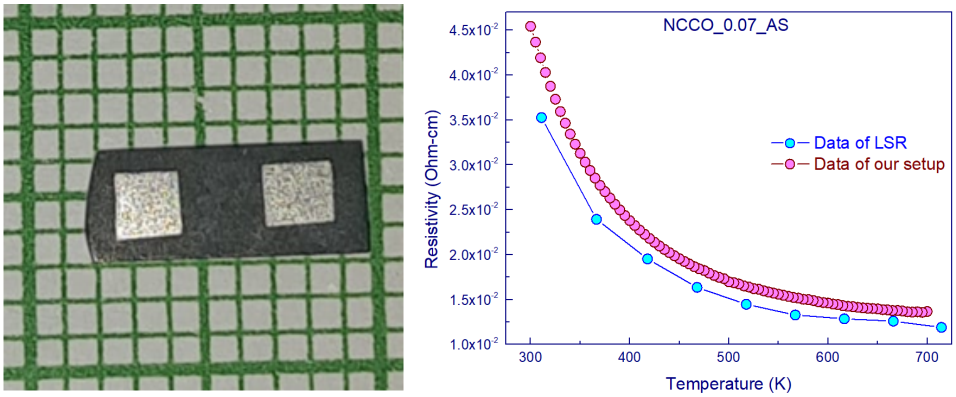

(a)

(b)

Figure 4.6: (a) The Pt sputtered pads on one of the samples, which is used in LSR setup for resistivity and Seebeck measurement. (b) The comparison of resistivity data measured in our home-built setup and in the LSR setup.

We have measured the high-temperature resistivity of our samples over a wide range of doping, underdoped (x=0.07) to overdoped (x=0.20) region in our home-built setup. We have taken multiple resistivity runs to ensure that we have high-quality data. We have observed many interesting features in our high-temperature resistivity. Figure 4.7a presents the high-temperature resistivity of all the unannealed samples from under-doped to over-doped regions.

The resistivity of the unannealed samples initially decreases with increasing temperature, and above around 450 K (roughly), it starts to rise for all the samples except x = 0.20 doped. For the x=0.20 over-doped samples, the resistivity always increases. The reason for this will be discussed in detail in the following section. The initial decreasing trend agrees with the previous reports on polycrystalline samples. We wish to reemphasize that this resistivity-decreasing behavior at low temperatures is present over a wide doping range (0.07-0.20) and does not show the same temperature dependence as the single crystal sample.

The phenomenon of resistivity upturn, characterized by an increase in resistivity with rising temperature, presents an intriguing observation in these unannealed samples. This upturn manifests only above a specific temperature threshold, T^*, beyond which $\frac{d\rho}{dT}$ becomes positive. The temperature T^* is defined as the point at which $\frac{d\rho}{dT}$ changes sign from negative

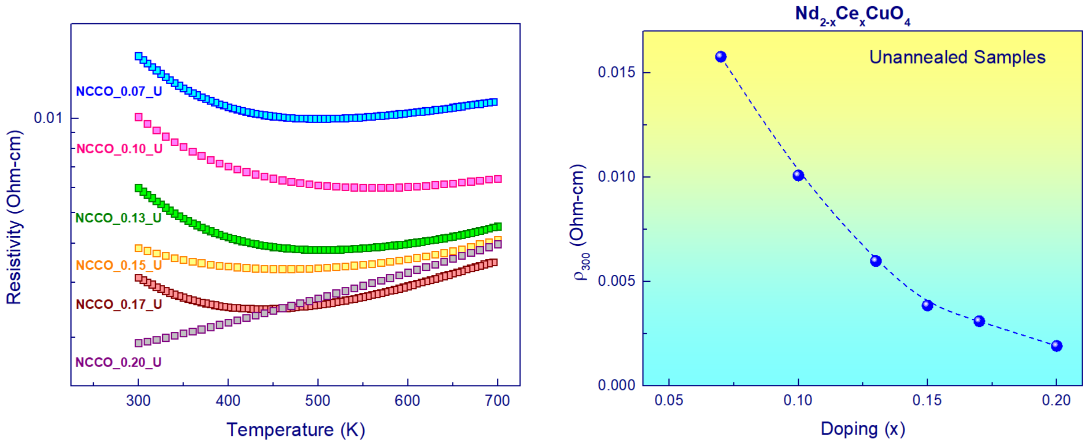

(a) (b)

Figure 4.7: (a) Resistivity of all the samples from Room temperature to 700K has been presented in log scale. For all the samples, except highly over-doped samples(x = 0.20), the resistivity shows an upturn around 450K. (b) The resistivity of the sample at 300K has been presented as a function of the doping, which has an expected decreasing trend.

to positive. So, in the unannealed samples, the resistivity first decreases as the temperature rises, but above T^*, we observe a resistivity upturn.

Figure 4.7b presents the resistivity of all the samples at 300K as a function of the doping. The ρ_{300} (Resistivity at 300 K) is decreasing with the doping. This is exactly what we expect. As we increase cerium doping, we introduce more and more electrons into the system. More carriers imply the conductivity will be higher. However, as the carrier concentration increases, so does the electron-electron interaction, which is crucial for comprehending the behavior of the x = 0.20 sample.

The resistivity upturn around 450 K shifts to a lower temperature (discussed later) with increasing doping and becomes visibly more prominent. The Ar-Annealing believed to be critical for obtaining the superconductivity, shifted this upturn to the higher temperature. Figure 4.8 presents the resistivity of the x = 0.10 doped sample before and after the Ar-annealing. In the unannealed sample, the resistivity upturn is around 550 K. However, it shifted to 650 K in the Ar-Annealed sample. This shifting in the onset of the resistivity upturn has not been reported before to the best of our knowledge.

There are literature studies that suggest that the Ar-annealing reduces the oxygen

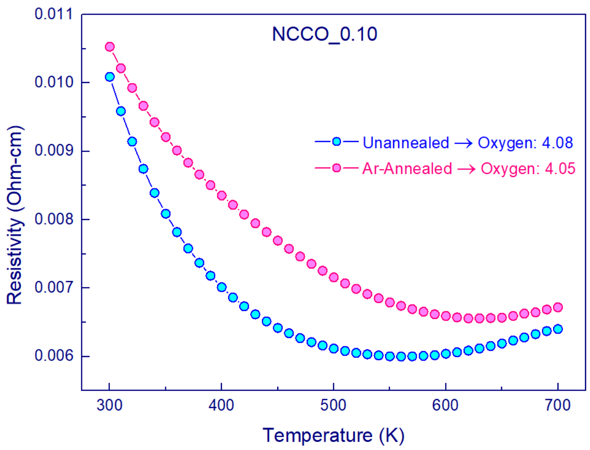

(a)

Figure 4.8: Resistivity of the sample $NCCO\_0.10$ before (Unannealed) and after (Ar-Annealed) the Ar-annealing is presented in this figure. Clearly, the resistivity upturn got shifted to a higher temperature in the Ar-Annealed sample.

stoichiometry in the sample by 1-2%, and it migrates the oxygen to the apical position over the Cu atom. This Ar-annealing is characteristically different than the normal annealing in air. In the air annealing process, the oxygen stoichiometry is expected to remain unchanged as long as the temperature is not too high above the room temperature. The air annealing may, however, reduce the sample inhomogeneity, strain, and disorder. On the other hand, during the Ar-annealing process, we alter both the oxygen stoichiometry and the position of oxygen within the lattice, potentially impacting the microstructure.

The suppression of resistivity upturn to higher temperatures by Ar-annealing may stem from two primary factors. Firstly, Ar-annealing modifies the microstructure of the sample, leading to an increase in grain boundaries. Secondly, it also impacts the oxygen stoichiometry within the sample. Usually, we keep the as-grown pellet (indexed as unannealed) directly in the tube furnace for Ar-annealing. To increase the grain boundary effects in the sample, we ground these pellets followed by cold-pressing and then kept them for Ar-annealing, referred to as an Ar-Sintered sample.

As a result, these Ar-Sintered samples will show more grain boundaries than just Ar-Annealed samples. The Ar-annealing temperature (1050 K) is also 50 K less than the sintering temperature of 1100 K. Heat treatment at higher temperatures helps us to get grains of bigger size. So, we have more grain boundaries in these Ar-Sintered samples. We kept the Ar-annealing time the same for both processes (Ar-Annealing, Ar-Sintering); hence, we expect the oxygen stoichiometry to be the same for both of these cases. This understanding was confirmed through TGA analysis conducted in an $Ar - H_2$ environment for both samples.

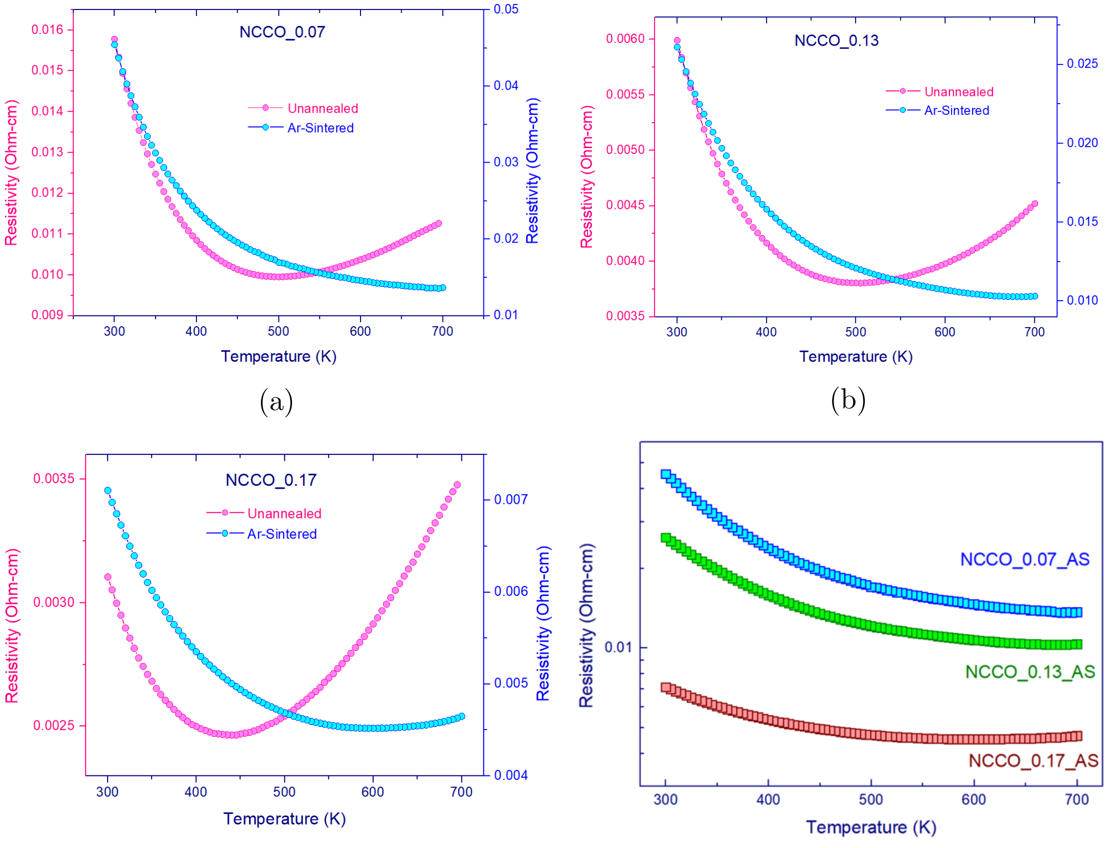

(a) (b)

(c) (d)

Figure 4.9: Resistivity of the Unannealed (pink data points) and Ar-Sintered (Blue data points) samples for the x = 0.07 (a), 0.13 (b), and 0.17 (c) doping. The resistivity upturn around 450K in the unannealed samples has been shifted to a higher temperature in the Ar-Sintered sample. (d) The resistivity of all the Ar-Sintered samples is presented in this figure.

If the oxygen stoichiometry is the critical factor, we would expect no alterations in the shift of the resistivity upturn behavior. Conversely, if grain boundaries significantly influence this behavior, a noticeable shift in the resistivity upturn is expected in the Ar-Sintered sample. Figure 4.9a, 4.9b, and 4.9c presents the resistivity of the samples with doping x = 0.07, 0.13, and 0.17 before (unannealed) and after this conditioning through intermediate grinding (Ar-Sintered). We could suppress the resistivity upturn completely within our measured temperature range in the Ar-Sintered sample. Also, the resistivity value of the Ar-Sintered samples is roughly one order of magnitude higher than the unannealed samples. More grain boundaries, as in the Ar-sintered sample, imply higher grain boundary scattering, which should result in a higher resistivity value. This implies that the increased grain boundary distributions in the Ar-Sintered sample led to a higher resistivity and suppression of this resistivity upturn.

Numerous reports have indicated that the resistivity behavior of the EDC at temperatures exceeding T_c is inconsistent across different samples. The microstructure of these samples, heavily influenced by their growth conditions, can vary significantly. This indicates that the behavior of EDC within these temperature ranges is largely determined by the sample's microstructure. Without understanding the influences of these microstructures, the intrinsic characteristics of the sample remain obscured.

The increase in the grain boundary density leads to higher resistivity, which in turn suppresses the resistivity upturn within our measured temperature range. In subsequent sections, these observations will be further analyzed to quantify the relevant energy scales or crossover temperatures.

The resistivity of all the Ar-Sintered samples has been presented in the figure 4.9d. In the sample with doping x = 0.07, x = 0.13, we completely suppressed the resistivity upturn. In the sample with x = 0.17, the resistivity upturn got shifted to a higher temperature by 250 K. In the x = 0.17 sample, due to the higher number of carriers, we still observed the upturn.

Now, we will discuss the results of the $NCCO\_0.20\_U$ sample, an unannealed sample of the highest doping for this project. This sample has the highest carrier density. The higher number of carriers means the grain boundary effects will be less significant. Figure 4.7b shows that this sample has the lowest resistivity at 300 K. The high-temperature resistivity of the x = 0.20 sample, presented in figure 4.7a, is different from all the samples as it is increasing in nature in the temperature region 300 K - 700 K. We measured the low-temperature resistivity of this sample to verify that at low temperature, it does show a minimum, below which the resistivity increases upon cooling. See Fig. 4.10, where the resistivity upturn has been suppressed to as low as 200 K. Thus, another piece of evidence we have discussed is that with an increase in carrier concentration, the resistivity upturn shifts to progressively lower temperatures.

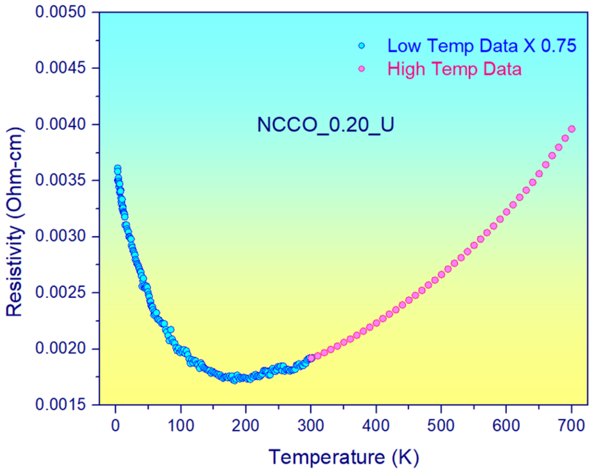

Figure 4.10: The resistivity data of the sample $NCCO\_0.20\_U$ from 2 K to 700 K. The low-temperature data was scaled with a factor of 0.75 to match the high-temperature data. As we are using the gold wire and silver paint contact to measure the resistivity, the inter-probe distance measurement is not always perfect, resulting in the observed mismatch.

We can thus conjecture that as we increase the temperature, carriers gain thermal energy, thus overcoming the grain boundary effects. We get to see the resistivity upturn. The exact temperature for this crossover from the initial decreasing resistivity trend to the increasing trend depends on the grain boundary distribution and the carrier concentration. By conditioning our sample, we can manipulate the grain boundary and, as a result, suppress the resistivity upturn in some lower-doped samples.

Resistivity Upturn Temperature, T*

Figure 4.11a illustrates the onset temperature (T^*) for the resistivity upturn as a function of Ce doping. With increasing Cerium doping, the onset temperature decreases. However, it's important to note that this onset temperature (T^*) is influenced by the sample synthesis process. For instance, the $x = 0.20$ sample, sintered at 1150K, exhibits a notably lower onset temperature compared to other samples. Similarly, sintering the $x = 0.17$

sample at the same temperature for the same duration (Pink data points, Sample of Batch 3b) resulted in a significant reduction in the onset temperature compared to the sample sintered at 1100K (Blue data point, Sample of Batch1). This implies that higher sintering temperatures lead to reduced grain boundary contributions, thereby revealing the intrinsic characteristics of EDC at lower temperatures.

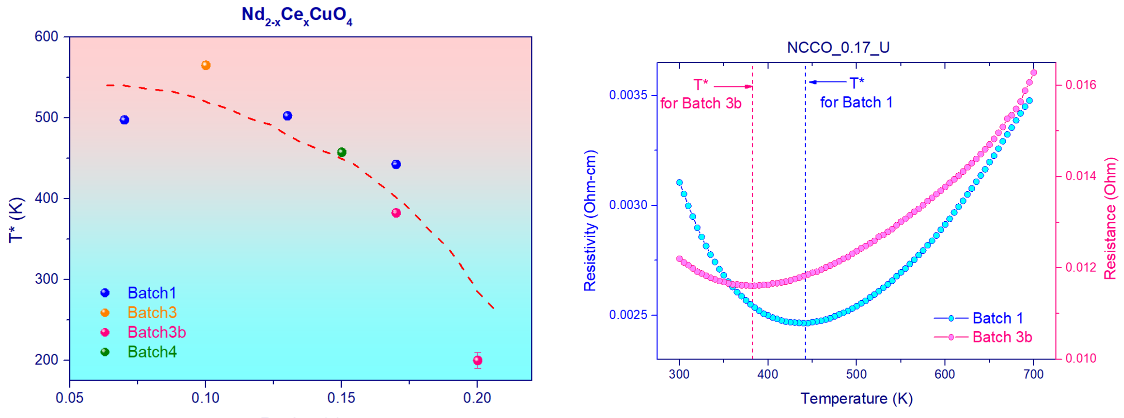

(a)

(b)

Figure 4.11: (a)The onset temperature of resistivity upturn, T* for different Ce doping. (b) The resistivity of the $NCCO\_0.17\_U$ sample sintered at two different temperatures, leading to two different T* for the resistivity upturn.

4.3 Resistivity Analysis

In this section, we will analyze our high-temperature resistivity data with theoretical models to gain a better understanding of the resistivity behavior and its physical significance. In the previous section, we discussed that the resistivity characteristics are dependent on the sample's conditioning. This dependency has been attributed to the grain boundaries in the sample. So, to understand the resistivity behavior of our sample, we will follow Matthiessen's Rule. Matthiessen's Rule states that the total scattering time (τ_{total}) can be considered as the inverse of the sum of the inverse of individual scattering times (τ_i) due to different mechanisms that do not influence each other.

$$\frac{1}{\tau_{total}} = \sum_i \frac{1}{\tau_i} \tag{4.2}$$

In this context, we can deconstruct our observation into two different mechanisms. One is related to the intrinsic behavior of our sample, and the other is related to the grain boundary scattering. Following Matthiessen's Rule, we can write the total scattering time as the contribution coming from the grain boundary and the intrinsic scattering of the samples.

$$\frac{1}{\tau_{total}} = \frac{1}{\tau_{in}} + \frac{1}{\tau_g} \tag{4.3}$$

Where τ_{in} corresponds to the inherent scattering time scales in the system and τ_g refers to the time associated with the grain boundary effects. The resistivity is related to the scattering time scale by Drude's formula.

$$\rho = \frac{m}{ne^2\tau} \tag{4.4}$$

In this equation, m corresponds to the mass of the charge carriers in the sample, n is the carrier concentration, e is the charge of the carriers, and τ refers to the scattering time. If we combine Drude's formula with Matthiessen's Rule, we can clearly write that the total resistivity is the sum of several different components, each representing a distinct scattering mechanism. For our analysis, the total resistivity can be written as the sum of the inherent characteristics and the resistivity associated with the grain boundary.

$$\rho = \rho_{in} + \rho_g \tag{4.5}$$

The resistivity due to grain boundaries will mask the inherent resistivity behavior of the sample if it is not dominant. So, depending on the relative strengths of the two scattering mechanisms, we will observe different resistivity behaviors. In our samples, we have observed different resistivity trends depending on the sample's conditioning, which is consistent with our understanding.

The grain boundary scattering usually shows a decreasing resistivity trend with increasing temperature. The reported studies of the single crystals of EDC suggest that the intrinsic resistivity increases with temperature. So, the resistivity upturn observed in the unannealed samples seemed to be due to the inherent increasing resistivity behavior (specifically, T^2) of the EDC. With increasing temperature, the contributions coming from the grain boundary are decreased and get back the intrinsic behavior of the EDC once the grain boundary contributions become negligible to the intrinsic behavior.

We would like to model the grain boundary contributions so that we can understand and correlate the intrinsic behavior with the reported results on single crystals. We have used the Arrhenius equation to fit the decreasing resistivity trend and model the behavior of the grain boundary scattering. The Arrhenius model corresponds to the systems having an energy cost for a specific process to occur and has been used regularly to model the behavior of semiconductors. The Arrhenius equation for resistivity has been mentioned below.

$$\rho = \rho_0 \exp(\frac{\Delta}{k_B T}) \tag{4.6}$$

Where ρ_0 corresponds to the residual resistivity and Δ refers to the activation energy. The Arrhenius equation can also be used as a model for grain boundary[43]. At the grain boundary, there are small crystallites oriented in different directions, which implies a discontinuity in the electronic band structure, creating a potential barrier that charge carriers must overcome to move from one grain to another. Charge carriers can cross this barrier by gaining enough thermal energy at high temperatures. This scenario is exactly similar to that of the Arrhenius equation, where the system has to provide the activation energy for a specific process to occur.

To implement the Arrhenius model, we present the equation in a different way so that we can use linear fit. The Equation 4.7 has been used for the linear fitting. By plotting $\ln(\rho)$ as a function of $\frac{1}{T}$, with the help of this equation, we can estimate the Activation energy. The evaluation of activation energy with the sample conditioning will help us to establish the correlation between the observed resistivity trend and the sample's grain boundary structure.

$$\ln(\rho) = \ln(\rho_0) + \frac{\Delta}{k_B T} = c + \frac{d}{T} \tag{4.7}$$

The Ar-Sintered sample, in which we don't have any resistivity upturn, and we only see the decreasing resistivity trend, has been fitted with the Arrhenius model. Figure 4.12 presents the linear fit of $\ln(\rho)$ as a function of $\frac{1}{T}$ for the x = 0.13 doped sample.

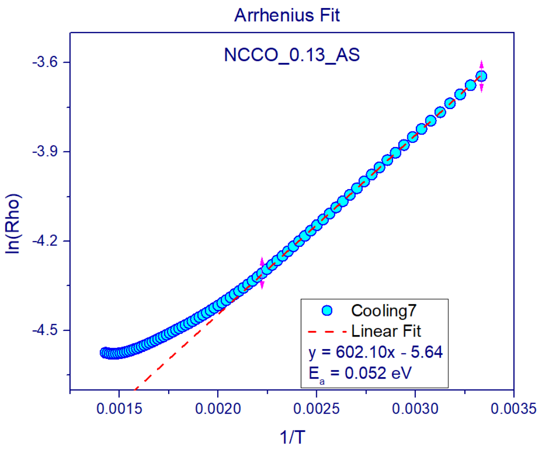

(a)

Figure 4.12: Arrhenius fit for the resistivity of the sample $NCCO\_0.13\_AS$.

Figure 4.13a and 4.13b present a similar Arrhenius fitting for the other two Ar-Sintered samples. For all of these samples, this Arrhenius model yields a good quality fit.

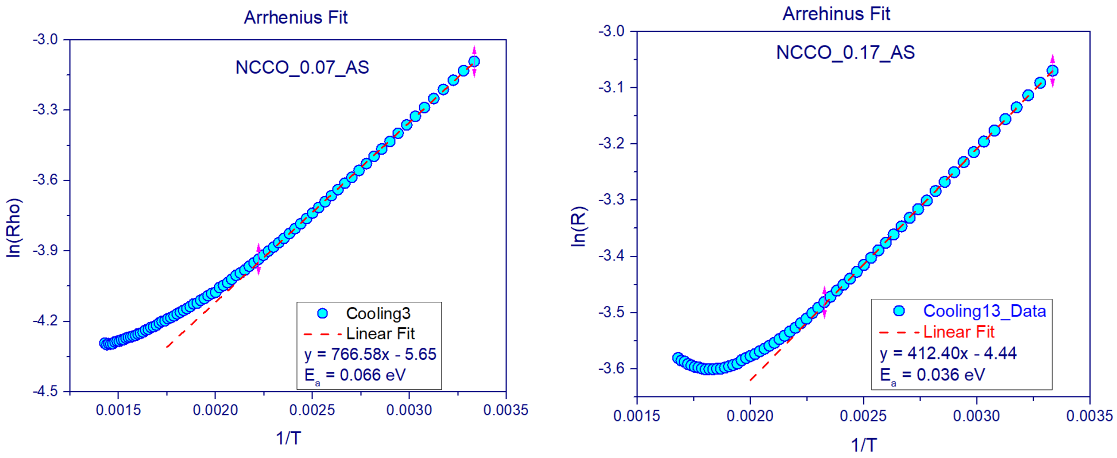

(a)

(b)

Figure 4.13: (a) Arrhenius fitting for the sample $NCCO\_0.07\_AS$. (b) Arrhenius fitting for the sample $NCCO\_0.17\_AS$.

A similar analysis has been done for the unannealed samples to capture the grain boundary effect below the resistivity crossover temperature. For the unannealed samples, the initial decreasing trend of resistivity is fitted with the Arrhenius model. Then, we subtracted this from the raw resistivity data. This subtracted data has been analyzed further to understand the inherent behavior of EDC.

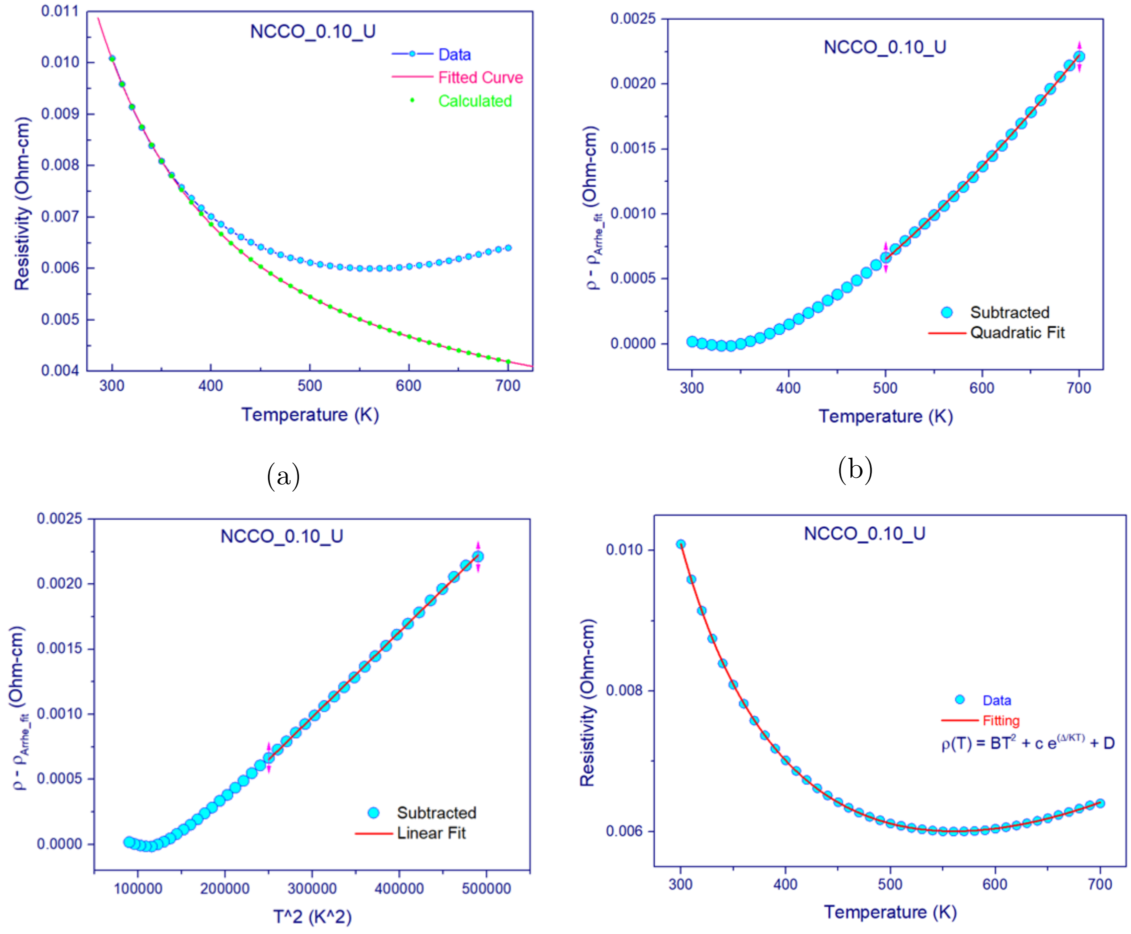

(a) (b)

(c) (d)

Figure 4.14: (a) Arrhenius fit to the decreasing resistivity trend for the unannealed samples with doping x = 0.10. (b) The raw data after the subtraction of the Arrhenius fit gave a good quadratic fit. (c) The same subtracted data has been plotted as a function of T^2 for better visualization of quadratic temperature dependency. (d) The combined function of grain boundary effect and quadratic behavior captures the complete resistivity behavior of the sample.

Figure 4.14a presents the Arrhenius fitting for the x = 0.10 doped sample. The decreasing resistivity trend has been captured in our fitting. Figure 4.14b presents the subtracted data after the Arrhenius fitting. We have tried different temperature dependencies to analyze the subtracted data. The Quadratic fit ($\rho - \rho_{arrhe\_fit} = BT^2 + D$) has worked satisfactorily. This analysis suggests that the resistivity behavior, after subtracting the Arrhenius component due to the grain boundary contribution, corresponds to quadratic temperature dependence. We have also plotted the subtracted data as a function of T^2 (Figure - 4.14c), which produces a clear linear fit, suggesting a generic quadratic temperature dependency.

This quadratic temperature dependence has been reported for many single crystals of the EDC. Our analysis suggests that this quadratic behavior is also present in the polycrystalline samples. However, it has been masked by the contribution from the grain boundaries. Now, if we combine the functional form of Grain boundary contribution and the inherent characteristic of EDC, we get a combined function (Equation 4.8), which can capture the overall resistivity trend.

$$\rho = BT^2 + c\exp(\frac{\Delta}{k_B T}) + D \tag{4.8}$$

Figure 4.14d presents the fitting of this combined equation to the raw data of the unannealed sample with x = 0.10, and we have got a quality of fitting parameter (χ^2) greater than 0.9999.

With this combined function, we could capture the complete resistivity trend. However, as this combined function has four independent variables, we have to be careful while implementing it. Otherwise, the parameter will take unphysical values and produce a good fit. For example, from our understanding of the model, we know that the energy gap and the coefficient B can't be negative, and D should be very small. Using this functional form without considering physical implications may produce a good quality fit, but that will not assist us in understanding the actual scattering mechanism. Hence, we analyzed the resistivity of all the unannealed samples by first fitting the low-temperature decreasing resistivity trend to the Arrhenius equation, followed by the T^2 analysis of the subtracted data.

Figure 4.15a and 4.15b presents a similar analysis for the unannealed sample x = 0.13. We find a reasonably good quadratic fit after subtracting the grain boundary contribution from the as-measured resistivity data.

A similar analysis for the resistivity data for the unannealed samples x =0.15, 0.17, 0.20 has been presented in figure 4.16. The subtracted data shows a quadratic temperature dependency for all the samples. This analysis supports that in these samples, we have T^2 dependence. But it is masked under the contribution coming from the grain boundary. Once the carrier can overcome the grain boundary effect at higher temperatures, we get to see their

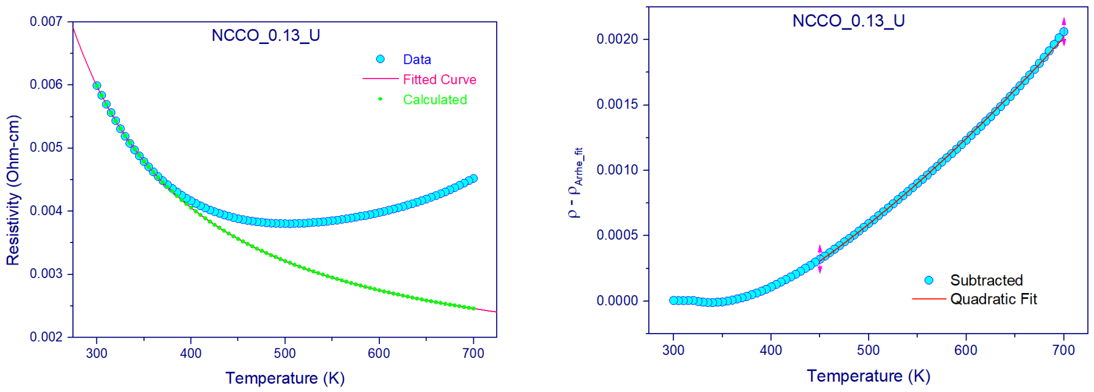

(a) (b)

Figure 4.15: (a) Arrhenius fit the decreasing resistivity trend for the unannealed samples with doping x = 0.13. (b) The subtracted data gave a good quadratic fit with a goodness of fit greater than 0.9999.

inherent characteristics. Depending on the sample conditioning and the doping coefficient, the required temperature will vary. In the x = 0.20 doped sample ($NCCO\_0.20\_U$), we see the onset of the quadratic temperature dependence even from the temperature lower than the room temperature.

For the $NCCO\_0.20\_U$, the Arrhenius model only produces a good fit of up to 50 K. The Arrhenius model, which is used to model the grain boundary (GB) scattering in this work, will work well if the excitation associated with GB scattering is only due to the activation energy gained through the temperature. As we go to very low temperatures, the quantum mechanical processes, such as tunneling through the grain boundary barrier, will also play a significant role. So, at lower temperatures, this simple fitting protocol, which only accounts for thermal activations, could not capture the complete behavior of the resistivity.

Figure 4.17 presents the activation energy of the Arrhenius model as a function of doping for two sets of samples. The blue data points present the activation energy for the unannealed samples. The overall activation energy has a decreasing trend with doping. As Ce doping increases, the grain boundary also accommodates carriers, leading to a reduced energy gap. Additionally, With higher carrier concentration, a significant number of carriers can be excited through the grain boundary at lower temperatures. Therefore, as the concentration of Ce increases, the activation energy decreases.

The pink data points correspond to the activation energy for the Ar-Sintered sam-

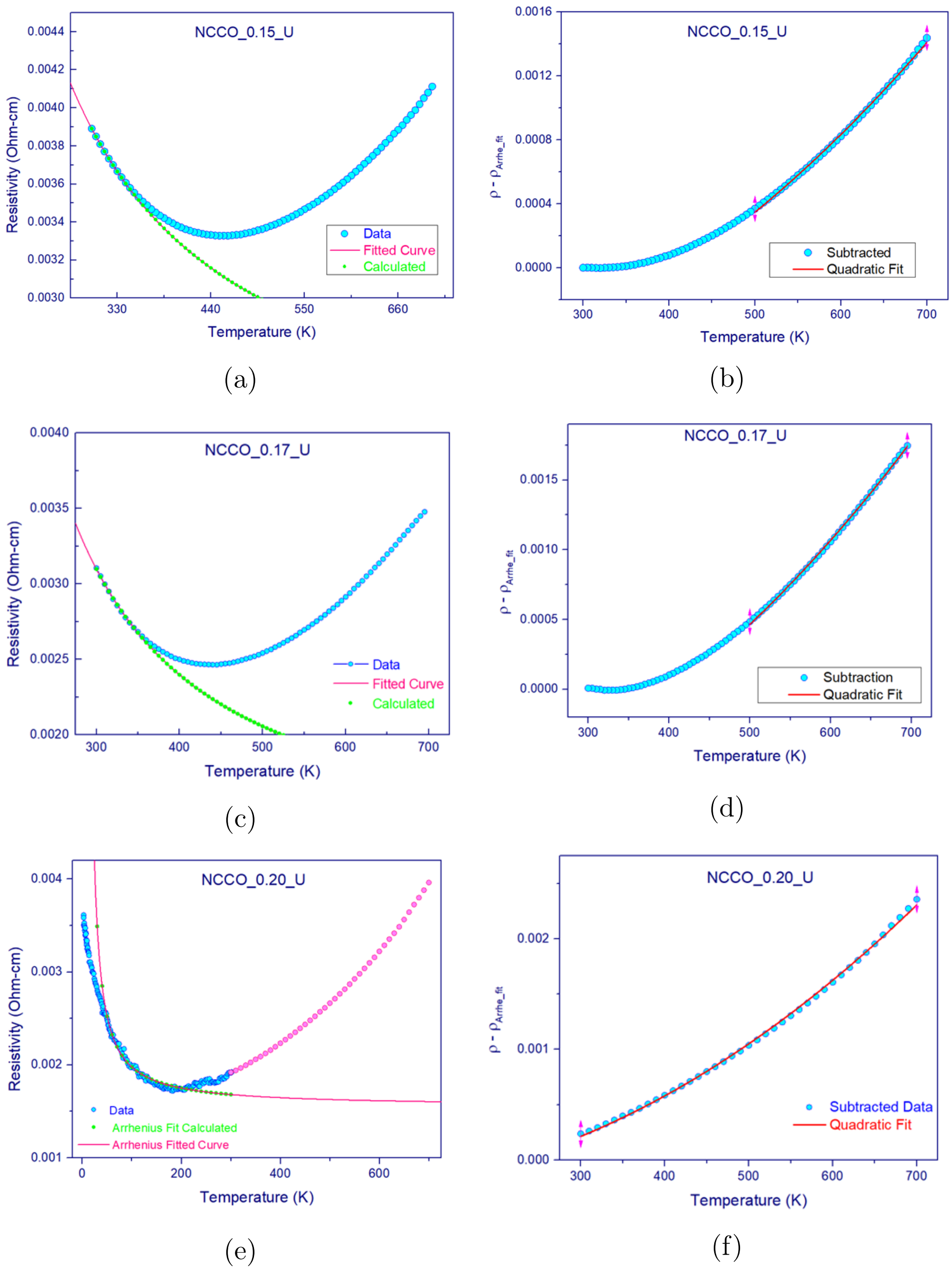

(a) (b)

(c) (d)

(e) (f)

Figure 4.16: (a), (c), (e) presents Arrhenius fit to the decreasing resistivity trend for the unannealed samples with doping x = 0.15, 0.17, and 0.20. (b), (d), (f) shows that the subtracted data has reasonably good T^2 fitting for the doping x=0.15, 0.17, and 0.20.

ples. For these samples also a decreasing trend is observed. In the Ar-Sintered sample, the conditioning increases the grain boundary density, resulting in higher activation energy and maintaining the decreasing resistivity trend at higher temperatures.

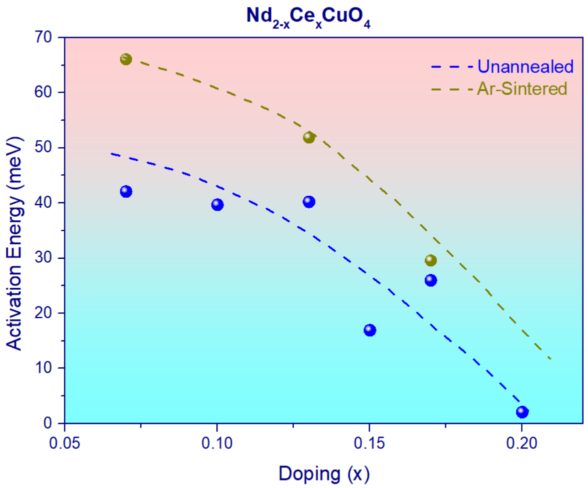

(a)

Figure 4.17: Activation Energy, calculated from the Arrhenius fit for all the samples, has been presented here.

In our polycrystalline samples, we observed a decreasing resistivity trend with increasing temperature, which matches previous reports on the polycrystalline samples. At higher temperatures, we observed a resistivity upturn. We modeled the initial decreasing resistivity trend with the Arrhenius formalism as a consequence of grain boundary scattering. After subtracting this grain boundary contribution, we got to observe the T^2 resistivity behavior over a doping range close to the superconducting dome. This T^2 behavior has been reported on single crystals of EDC. Our analysis suggests that this T^2 characteristic is always present in the EDC samples with doping concentration falling in the region of the superconducting dome. In the following sections, we will discuss the manipulation of grain boundaries in the samples using Hot-Press techniques. That will further support our analysis.

4.4 Grain Boundary Analysis

This section will discuss the grain boundary distributions in our samples. The discussion will focus on grain boundary manipulation through the Hot Press technique and FESEM imaging of those samples.

4.4.1 Hot Pressing

Hot Press can be used methodically to create different microstructures. Here, we have performed hot pressing on our samples at 800 °C for 10 minutes under a pressure of 57 MPa pressure. As the hot pressing is done in a vacuum, we did not go to higher temperatures.

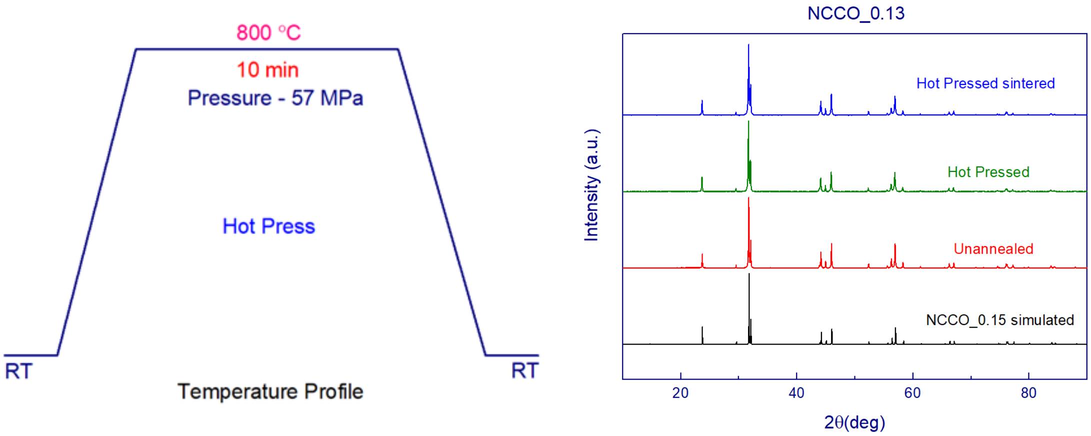

(a)

(b)

Figure 4.18: (a) The condition for the hot pressing. (b) The XRD of the samples after hot pressing and followed sintering corresponds to the pure sample quality.

Figure 4.18b presents the XRD of the samples after the hot pressing. The hot-pressed samples are found to be phase pure, with no signs of any secondary phase forming alongside the main phase. We studied these samples further to understand the role of the grain boundary. Since the hot-pressing duration is typically a few minutes, the grain growth is inhibited in this process, leading to a sample with a higher grain boundary density than what one achieves by a conventional sintering process, which typically lasts for significantly longer durations. Further, in the present case, since the sintering temperature of 800 C is also relatively low, the grain growth is further suppressed.

Figure 4.19a presents the resistivity trend of the sample with doping x = 0.13 for different conditions. As discussed above, the unannealed sample has a resistivity upturn around 450 K. In the Ar-Sintered sample, the upturn has been suppressed to higher temperatures due to an increase in the grain boundary contributions. However, the behavior of the Ar-Sintered sample is somewhat saturating, close to 700 K. The resistivity of the hot-pressed sample (Brown data points) is higher than that of all other samples. The trend

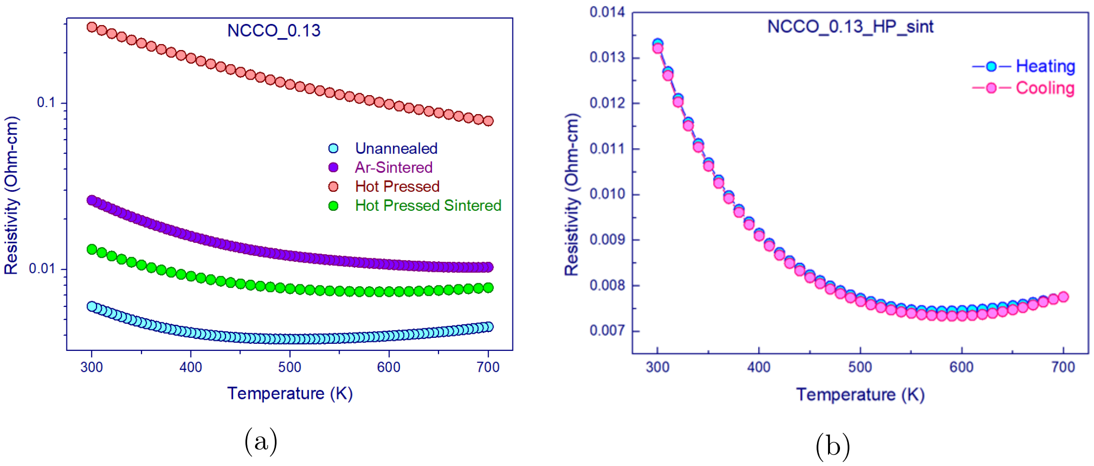

(a) (b)

Figure 4.19: (a) The resistivity trend of the sample with doping x = 0.13 for different conditioning- Unannealed, Ar-Sintered, Hot Pressed, and Hot Pressed Sintered. (b) The resistivity data for the Hot pressed sintered sample exhibits a resistivity upturn of around 600 K.

is also strictly decreasing, suggesting an increase in the grain boundary contribution.

To further test the validity of our analysis, we sintered the hot-pressed pellet under a similar condition as that of the second sintering (figure - 3.1b). This is expected to promote the grain growth. Figure 4.19b presents the resistivity data of the hot-pressed pellets sample post-conventional sintering. After sintering, the resistivity reduced significantly, and we also got back the resistivity upturn. However, the upturn appears around 600 K compared to the 450 K upturn in the unannealed sample. This is in line with our expectations stated earlier.

The resistivity of the hot-pressed sintered sample is slightly higher than that of the unannealed sample, resulting in a shift of the crossover temperature, T*, to 600K. This difference can be attributed to a slightly higher grain distribution in the hot-pressed-sintered sample due to the lower pressure applied during hot pressing (6 tons compared to 10 tons in the KBr Press used for synthesizing the unannealed sample). The electron microscopy images of these samples, which will be discussed next, will support these observations.

We therefore conclude that in the polycrystalline samples of EDC, the resistivity behavior is highly dependent on the grain boundary or the microstructure. However, the series of experiments undertaken during the course of this thesis clearly suggest that the intrinsic T^2 behavior can be revealed by subtracting the grain-boundary contribution, which can be modeled using the Arrhenius-type activation behavior.

4.4.2 Electron Microscopy

In this section, we will discuss the electron microscopy images of our samples to show how the grain size and the grain boundary distributions change upon Ar-annealing, Ar-sintering, and hot-pressing.

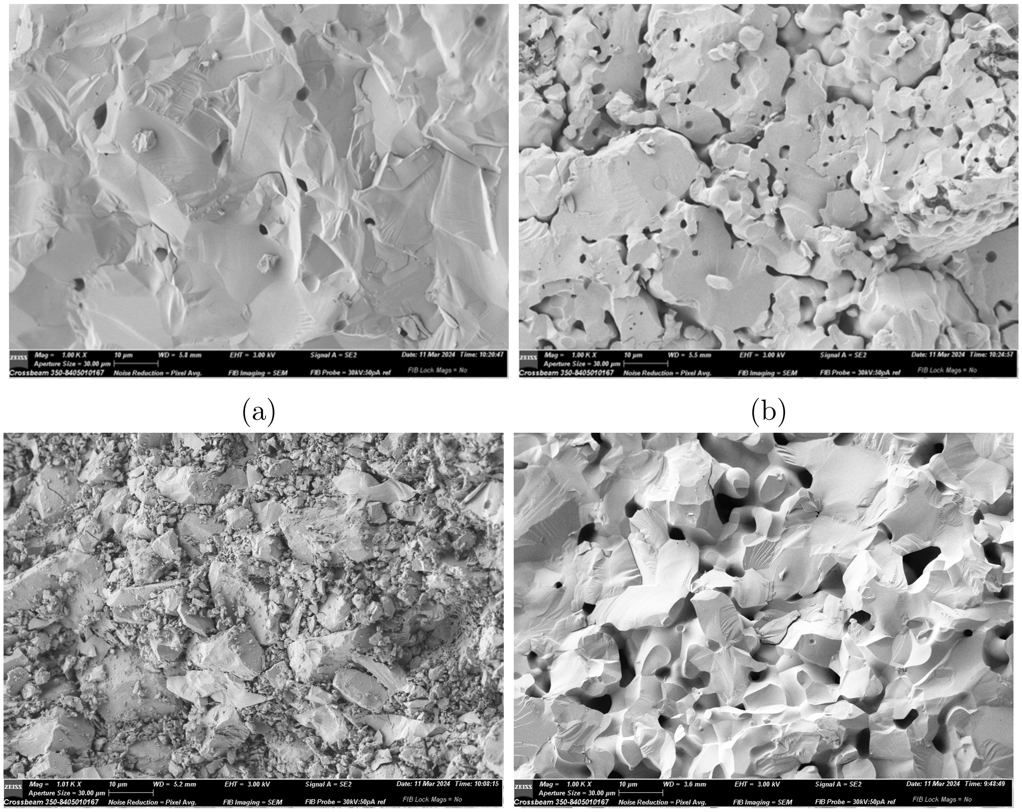

(a) (b) (c) (d)

Figure 4.20: SEM images of $NCCO$_0.13 samples prepared with different conditioning. (a) Unannealed sample. (b)Ar-Sintered sample. (c) Hot Pressed sample. (d) Hot Press sintered sample. The grain boundaries have changed significantly with these conditions, and the observed resistivity trend exactly corresponds to that behavior.

The above figure presents the Electron microscopy images of $NCCO$_0.13 samples collected using SE detector. The Unannealed sample has fewer grain boundaries (figure 4.20a), which results in the lowest resistivity among all these samples. In this sample, we observed the resistivity upturn, which corresponds to the inherent T^2 behavior of EDC. The Hot pressed sample (4.20c) shows the highest grain boundary density, leading to the highest resistivity, and we just observe the contribution of grain boundary on its resistivity behavior.

Upon sintering the hot-pressed pellet (figure 4.20d), the grain boundary density decreases, and its resistivity accordingly decreases. The SEM images closely support our resistivity trend and its analysis, suggesting in these EDCs the contribution coming from the grain boundaries can suppress the intrinsic resistivity behavior of the sample.

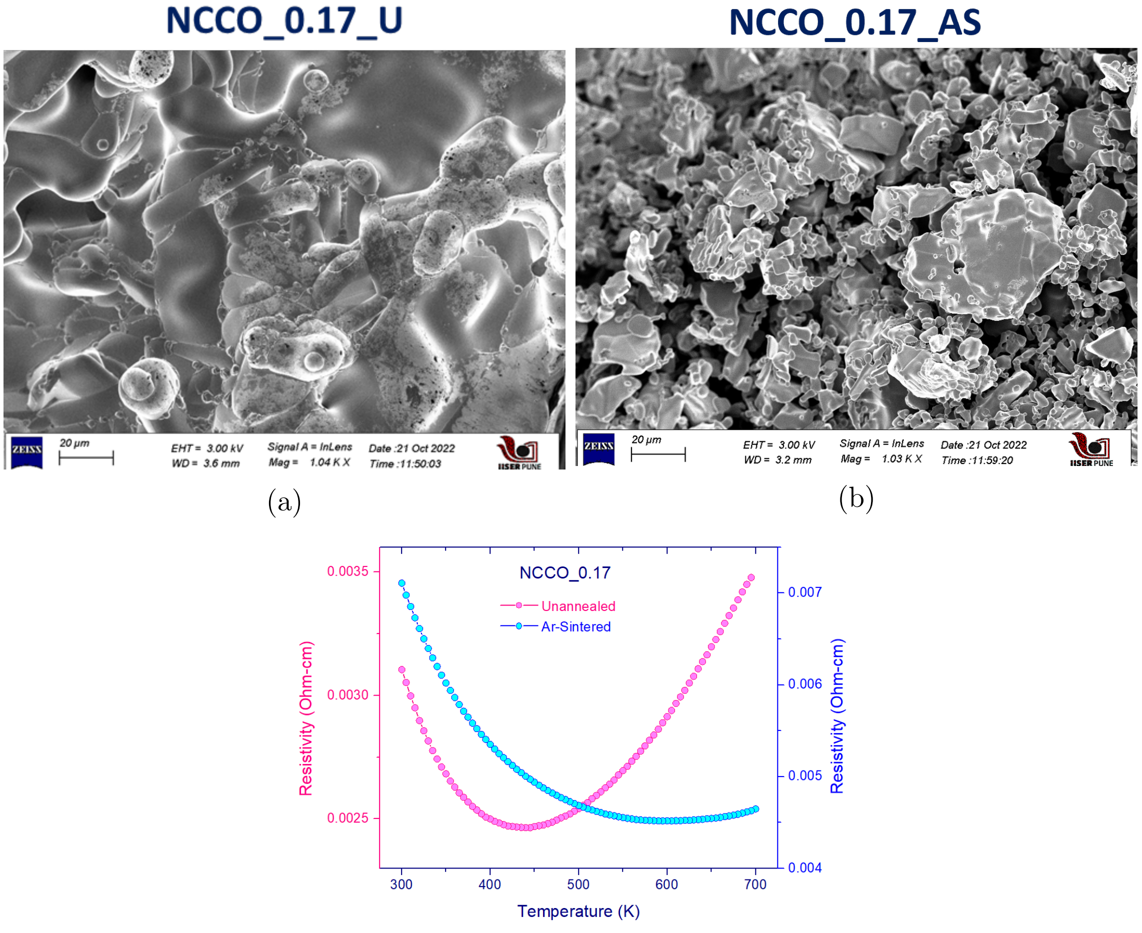

(a)

(b)

(c)

Figure 4.21: (a), (b) The Electron microscopy images of the sample with doping x = 0.17 for two different conditions - Unannealed, Ar-Sintered. (c) Resistivity behavior of the unannealed and Ar-Sintered sample with doping x = 0.17.

Figure 4.21a and 4.21b presents the Electron microscopy images of the unannealed and Ar-Sintered sample with doping x = 0.17. We can clearly see that in the unannealed sample, we have a larger grain size and less grain boundary density. Whereas in the Ar-Sintered sample, we have very small grains and a large number of grain boundaries. The resistivity behavior of these two samples is presented in the figure 4.21c. In the unannealed sample, there is a resistivity upturn of around 450 K, which shifts to a higher temperature after doing this conditioning.

The electron microscopy images and resistivity measurements complement each other. The increased number of grain boundaries in the Ar-Sintered sample results in higher resistivity values and a higher onset temperature for the resistivity upturn. Systems with a denser distribution of grain boundaries necessitate higher temperatures to overcome their impact, allowing the intrinsic characteristics of the sample to emerge only at elevated temperatures.

4.5 Seebeck Coefficient

In this section, we will discuss the results of Seebeck measurements on our polycrystalline samples and how it has varied with sample conditioning. Grain boundaries can influence the Seebeck coefficient (S) in polycrystalline materials through mechanisms like scattering, energy filtering, and carrier trapping. Scattering at grain boundaries can reduce carrier mobility, indirectly affecting S, while energy filtering, which allows high-energy carriers to pass but blocks the low-energy ones, can enhance S by increasing the average energy of the carriers, contributing to electrical conduction. The overall impact of grain boundaries on the Seebeck coefficient is determined by a complex interplay of these effects, which can vary with factors like grain size, doping levels, and temperature.

The Seebeck measurements on the sample $NCCO\_0.17$ are presented in the figure 4.22a. The Seebeck varies smoothly with temperature, increasing in magnitude upon warming. The magnitude of S is low, and it increases by a factor of 2-3 or 4-5, depending on the preparation condition. In particular, no change in the behavior of S is observed near the temperature where we observed resistivity upturn with increasing temperature.

Figure 4.23 presents the Seebeck measurements on a few other samples for our study - Ar-Sintered with x = 0.07, 0.17, and Ar-Annealed with x = 0.10. The Seebeck data follows a gradual change with doping. As the doping concentration decreases, the Seebeck coefficient increases in magnitude. Its temperature dependence also changes from $dS/dT < 0$ for x = 0.17 to $dS/dT > 0$ for x = 0.10 and 0.07. The increase in the magnitude of S is in line with the fact that the Seebeck is inversely related to the carrier concentration. We are further

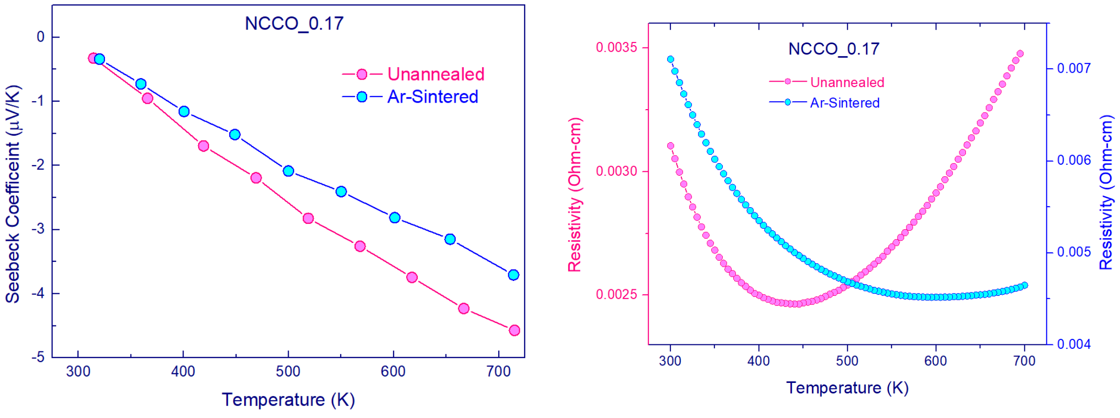

(a) (b)

Figure 4.22: (a) Seebeck data of the sample with doping x =0.17 in the Unannealed and Ar-Sintered version. (b) This graph presents the resistivity data for these two samples.

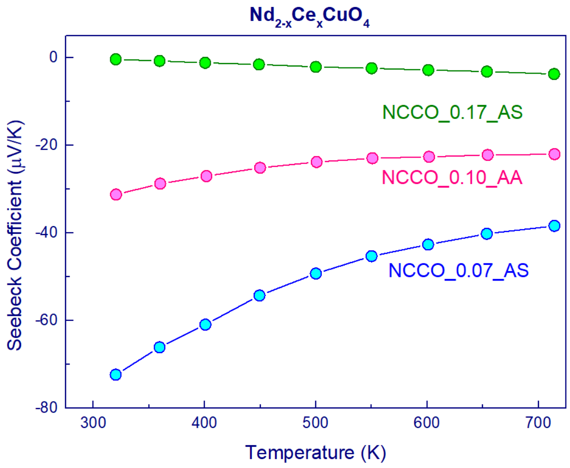

Figure 4.23: The seebeck data of Ar-Sintered samples with x=0.07, 0.17 and Ar-Annealed sample with x = 0.10 up to 700K have been presented in this figure.

exploring the Seebeck measurements on these samples to understand these features.

We can conclude that in the Seebeck data, we don't observe any feature close to the resistivity upturn, suggesting that this feature is not related to the sample's internal electronic structure. So, our analysis of the grain boundary effect contributing to the resistivity behavior stands intact. The Seebeck has decreased after the conditioning, suggesting that the higher grain led to lower carrier mobility.

In this chapter, we have discussed the electrical transport properties of the polycrystalline samples of EDC superconductors above room temperature. The Ar-Annealed EDC shows a complete superconducting transition, in agreement with the literature. This helped us to establish that our samples are superconducting.

The high-temperature resistivity of our samples shows an upturn above a crossover temperature, T^* (i.e., the resistivity increases with increasing temperature above T^*, which depends on the concentration x of Ce - the higher the x, the lower this temperature, T^*). We show that the initial decreasing resistivity trend at low temperatures can be satisfactorily modeled using the Arrhenius activation behavior, which essentially models the grain-boundary scattering. Upon subtracting the grain-boundary contribution, the intrinsic resistivity is found to follow the requisite T^2 dependence over a broad temperature range. It should be emphasized that the presence of grain-boundary scattering masks the T^2 behavior. In other words, the as-measured resistivity does not obey the T^2 dependence, which is revealed only after the GB contribution has been subtracted from the raw data.

In summary, our findings suggest that the quadratic temperature dependence of resistivity at high temperatures is an inherent characteristic of the EDCs. However, in the polycrystalline samples, the intrinsic behavior is obscured by the grain boundary contribution. This inherent quadratic behavior is present in all the samples whose compositions lie in and around the superconducting dome.

Chapter 5

COMBINED MODEL FOR STRANGE METAL

In this chapter, we introduce a unified model aimed at analyzing the resistivity characteristics observed in the Strange Metal state, applicable to both Hole Doped Cuprates (HDC) and Electron Doped Cuprates (EDC). This model incorporates the observed linear resistivity trend in HDC or the linear and quadratic resistivity trends seen in EDC across various temperature domains. The manifestation of these specific resistivity trends at differing temperature ranges will be presented as special cases of our model.

5.1 Description

This model is inspired by the findings from optimally doped samples and extends these insights to account for strange metal behavior for other doping levels and temperature ranges. Initially, we introduce one important approximation and proceed to describe our model, explaining the observed experimental behaviors as special cases within this framework. Subsequent analysis of reported data serves to validate this initial approximation. It is important to acknowledge that our model remains a work in progress; efforts are ongoing to strengthen it with additional evidence and examples. The outline of our model is presented as follows:

The reconstruction of the Fermi surface in EDCs from an electron pocket to a hole-like FS near optimal doping necessitates considering both carrier types to interpret the experimental findings at this doping level [44]. The presence of electron pockets in the

Fermi surface of HDCs [45] motivates the adoption of a single comprehensive equation to describe the resistivity for both HDCs and EDCs, considering the contribution of both types of carriers. Thus, we consider one unified equation to describe the resistivity of both the HDC and EDC, which can be expressed as:

$$\rho(T) = AT + BT^2 + C(T) \tag{5.1}$$

The linear term AT arises from hole scattering, inspired by the linear resistivity trend observed across all temperatures in optimally doped HDC. On the other hand, the quadratic term BT^2 is associated with electron scattering in the sample, drawing motivation from the quadratic temperature dependence reported exclusively in EDC at high temperatures. The term $C(T)$ encompasses the temperature-dependent contributions from defects, disorder, morphology, and microstructures within the samples.

5.2 Physcal Picture

The physical scenario can be simplified as follows. There exists an unknown scattering mechanism within cuprates responsible for the linear temperature term (AT) for holes and the quadratic term (BT^2) for electrons. The lack of a universally accepted microscopic theory explaining the origin of the linear and quadratic terms prevents a detailed discussion of this unidentified scattering mechanism within the scope of this project. Thus, we introduce a single, unknown scattering mechanism operational across all temperature ranges for our analysis. We propose that the coefficient A, associated with hole scattering, is significantly greater than the coefficient B, associated with electron scattering. Consequently, it is assumed that the scattering cross-section area for holes is considerably larger than that for electrons. This hypothesis will be supported by experimental evidence in the subsequent sections.

To summarize, we are starting with two simple assumptions:

1. This scattering mechanism is present over all temperature ranges.
2. A $\gg$ B

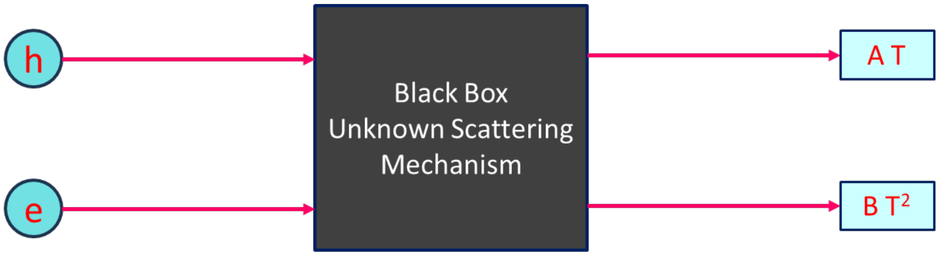

Figure 5.1: Description of the scattering mechanism for the combined model of strange metal

The coefficients A and B will be respectively related to the scattering cross-section area of holes and electrons and their number density.

5.3 Behavior of Single Crystal

Initially, we concentrate our analysis on clean single crystals with a minor amount of disorder or defect concentrations. In this case, C can be assumed to be temperature-independent and relatively very small. For single crystals, C is regarded as a temperature-independent constant. Consequently, the resistivity can be expressed as follows:

$$\begin{aligned} \rho(T) &= AT + BT^2 + C \\ \rho(T) &= B\left[\frac{A}{B}T + T^2 + \frac{C}{B}\right] \end{aligned} \tag{5.2}$$

Next, we follow preliminary algebra to interpret the resistivity trend across different temperature regimes.

$$\begin{aligned} x > x^2 \quad &\text{for} \quad x < 1 \\ x < x^2 \quad &\text{for} \quad x > 1 \end{aligned} \tag{5.3}$$

If we consider x to be T/S, where T is the temperature, and S is a scaling factor, we get:

$$\begin{aligned} &\text{Considering,} \quad x = \frac{T}{S} \\ &ST > T^2 \quad \text{for} \quad T < S \\ &ST < T^2 \quad \text{for} \quad T > S \end{aligned} \tag{5.4}$$

By comparing equations 5.2 and 5.4, we are able to describe the resistivity behavior across two distinct temperature intervals. The equation 5.5 describes those behaviors.

$$\begin{aligned} T < \frac{A}{B} \quad &\implies \quad \frac{A}{B}T > T^2 \quad \implies \quad AT > BT^2 \quad \implies \quad \rho(T) \approx AT + C \\ T > \frac{A}{B} \quad &\implies \quad \frac{A}{B}T < T^2 \quad \implies \quad AT < BT^2 \quad \implies \quad \rho(T) \approx BT^2 + C \end{aligned} \tag{5.5}$$

So, we have two temperature regions depending on the ratio of A and B. The sample will show two different characteristic trends in these two temperature ranges. The onset temperature of Quadratic behavior (T^2) will be related to a function of the ratio of these two parameters, $f(A/B)$. The crossover temperature from linear to quadratic behavior will vary depending on these parameter values of A and B, which are related to the scattering cross-section area of the electrons and holes and their number density.

5.3.1 Hole Doped Cuprates (HDC)

Beginning with the assumption that $A \gg B$, we consider HDC, where the carrier density of holes (n_h) is much higher than that of electrons (n_e). That results in A being considerably greater than B. Consequently, the ratio A/B, associated with the crossover temperature for the onset of quadratic temperature dependence, becomes exceedingly large. This implies that the transition temperature to quadratic behavior falls outside the observed temperature ranges. So, we will always observe the T-linear behavior for the HDC.

5.3.2 Electron Doped Cuprates (EDC)

If we consider the EDC, the scenario is the opposite. We have a carrier density of electrons higher than the carrier density of holes. This condition leads to a comparatively lower A/B ratio, ensuring that the crossover temperature falls within the range we can observe. Experimental findings suggest this, with the transition temperature to quadratic behavior identified around 50K for the disorder-free single crystals and thin films, as reported by Greene et al. [22].

$$\begin{aligned}&\text{For HDC,} \quad n_h \gg n_e \quad \Longrightarrow \quad \frac{A}{B} \text{ is very high} \Longrightarrow \text{Crossover temperature is not in our range.}\\&\text{For EDC,} \quad n_h \ll n_e \quad \Longrightarrow \quad \frac{A}{B} \text{ is not very high} \Longrightarrow \text{Crossover temperature in our range.}\end{aligned} \tag{5.6}$$

5.4 Analysis of Published Data

In this section, we analyzed the published data within our framework and found that they are consistent with our model.

5.4.1 Estimating A/B Ratio

Using this framework, examining the resistivity pattern for EDC — which exhibits a linear temperature dependence at lower temperatures and a quadratic dependence at higher temperatures—indicates an expected A/B ratio on the order of 100, given its crossover temperature is approximately 50 K. We took the reported data of the LCCO sample with a cerium content of 0.15 from the publications of Greene et al. [9] [22]. Their data was evaluated within our model. The findings, depicted in Figure 5.2, reveal a parameter ratio of $A/B = 81K$, aligning with the anticipated order based on the crossover temperature of 50 K. This alignment enhances the credibility of our model as a tool for interpreting the resistivity characteristics of the strange metal state.

5.4.2 Strenth of T-linear term

Our analysis, as presented in the equation 5.6, reveals different magnitudes in the slope of the T-linear resistivity between hole-doped cuprates (HDC) and electron-doped cuprates (EDC). The analysis posits that this discrepancy arises from the distinct scattering cross-section areas of holes and electrons coupled with their respective carrier densities within the samples. This premise suggests that conducting measurements across various HDC and EDC samples in the low-temperature domain could verify these findings. The 2019 Nature publication on the T-linear behavior [17] meticulously examines T-linear resistivity across

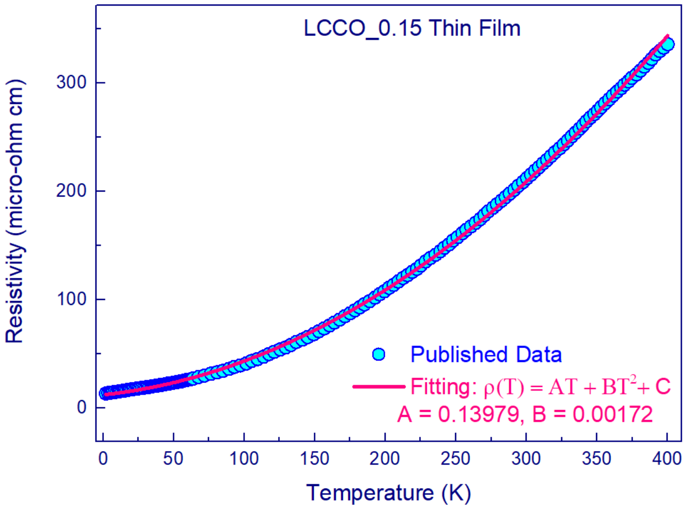

Figure 5.2: Analysis of the reported resistivity data on $LCCO\_0.15$ within our framework.

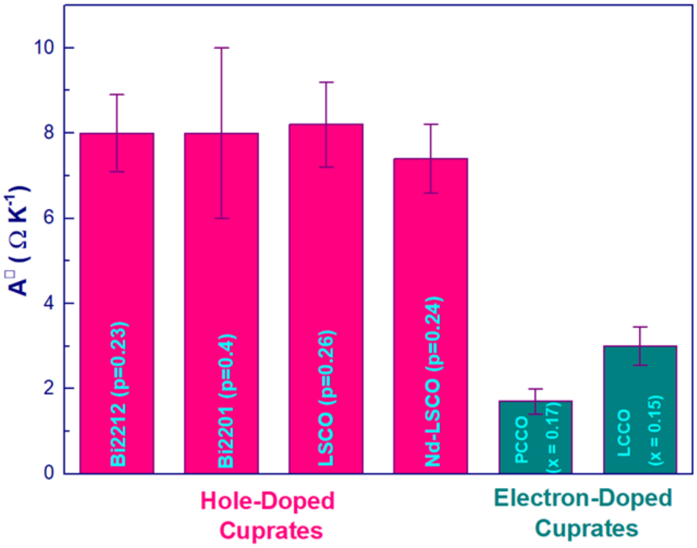

Figure 5.3: The linear coefficient(per CuO_2 plane) for HDC and EDC.

different families of cuprates. This research demonstrates that T-linear resistivity follows the Planckian limit, constituting a universal behavior across all cuprate families. The reported slopes of T-linear resistivity, as depicted in figure 5.3, unambiguously indicate a higher value for HDC as opposed to EDC, which is in line with our hypothesis. In this figure, $A^{\Box}$ corresponds to the slope of the T-linear behavior per CuO_2 plane. ($A^{\Box}$ = A/d, where A is the slope of the T-linear behavior and d is the average separation between CuO_2 planes.)

5.4.3 Carrier Effective Mass for HDC and EDC

Figure 5.4 showcases the effective mass of charge carriers across various HDC and EDC series, revealing a significant disparity: HDCs exhibit a considerably higher effective mass than EDCs. When the effective mass of charge carriers increases, their mobility decreases, leading to lower conductivity. Consequently, a larger effective mass is associated with higher resistivity. This relationship suggests that the contribution of holes, represented by coefficient A, is greater than the contribution of electrons, represented by the coefficient B. Therefore, the approximation $A \gg B$ is supported by this observation. These approximations are further validated in the subsequent section, which reviews studies on co-doped samples.

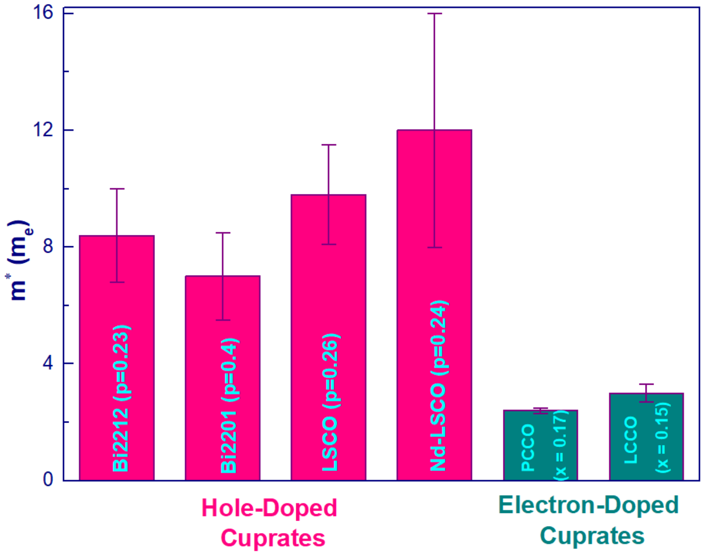

Figure 5.4: Effective mass of the charge carriers in different series of HDC and EDC.

5.5 Behaviour of Polycrystalline sample

Thus far, our analysis has centered on single crystal samples, demonstrating how, within this framework, we can comprehend the linear resistivity trend across the entire temperature spectrum for HDC and the transition from linear to quadratic temperature dependence in EDC. Now, our attention turns to understanding HDC and EDC polycrystalline samples. While the behavior of single-crystal and polycrystalline EDC samples diverges, as discussed extensively in Chapter 4, both single-crystal and polycrystalline HDC samples exhibit similar T-linear resistivity trends. Our aim is to elucidate these behaviors within the same analytical framework. Thus, the experimental results of polycrystalline samples or single crystals and thin films with high disorder should be consistent with the analysis of this section.

We will start by revisiting the results of EDC polycrystalline samples at high temperatures using this model, considering the discussion of Chapter 4. In the case of EDC polycrystalline samples, our analysis revealed that the Arrhenius contribution came from the grain boundaries. Therefore, the final term in Equation 5.1 exhibits Arrhenius-type behavior. The comprehensive equation describing the resistivity of EDC polycrystalline samples at high temperatures is given by:

$$\begin{gathered} \rho(T) = AT + BT^2 + C(T) \quad \Longrightarrow \quad \rho(T) = BT^2 + c\exp^{\frac{\Delta}{k_B T}} \\ \text{(High-Temperature behavior of Polycrystalline sample of EDC)} \end{gathered} \tag{5.7}$$

In our sample, we observed a transition from Arrhenius-type behavior to quadratic temperature dependence, indicating that the magnitude of the quadratic term is comparable to that of the Arrhenius term. This implies that these two terms compete with each other as functions of temperature.

In the case of HDC, it's inferred that the linear term overwhelmingly dominates the quadratic term across our observed temperature range [$AT \gg BT^2$]. Through analysis of the EDC polycrystalline sample, we understood that the quadratic term is comparable in magnitude to the Arrhenius term [$BT^2 \sim C(T)$]. Consequently, the linear term significantly outweighs the Arrhenius term [$AT \gg BT^2 \sim C(T)$] in the polycrystalline samples. This explains why we observe identical T-linear resistivity trends for both single-crystal and polycrystalline HDC samples. We want to mention that, at very low temperatures, charge carriers can tunnel through grain boundaries, a phenomenon not accounted for by the Arrhenius equation. As a result, the Arrhenius relationship may not accurately describe the resistivity behavior in the low-temperature regime.

$$\text{Single Crystal of HDC:} \quad AT \gg BT^2 \quad \Longrightarrow \quad \rho(T) = AT + C$$

$$\text{Single Crystal of EDC:} \begin{cases} \rho(T) = AT + C & \text{For } \ T < \frac{A}{B} \\ \rho(T) = BT^2 + C & \text{For } \ T > \frac{A}{B} \end{cases}$$

$$\text{Polycrystalline sample of EDC at high temperature:} \quad \rho(T) = BT^2 + c\exp^{\frac{\Delta}{k_B T}}$$

$$\text{Polycrystalline sample of HDC at high temperature:} \quad \rho(T) = AT + C$$

$$\text{as,} \quad [AT \gg BT^2 \sim C(T)]$$

We initiated our analysis with basic approximations and proceeded to develop a formalism that aligns with the reported experimental results. A key assumption underlying our approach was the dominance of A over B. This assumption finds support in reported data regarding the carrier's effective mass. Additionally, the studies on co-doped samples of Nd_2CuO_4, as detailed in the subsequent section, further strengthen this assumption.

5.6 Study of co-doped Samples

In Nd_2CuO_4, we dope Ce in the place of Nd for electron-doping and Sr in the place of Nd for hole-doping. The superconducting dome for the electron dope sample is tiny, and x = 0.18 doping of cerium is at the edge of the superconducting dome. Singh et al., in their publication [46], suggested that by doping Sr in these 0.18 Ce-doped, they can get back superconductivity.

The sample $Nd_{1.82-x}Sr_xCe_{0.18}CuO_4$ corresponds to these co-doped samples, which have electrons and holes in the system due to Ce and Sr doping. Even though their results primarily focus on the revival of superconductivity by Sr doping, their data provides valuable insight for our model. Figure 5.5a and 5.5b present their experimental results.

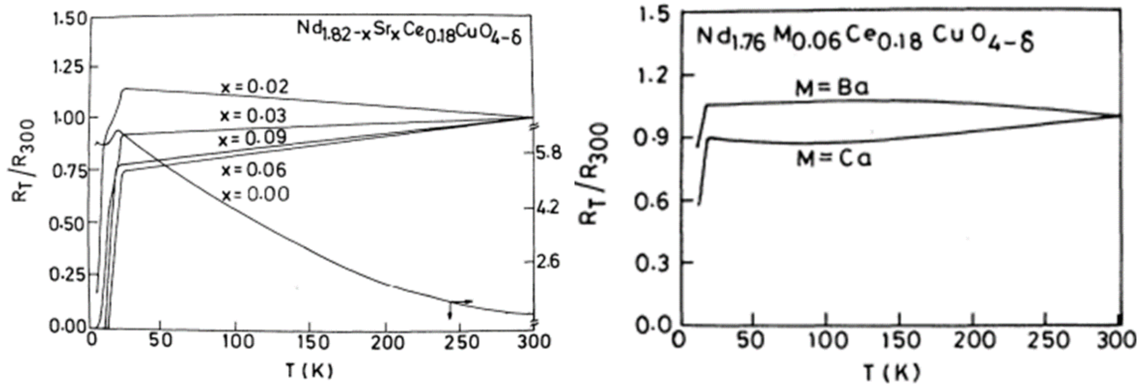

(a)

(b)

Figure 5.5: Results from the publication of Singh et al. on the co-doped sample.

In the sample with only electrons, corresponding to the sample with x = 0.00 in figure 5.5a, the resistivity behavior is strictly decreasing, as usual for the EDC polycrystalline sample. As Sr is introduced with x = 0.02, the behavior no longer strictly decreases. With x =0.03 amount of Sr, the sample shows a linear resistivity trend similar to the behavior of HDC. A similar trend is followed for x =0.06 and x = 0.09 doping of Sr.

In the sample with x = 0.03 doping of Sr, the resistivity behavior resembles the behavior of HDC, which is very surprising. In HDCs, the resistivity varies as T-linear, and in EDCs, the resistivity varies as T^2. When both electrons and holes are present in the co-doped samples due to the doping with Sr and Ce, the overall resistivity will have contributions from both charge carriers, weighted by their respective number densities. In this sample, we have three holes corresponding to the eighteen electrons. Still, the resistivity behavior resembles the characteristic features of the HDC. If electrons and holes were behaving similarly in these samples, we would expect that the EDC sample $NCCO\_0.15$ and the co-doped sample $Nd_{1.79}Sr_{0.03}Ce_{0.18}CuO_4$ have similar behavior. However, the experimental observation is completely different, and this co-doped sample resembles HDC. This hints at how the behavior of holes dominates the behavior of electrons in these samples. Not only that, but the decreasing nature of the polycrystalline EDC is also suppressed. Both of these observation supports our assumption, $A \gg B$, which is that the scattering mechanism of holes dominates the scattering mechanism of electrons.

In the co-doped sample with a doping level of $x = 0.03$ Sr, the resistivity pattern mirrors that of HDC, which is very surprising. Despite having three holes per eighteen electrons in this sample, the resistivity behavior exhibits characteristic features of HDC. If electrons and holes were behaving similarly in these samples, one would anticipate similar behavior between the EDC sample $NCCO\_0.15$ and the co-doped sample $Nd_{1.79}Sr_{0.03}Ce_{0.18}CuO_4$. However, the experimental findings reveal stark differences, with the co-doped sample resembling HDC. This suggests that the behavior of holes predominates over that of electrons in these samples. Moreover, the diminishing trend observed in the polycrystalline EDC is also suppressed. Both observations validate our assumption $A \gg B$ and our analysis of the previous section, indicating that the scattering mechanism of holes dominates over that of electrons.

Figure 5.5b presents the co-doped sample with x = 0.06, where hole doping has been done by Ba and Ca instead of Sr. In these samples, the scattering process will not be exactly the same as that of the Sr-doped sample due to the size mismatch of Ba and Ca with the Nd. This will result in different values of A and B. The results on those samples support this idea, as their resistivity trend is not properly linear.

To summarise, the combined model started with approximations and seems to consistently describe the electrical resistivity of co-doped samples. The crucial experimental results can be understood within our model. The published results about the effective carrier mass in some HDCs and EDCs, as well as the studies on some of the co-doped samples, lend support to our hypothesis. This may suggest that the differences in the electrical resistivity behavior of HDCs and EDCs are due to the different scattering mechanisms associated with electrons and holes.

In conclusion, we argue that the electrons and holes in the high-Tc cuprates have different scattering mechanisms. In samples with electrons as majority carriers, the T^2 behavior dominates at high temperatures, but the T-linear behavior is recovered at low temperatures. We explained this based on the assumption that coefficient A of the T-linear term is very large compared to coefficient B of the T^2 term, which naturally leads to a crossover temperature above which the T^2 term dominates and below which the T-linear term dominates. The inequality $A \gg B$ can be justified from the observation that the holes are relatively much heavier compared to the electrons. In HDCs, where the hole concentration is much larger compared to the electron, the crossover temperature is expected to be very high, which may not even be realizable in the experiments. Previous studies on the co-doped samples support our hypothesis.

Why the holes and electrons have very different scattering cross-sections is an outstanding question, indicating that the Fermi surfaces of these carrier types play an important role, which requires further exploration.

Chapter 6

PLANCKIAN CONJECTURE FOR THERMAL RESISTIVITY

In this chapter, we present our investigation of the thermal diffusivity in polycrystalline samples of NCCO. We aim to draw parallels between these findings and those from electrical transport studies, underscoring the intricate relationship between thermal and electrical behaviors in these materials. For our discussion, the critical term is the inverse of thermal diffusivity, which serves as a measure of the thermal resistivity of the system. So, throughout our discussion, we treat thermal resistivity as synonymous with the inverse of thermal diffusivity. We use these terms interchangeably to articulate our observations and their significance in understanding the complex transport phenomena in NCCO.

6.0.1 Thermal Resistivity

Thermal diffusivity was measured in all the samples using the Linseis LFA setup. Figure 6.1a presents thermal diffusivity data of the underdoped sample $NCCO\_0.07\_U$ showing good reproducibility while heating and cooling the sample. The inverse thermal diffusivity, which is a measure of the thermal resistivity, shows a linear trend at high temperature (T > 500 K) as presented in figure 6.1b. We analyzed this linear thermal resistivity within the Planckian dissipation framework.

The thermal diffusivity in polycrystalline samples is significantly influenced by their

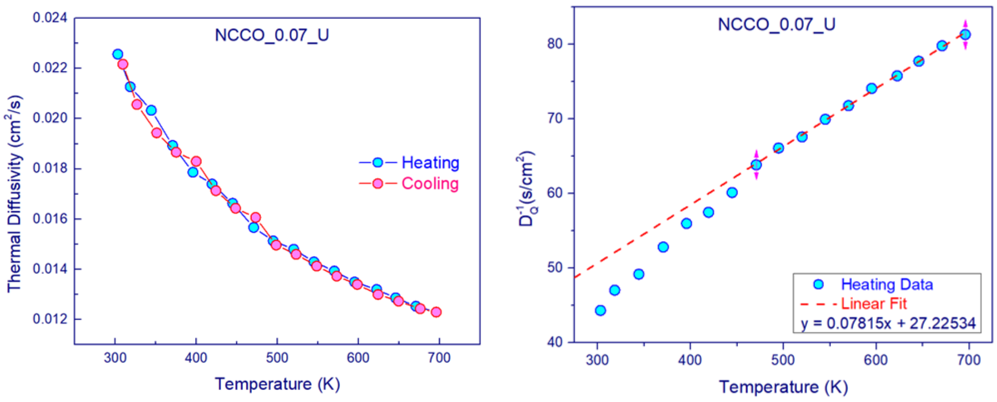

(a) (b)

Figure 6.1: (a) Thermal Diffusivity data of the $NCCO\_0.07\_U$ having good data quality. (b) Thermal resistivity showing a T-linear trend for this sample above 450K.

microstructures, which are pivotal in determining the overall thermal transport properties. These microstructural contributions are integrated into the thermal diffusivity measurements, complicating the separation of these effects from the intrinsic behavior of the material. Despite these challenges, the observation of a T-linear trend in thermal resistivity at high temperatures indicates the ability to probe the material's inherent characteristics.

The onset temperature for this linear behavior, identified at approximately 450 K in Figure 6.1b, is observed to be higher than the previously reported values, which is around 200 K as shown in Figure 1.7a. This discrepancy suggests that the microstructural attributes of polycrystalline samples may lead to a shift in the onset temperature of the T-linear trend in thermal resistivity.

We have observed this T-linear thermal resistivity behavior in all of our samples, spanning from the underdoped to the overdoped region of the phase diagram with slightly different onset temperatures. The thermal diffusivity data for all the samples have been presented in the Appendix.

6.0.2 Association with the Electrical Resistivity upturn

Figures 6.2a and 6.2b display the thermal resistivity data for unannelaed samples doped at $x = 0.15$ and $x = 0.20$, respectively. Surprisingly, the onset of the T-linear behavior (T^{**}) in thermal resistivity coincides with the temperature (T^{*}) where a resistivity upturn

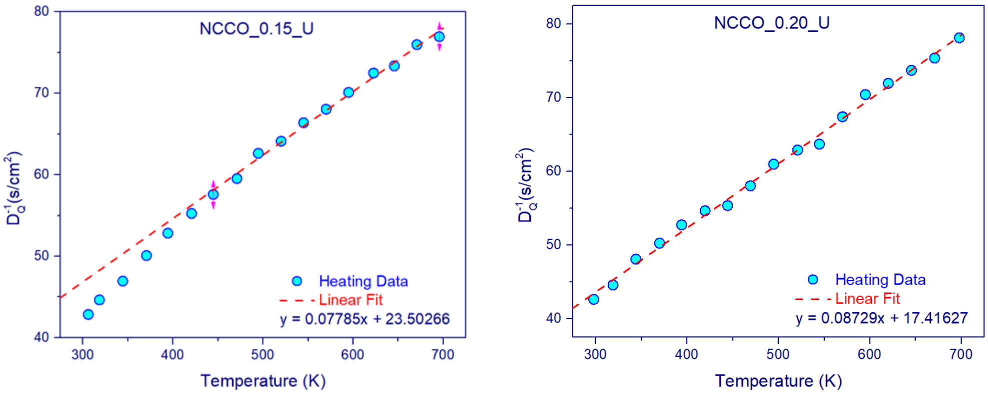

(a)

(b)

Figure 6.2: Thermal resistivity showing T-linear behavior for the sample $NCCO\_0.15\_U$ (a) and $NCCO\_0.20\_U$ (b).

is observed in all the unannealed samples, as evident from the data of the $NCCO\_0.15\_U$ sample in figure 6.2a. This correlation between the two behaviors is intriguing, suggesting a potential link between them. The resistivity upturn, corresponding to the T^2 behavior, has not been previously accounted for within the Planckian dissipation limit framework. For the $NCCO\_0.20\_U$ sample, the onset of T^2 behavior in resistivity data occurs below room temperature, which aligns with the observation that the T-linear trend in thermal resistivity for this sample also begins below room temperature, given that thermal resistivity maintains a linear trend above room temperature. This parallel suggests a possible correlation between the T-linear thermal resistivity and T^2 electrical resistivity behaviors despite the lack of a detailed microscopic understanding of these observations.

Figure 6.3a showcases thermal resistivity data for two variants of $NCCO\_0.010$ sample. The Ar-Annealed sample has a lower thermal resistivity, diverging from the trend observed in electrical resistivity. In electrical transport data, the Ar-Annealed sample has a higher resistivity than the unannealed sample for $NCCO\_0.10$ as shown in figure 4.8.

Conversely, the Ar-Sintered $NCCO\_0.07$ sample presents an elevated thermal resistivity compared to its unannealed counterpart, aligning with electrical resistivity outcomes as shown in the figure 4.9a. In the Ar-Sintered sample, the T^2 resistivity behavior is entirely suppressed, whereas the T-linear trend in thermal resistivity persists, as evidenced in Figure 6.3b. This observation indicates that the relationship between electrical and thermal

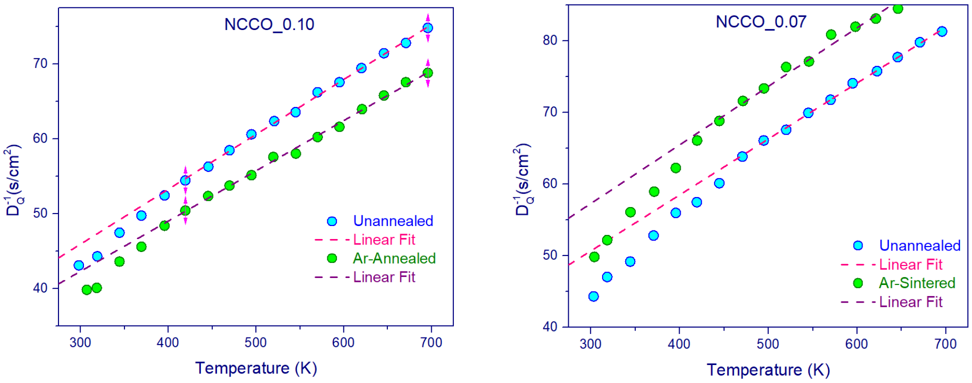

(a) (b)

Figure 6.3: Thermal resistivity for two different versions of the $NCCO\_0.10$ sample - Unannealed, Ar-Annealed (a) and $NCCO\_0.07$ sample - Unannealed, Ar-Sintered.

resistivity is complex and not very straightforward. In this section of the thesis, we are showcasing the findings of thermal resistivity alongside the studies on electrical resistivity. Yet, the precise interrelation between these two transport phenomena remains unidentified. Elucidating the dynamics between phonon and electron transport stands as our forthcoming challenge.

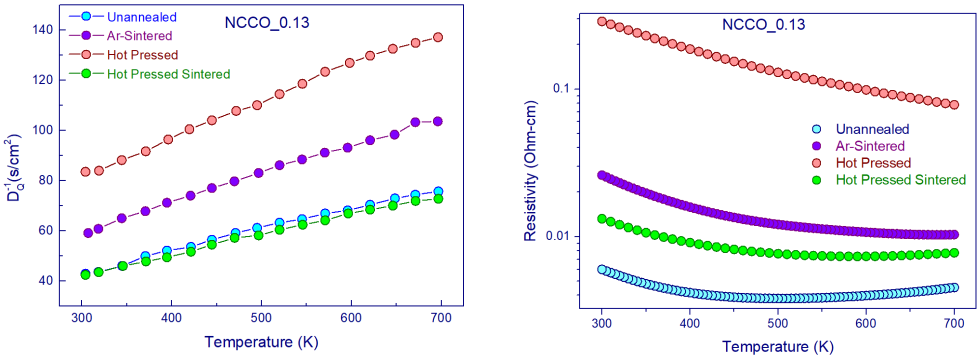

(a) (b)

Figure 6.4: (a) Thermal resistivity for different versions of the $NCCO\_0.13$. (b) Electrical resistivity corresponding to the same sample conditioning.

The electrical and thermal resistivity measurements of $NCCO\_0.13$ exhibit a direct correspondence in their relative values, highlighting the pivotal role of microstructures in influencing both electrical and thermal transport properties. This parallel suggests that a thorough understanding of microstructural influences is also essential for elucidating the underlying connections between thermal and electrical transport mechanisms.

Comparing T* with T**

The onset temperature of the resistivity upturn denoted as T^*, and the onset of T-linear behavior in thermal resistivity, denoted as T^{**}, are presented in parallel. Figure 6.5b illustrates the decrease in T^{**} with increased cerium doping, indicating a consistent downward trend with doping levels. The similar decreasing trend of T^* and T^{**} with doping suggests a potential linkage between these phenomena.

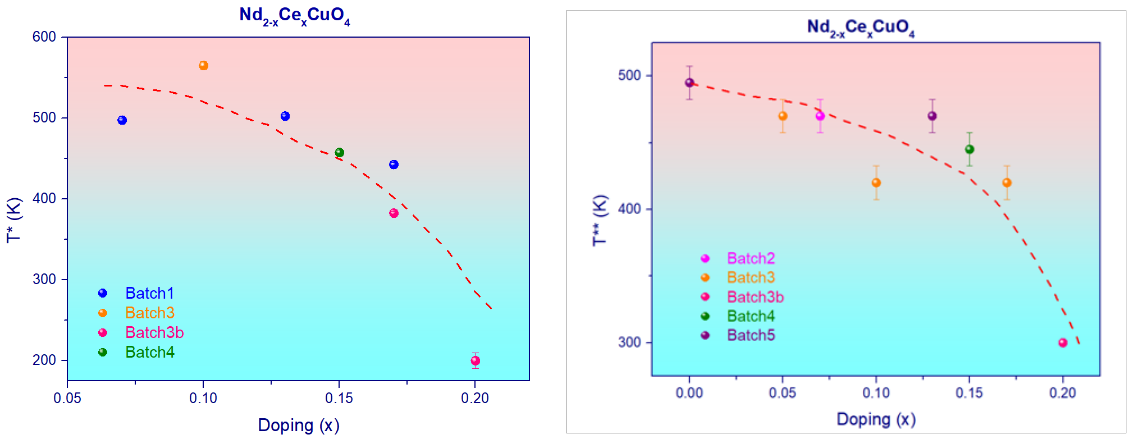

(a) (b)

Figure 6.5: (a)The onset temperature of resistivity upturn, T* for different Ce doping. (b) The onset temperature of the T-linear behavior in thermal resistivity, T** as a function of Ce doping

6.0.3 Effective Thermal Diffusion Velocity and Diffusion Mass

The thermal resistivity of all samples has been analyzed within the framework of the Planckian Conjecture. Utilizing linear fit data of the thermal resistivity (D_Q^{-1}), we calculate the thermal diffusion velocity (v_B) and effective diffusion mass (m_D) using Equation 6.1. In this equation, 'a' represents the slope of the linear fit, 'b' corresponds to the intercept of the linear fit, and 's' is an order-unity constant. For our calculations, we set 's' to 2, as discussed in Refs. [30] and [31].

$$\begin{aligned} v_{ph} &= \sqrt{\frac{K_B}{as\hbar}} \\ m_D &= \frac{b\hbar}{3} \end{aligned} \tag{6.1}$$

By computing v_B and m_D as functions of Ce doping, our objective is to explore their systematic evolution across the phase diagram of cuprates. This endeavor aims to elucidate the extent to which the Planckian conjecture is applicable within the cuprates phase diagram.

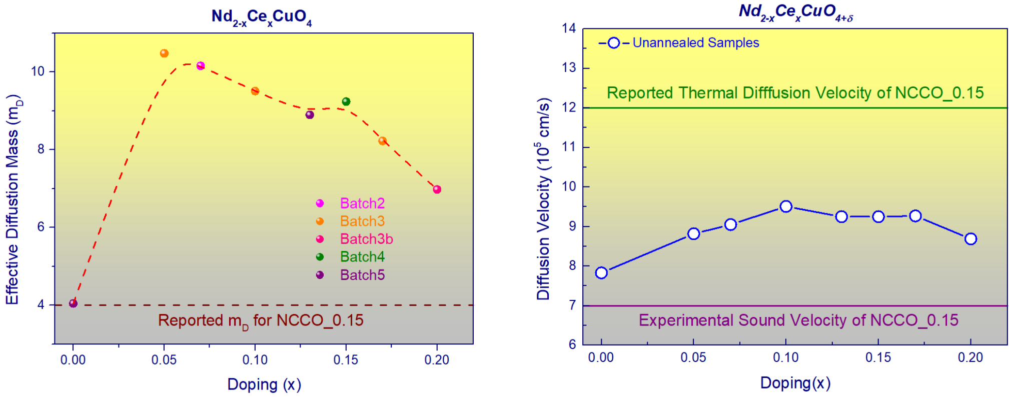

(a) (b)

Figure 6.6: Effective Diffusion Mass (a) and Diffusion velocity (b) of $NCCO$ as calculated from the Planckian Conjecture analysis has been presented for different dopings.

As our analysis has focused on polycrystalline samples of $NCCO$, to achieve a conclusive understanding, it's essential to recognize the impact of microstructures on thermal resistivity. The effective diffusion velocity, depicted in Figure 6.6b, remains constant with respect to doping, within the limits of our measurement accuracy. This velocity is lower than the thermal diffusion velocity reported for single crystals, implying that microstructure and GB hinder heat transport. However, the diffusion velocity exceeds the sound velocity in the single crystal, indicating a substantial role of charge carriers in thermal conduction. The diffusion velocity of the single crystal and sound velocity have been taken from the ref. [30].

The effective diffusion mass is calculated from the intercept of the linear fit, D^0_{-1}. This intercept acts as a constant that separates the coherent and incoherent regimes of the electronic contribution of the thermal transport. This term relates to phonon scattering by charge carriers within these systems. Therefore, the evolution of m_D across different doping levels should reflect variations in the strength of this scattering process. Intuitively, introducing more carriers is expected to enhance the scattering process. Contrary to this expectation, the data presented in Figure 6.6a indicates a decrease in the effective mass, m_D, with increasing doping, followed by a sharp decline in the parent sample. Additionally, the disorder also introduces an additional component to the intercept, as discussed in the ref. [47]. Our calculated diffusion mass is significantly larger than the diffusion mass reported for single crystals, a difference likely due to the microstructures present in the polycrystalline samples. Thus, assessing the impact of the disorder is essential for accurately interpreting these results.

In summary, our thermal transport studies on polycrystalline samples of EDC reveal intriguing connections with the resistivity upturn or the T^2 behavior. We observed a T-linear behavior in the inverse thermal diffusivity, as reported by Kapitulnik et al. [30]. Our research underscores the presence of this linear trend, indicative of incoherent transport, across a wide range of doping in $NCCO$. The influence of microstructures undoubtedly plays a crucial role in the physical properties of these samples. Therefore, a deeper understanding of these contributions and developing models to account for them will be essential in clarifying the exact relationship between thermal and electrical transport properties.

Chapter 7

CONCLUSIONS

In this thesis, we have conducted a detailed study of polycrystalline samples of $Nd_{2-x}Ce_xCuO_4$ (NCCO) to explore the high-temperature electrical and thermal transport properties of electron-doped cuprates (EDCs), leading to important findings. We synthesized NCCO samples with varying cerium doping concentrations, covering a wide range of the phase diagram of EDC. The quality of the samples was examined using XRD, SEM-EDX, and TGA probes. Our TGA data analysis suggests an oxygen content close to the ideal value of 4 for all the samples studied in this thesis.

The low-temperature resistivity measurements confirmed the superconductivity in the Ar-Annealed NCCO samples. Exploring the high-temperature resistivity behavior, we observed new findings. We noticed a resistivity upturn in our unannealed samples above a crossover temperature (T^*). Ar-Sintering enhances this cross-over temperature T^* above which the resistivity shows an upturn. This controlled conditioning of the samples, leading to different cross-over temperatures, presents the important contributions from the microstructures of the samples in dictating the overall behavior of the polycrystalline EDC samples. Our detailed analysis using the Arrhenius model to represent the grain boundary scattering contribution to resistivity led to the understanding of this resistivity upturn. This resistivity upturn corresponds to the T^2 behavior observed in single crystals of EDCs; however, it is masked by contributions from the grain boundaries. After subtracting the GB contribution from the as-measured resistivity, we recovered the T^2 behavior in our samples. Our study highlights that the T^2 behavior is an inherent true characteristic of EDCs. However, we can only observe this behavior once the carriers can overcome the grain boundary effects at high temperatures or over a wider temperature range after subtracting the GB contribution.

Our studies of the Seebeck coefficient and sample conditioning using the hot-pressing technique strongly support this hypothesis. With the help of the hot-pressing technique, we can increase the grain-boundary density, leading to a higher crossover temperature (T^*). Thus, after subtracting the GB scattering contribution from the raw data, we showed that the T^2 behavior is always present in EDCs over a wide range of doping (x = 0.10 to x = 0.20) and temperature. Thus, whether one would see the intrinsic behavior in the raw / as-measured data or not depends highly on the microstructure. In the single crystal samples, where no grain-boundary effect is expected, a T^2 behavior is directly revealed.

With this understanding of grain boundary contribution, we propose a simple joint equation comprising T-linear, T^2, and the Arrhenius term to explain different experimental resistivity results in both EDCs and HDCs. This model is also consistent with the previous studies on the co-doped samples.

The thermal transport studies in our samples are in good agreement with previous reports, and our study suggests the T-linear behavior of the inverse thermal diffusivity is present over a wide range of doping concentrations. Thermal resistivity analysis of our samples using the Planckian Conjecture suggests the presence of a direct correlation between the temperature T^* above which we observed an increase in resistivity and the temperature T^{**} above which the thermal resistivity exhibits a linear dependence on temperature (T-linearity). Currently, we are analyzing our experimental data to understand this interesting correlation further.

Appendix A

Thermal Resistivity

In this appendix, we present the thermal diffusivity (D_Q) and thermal resistivity (D_Q^{-1}) data for all the Unannealed samples. We have used the linear fitting of the thermal resistivity data from all samples to derive the diffusion mass and diffusion velocity.

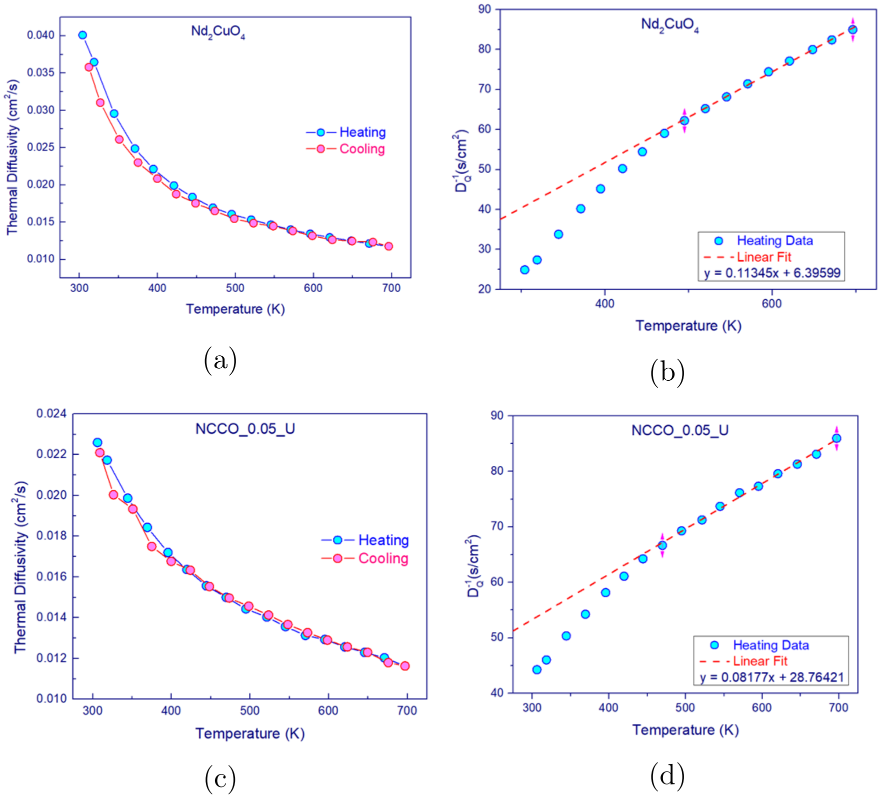

(a) (b)

(c) (d)

Figure A.1: Themarl Diffusivity (in left) and thermal diffusivity inverse (in right) for x = 0 (a,b) and 0.05 (c,d).

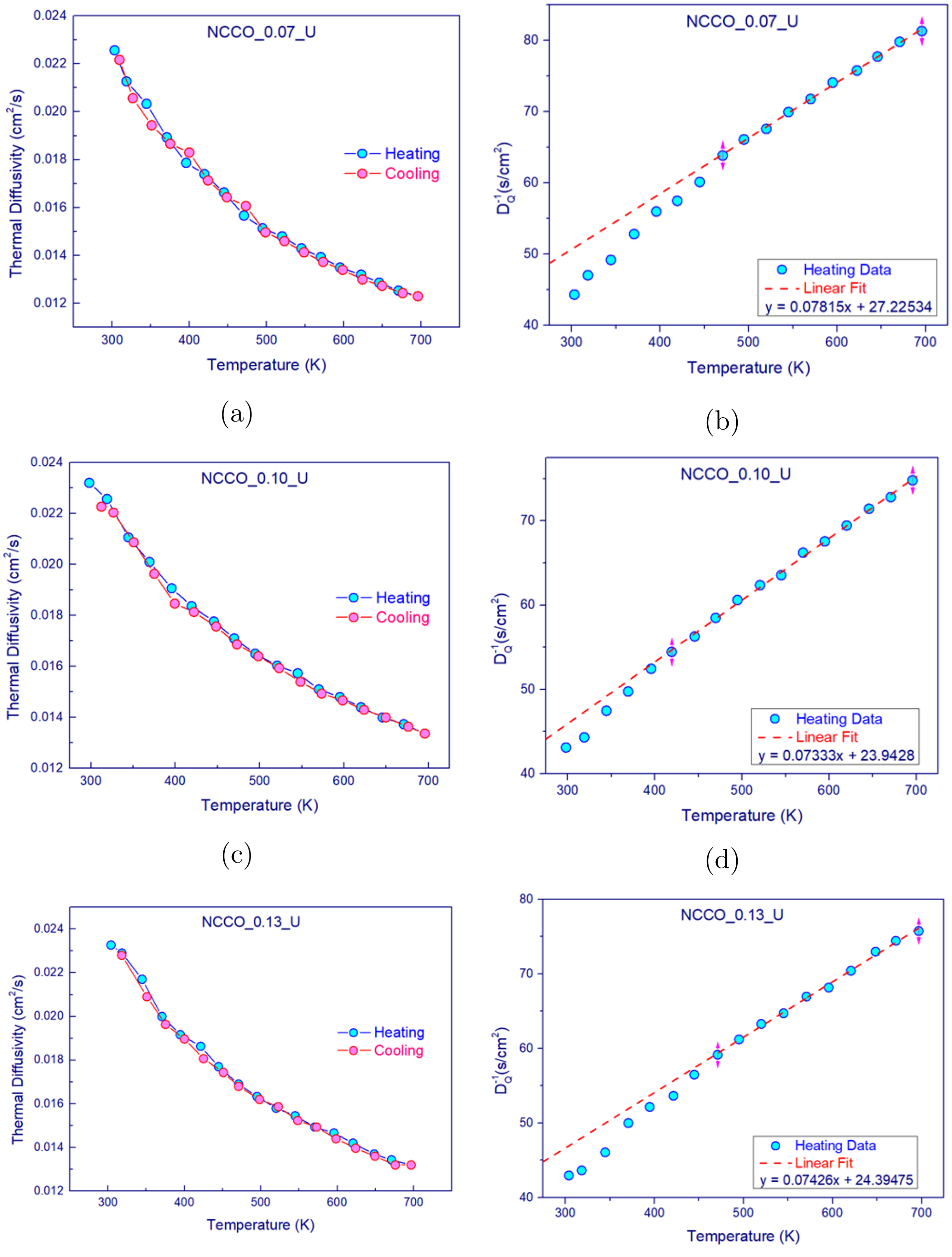

(a) (b)

(c) (d)

(e) (f)

Figure A.2: Themarl Diffusivity (in left) and thermal diffusivity inverse (in right) for x = 0.07 (a,b), 0.10 (c,d) and 0.13 (e,f).

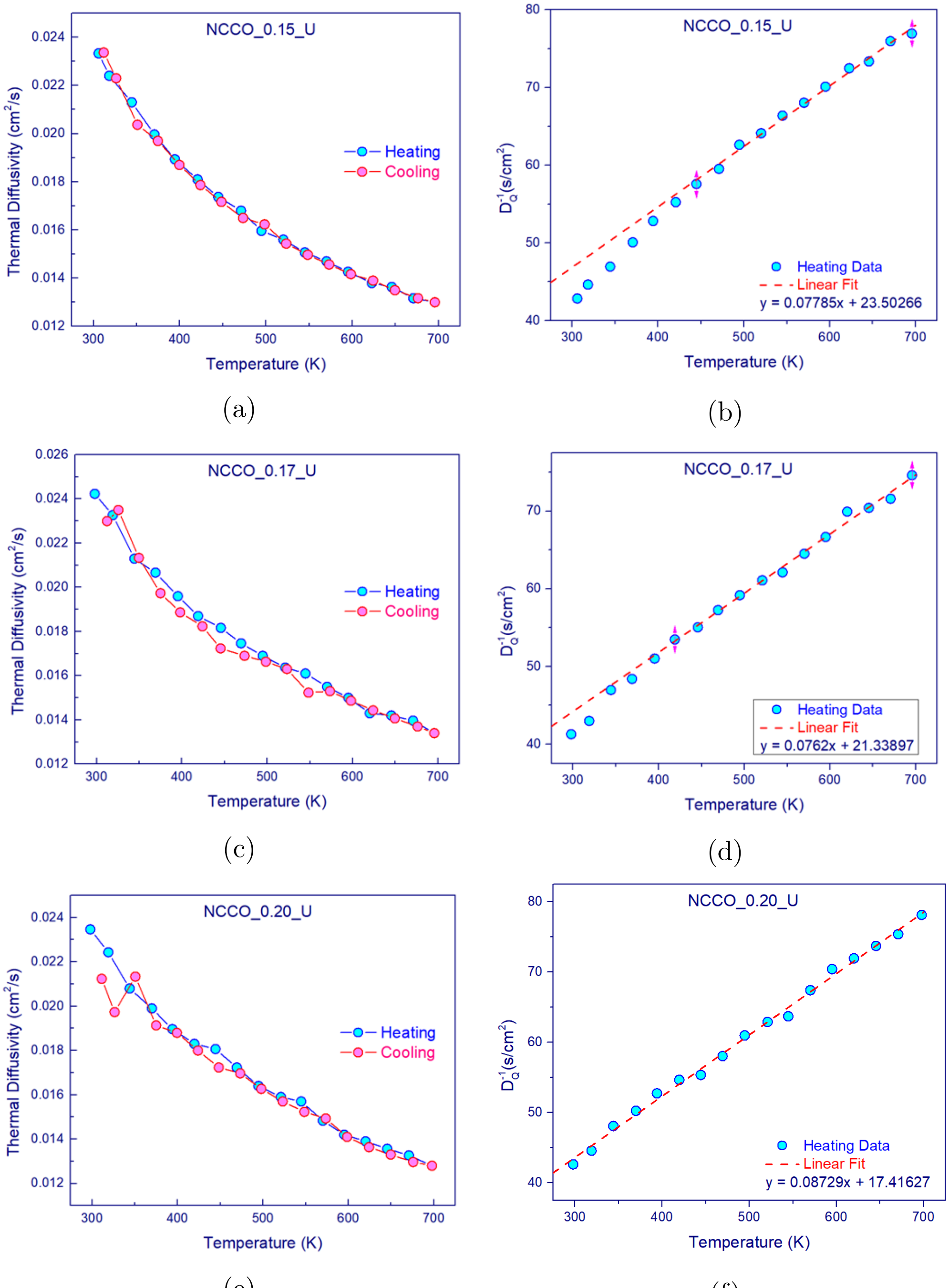

(a) (b) (c) (d) (e) (f)

Figure A.3: Themarl Diffusivity (in left) and thermal diffusivity inverse (in right) for x = 0.15 (a,b), 0.17 (c,d) and 0.20 (e,f).

References

[1] J. G. Bednorz and K. A. Müller, "Possible high t c superconductivity in the ba- la- cu- o system," *Zeitschrift für Physik B Condensed Matter*, vol. 64, no. 2, pp. 189–193, 1986.

[2] Y. Kamihara, T. Watanabe, M. Hirano, and H. Hosono, "Iron-based layered superconductor la [o1-x f x] feas (x= 0.05- 0.12) with t c= 26 k," *Journal of the American Chemical Society*, vol. 130, no. 11, pp. 3296–3297, 2008.

[3] J. Nagamatsu, N. Nakagawa, T. Muranaka, Y. Zenitani, and J. Akimitsu, "Superconductivity at 39 k in magnesium diboride," *nature*, vol. 410, no. 6824, pp. 63–64, 2001.

[4] B. White, J. Thompson, and M. Maple, "Unconventional superconductivity in heavy-fermion compounds," *Physica C: superconductivity and its applications*, vol. 514, pp. 246–278, 2015.

[5] S. Banerjee, C. Dasgupta, S. Mukerjee, T. Ramakrishnan, and K. Sarkar, "High temperature superconductivity in the cuprates: Materials, phenomena and a mechanism," vol. 2005, no. 1, 2018.

[6] C. Chu, L. Deng, and B. Lv, "Hole-doped cuprate high temperature superconductors," *Physica C: Superconductivity and its Applications*, vol. 514, pp. 290–313, 2015.

[7] F. Boschini, M. Zonno, E. Razzoli, R. P. Day, M. Michiardi, B. Zwartsenberg, P. Nigge, M. Schneider, E. H. da Silva Neto, A. Erb, *et al.*, "Emergence of pseudogap from short-range spin-correlations in electron-doped cuprates," *npj Quantum Materials*, vol. 5, no. 1, p. 6, 2020.

[8] C. Proust and L. Taillefer, “The remarkable underlying ground states of cuprate superconductors,” *Annual Review of Condensed Matter Physics*, vol. 10, pp. 409–429, 2019.

[9] R. L. Greene, P. R. Mandal, N. R. Poniatowski, and T. Sarkar, “The strange metal state of the electron-doped cuprates,” *Annual Review of Condensed Matter Physics*, vol. 11, pp. 213–229, 2020.

[10] O. Gunnarsson, M. Calandra, and J. Han, “Colloquium: Saturation of electrical resistivity,” *Reviews of Modern Physics*, vol. 75, no. 4, p. 1085, 2003.

[11] P. Fournier, “T’ and infinite-layer electron-doped cuprates,” *Physica C: Superconductivity and its Applications*, vol. 514, pp. 314–338, 2015.

[12] C. Chu, L. Deng, and B. Lv, “Hole-doped cuprate high temperature superconductors,” *Physica C: Superconductivity and its Applications*, vol. 514, pp. 290–313, 2015.

[13] *Cuprates phase diagram*, https://en.wikipedia.org/wiki/File:Cuprates_phasedigagram_en.svg, Accessed: 2024-04-15.

[14] S. M. O’Mahony, W. Ren, W. Chen, Y. X. Chong, X. Liu, H. Eisaki, S.-i. Uchida, M. Hamidian, and J. S. Davis, “On the electron pairing mechanism of copper-oxide high temperature superconductivity,” *Proceedings of the National Academy of Sciences*, vol. 119, no. 37, e2207449119, 2022.

[15] D. v. d. Marel, H. Molegraaf, J. Zaanen, Z. Nussinov, F. Carbone, A. Damascelli, H. Eisaki, M. Greven, P. Kes, and M. Li, “Quantum critical behaviour in a high-t c superconductor,” *Nature*, vol. 425, no. 6955, pp. 271–274, 2003.

[16] T. Helm, M. Kartsovnik, C. Proust, B. Vignolle, C. Putzke, E. Kampert, I. Sheikin, E.-S. Choi, J. Brooks, N. Bittner, *et al.*, “Correlation between fermi surface transformations and superconductivity in the electron-doped high-t c superconductor nd 2- x ce x cuo 4,” *Physical Review B*, vol. 92, no. 9, p. 094 501, 2015.

[17] A. Legros, S. Benhabib, W. Tabis, F. Laliberté, M. Dion, M. Lizaire, B. Vignolle, D. Vignolles, H. Raffy, Z. Li, *et al.*, “Universal t-linear resistivity and planckian dissipation in overdoped cuprates,” *Nature Physics*, vol. 15, no. 2, pp. 142–147, 2019.

[18] T. Sarkar, P. Mandal, N. Poniatowski, M. K. Chan, and R. L. Greene, “Correlation between scale-invariant normal-state resistivity and superconductivity in an electron-doped cuprate,” *Science Advances*, vol. 5, no. 5, eaav6753, 2019.

[19] P. Mandal, T. Sarkar, and R. L. Greene, “Anomalous quantum criticality in the electron-doped cuprates,” *Proceedings of the National Academy of Sciences*, vol. 116, no. 13, pp. 5991–5994, 2019.

[20] J. Ayres, M. Berben, M. Čulo, Y.-T. Hsu, E. van Heumen, Y. Huang, J. Zaanen, T. Kondo, T. Takeuchi, J. Cooper, *et al.*, “Incoherent transport across the strange-metal regime of overdoped cuprates,” *Nature*, vol. 595, no. 7869, pp. 661–666, 2021.

[21] N. R. Poniatowski, T. Sarkar, and R. L. Greene, “Anomalous normal-state magnetotransport in an electron-doped cuprate,” *Physical Review B*, vol. 103, no. 12, p. 125 102, 2021.

[22] T. Sarkar, R. L. Greene, and S. D. Sarma, “Anomalous normal-state resistivity in superconducting l a 2- x c e x cu o 4: Fermi liquid or strange metal?” *Physical Review B*, vol. 98, no. 22, p. 224 503, 2018.

[23] P. Bach, S. Saha, K. Kirshenbaum, J. Paglione, and R. Greene, “High-temperature resistivity in the iron pnictides and the electron-doped cuprates,” *Physical Review B*, vol. 83, no. 21, p. 212 506, 2011.

[24] J. Kim and E. Kvam, “Study on the possible structural transition in nd2- xcexcuo4-δ,” *Physica C: Superconductivity*, vol. 292, no. 3-4, pp. 203–210, 1997.

[25] H. Takagi, B. Batlogg, H. Kao, J. Kwo, R. Cava, J. Krajewski, and W. Peck Jr, “Systematic evolution of temperature-dependent resistivity in la 2- x sr x cuo 4,” *Physical review letters*, vol. 69, no. 20, p. 2975, 1992.

[26] N. Mori, T. Kameyama, H. Enomoto, H. Ozaki, Y. Takano, and K. Sekizawa, “Thermoelectric power and resistivity in nd2- xcexcuo4 system,” *Journal of alloys and compounds*, vol. 408, pp. 1222–1225, 2006.

[27] R. Jardim, E. Early, and M. Maple, "Properties of polycrystalline nd1. 85ce0. 15cuo4-γ prepared under different conditions," *Journal of alloys and compounds*, vol. 221, no. 1-2, pp. 1–14, 1995.

[28] T. Klimczuk, W. Sadowski, J. Olchowik, and E. Walker, "Crystal growth and the influence of oxygen stoichiometry on electrical resistivity of single crystals," *Superconductor Science and Technology*, vol. 12, no. 4, p. 199, 1999.

[29] M. Naito, H. Sato, and H. Yamamoto, "Mbe growth of (la, sr) 2cuo4 and (nd, ce) 2cuo4 thin films," *Physica C: Superconductivity*, vol. 293, no. 1-4, pp. 36–43, 1997.

[30] J. Zhang, E. D. Kountz, E. M. Levenson-Falk, D. Song, R. L. Greene, and A. Kapitulnik, "Thermal diffusivity above the mott-ioffe-regel limit," *Physical Review B*, vol. 100, no. 24, p. 241 114, 2019.

[31] J. Zhang, E. D. Kountz, K. Behnia, and A. Kapitulnik, "Thermalization and possible signatures of quantum chaos in complex crystalline materials," *Proceedings of the National Academy of Sciences*, vol. 116, no. 40, pp. 19 869–19 874, 2019.

[32] Bruker, *Bruker d8 advance powder x-ray diffractometer*, https://hijaz-jo.com/product/the-d8-advance-family/, Accessed: 2024-03-25.

[33] Nanoscience, *Scanning electron microscope*, https://www.nanoscience.com/techniques/scanning-electron-microscopy/, Accessed: 2024-03-25.

[34] V. COAT, *Electron microscope (em)*, https://vaccoat.com/blog/electron-microscope/, Accessed: 2024-03-25.

[35] Netzsch, *Netzsch sta 449 f1 tga setup*, https://www.azonano.com/equipment-details.aspx?EquipID=301, Accessed: 2024-03-15.

[36] Linseis, *Linseis lsr3*, https://www.linseis.com/en/products/thermoelectric/lsr-3/, Accessed: 2024-03-15.

[37] Linseis, *Linseis lfa 500*, https://www.linseis.com/en/products/thermal-conductivity-instruments/lfa-500/, Accessed: 2024-03-15.

[38] A. Guarino, C. Autieri, P. Marra, A. Leo, G. Grimaldi, A. Avella, and A. Nigro, “Superconductivity induced by structural reorganization in the electron-doped cuprate nd 2- x ce x cuo 4,” *Physical Review B*, vol. 105, no. 1, p. 014 512, 2022.

[39] H. Takagi, S. Uchida, and Y. Tokura, “Superconductivity produced by electron doping in cuo 2-layered compounds,” *Physical review letters*, vol. 62, no. 10, p. 1197, 1989.

[40] M. Lambacher, T. Helm, M. Kartsovnik, and A. Erb, “Advances in single crystal growth and annealing treatment of electron-doped htsc,” *The European Physical Journal Special Topics*, vol. 188, pp. 61–72, 2010.

[41] N. R. Raveendran, K. Vinod, E. Amaladass, J. Janaki, and A. Mani, “Investigation of the effect of ag addition on the critical current density of the high-temperature superconductor nd1. 85ce0. 15cuo4,” *Superconductor Science and Technology*, vol. 29, no. 7, p. 075 012, 2016.

[42] Y. Onose, Y. Taguchi, K. Ishizaka, and Y. Tokura, “Charge dynamics in underdoped nd 2- x ce x cuo 4: Pseudogap and related phenomena,” *Physical Review B*, vol. 69, no. 2, p. 024 504, 2004.

[43] S. Badwal, “Electrical conductivity of single crystal and polycrystalline yttria-stabilized zirconia,” *Journal of materials science*, vol. 19, pp. 1767–1776, 1984.

[44] N. Armitage, F. Ronning, D. Lu, C. Kim, A. Damascelli, K. Shen, D. Feng, H. Eisaki, Z.-X. Shen, P. Mang, *et al.*, “Doping dependence of an n-type cuprate superconductor investigated by angle-resolved photoemission spectroscopy,” *Physical Review Letters*, vol. 88, no. 25, p. 257 001, 2002.

[45] D. LeBoeuf, N. Doiron-Leyraud, J. Levallois, R. Daou, J.-B. Bonnemaison, N. Hussey, L. Balicas, B. Ramshaw, R. Liang, D. Bonn, *et al.*, “Electron pockets in the fermi surface of hole-doped high-t c superconductors,” *Nature*, vol. 450, no. 7169, pp. 533–536, 2007.

[46] O. G. Singh, O. Prakash, B. Padalia, and A. V. Narlikar, “Evidence for the revival of superconductivity in nd 1.82 ce 0.18 cuo 4- δ by doping with divalent alkaline-earth elements,” *Physical Review B*, vol. 48, no. 17, p. 13 182, 1993.

[47] C. Mousatov and S. Hartnoll, “Phonons, electrons and thermal transport in planckian high,” *Tc*, 2021.